UNIVERSITÀ
DEGLI STUDI
DI PADOVA

Università degli Studi di Padova

Dipartimento di Scienze Chirurgiche Oncologiche e Gastroenterologiche

Scuola di dottorato di ricerca in

ONCOLOGIA E ONCOLOGIA CHIRURGICA

XXVI ciclo

Cellular communication and cancer therapy:

targeting Ca^{2+} and NO signalling within the tumour microenvironment

Direttore della Scuola : Ch.ma Prof. Paola Zanovello

Supervisore :Ch.mo Prof. Vincenzo Bronte

Co-Supervisore :Ch.mo Prof. Fabio Mammano

Dottorando : Bianca Calì

Anno accademico 2012-2013

Index

Abstract

Cell death and bystander effect are crucial for both the efficacy of cancer therapy and the modulation of anti-tumour immune response. The 'bystander effect' refers to a process whereby untreated cells exhibit either the deleterious or beneficial indirect effects as a result of signals received from nearby targeted cells. Various molecular players and pathways have been suggested to mediate the bystander effects, nevertheless to date it is not known which are the key molecules and cellular mechanisms underpinning cell death signal propagation. Several reports suggest the involvement of both nitric oxide (NO) and reactive nitrogen species (RNS) in mediating the bystander effect. Nevertheless their role in the process has not been totally defined since these molecules can either inhibit or sustain tumour progression. Additionally, the methods conventionally applied for NO tracking do neither necessarily reflect real-time NO production nor allow studies into intact three-dimensional tumour mass.

The primary aim of this study was to investigate and characterize cell signals responsible for the bystander effect within the tumour microenvironment, paying particular attention to NO. To this purpose, we exploited intravital microscopy by taking advantage of the novel fluorecent probe for NO (CuFL) and the dorsal skinfold chamber model on living tumour-bearing mice subjected to photodynamic therapy (PDT).

Notably, the PDT-triggered bystander effect was associated to the generation of very fast NO and Ca^{2+} waves within the whole tumour mass, supported the hypothesis that constitutive NOS activity might be crucial for the beneficial spread of bystander response and death signals propagation. Additionally, we demonstrated that PDT triggered apoptosis in bystander cells, through gap junction intercellular communication.

Finally, our results, provide the first direct evidence of NO involvement in bystander responses within a three-dimensional tumour mass, and strikingly corroborate the notion that connexin gap junction are instrumental for mediating bystander death signals propagation.

Riassunto

La morte cellulare e l'effetto bystander rappresentano degli elementi decisivi per l'efficacia della terapia antitumorale nonchè per la modulazione della risposta immunitaria contro il cancro. Per "effetto bystander" si intende il processo per il quale le cellule non soggette a determinati trattamenti farmacologici subiscono indirettamente gli effetti terapeutici, siano essi positivi o negativi, risultanti dal trattamento esclusivo delle cellule vicine. Nonostante siano state proposte diverse molecole e vie di segnalazione coinvolte nell'effetto bystander, i messaggeri molecolari essenziali ed i meccanismi che sottendono alla propagazione dei segnali di morte non sono ancora noti. Diversi studi suggeriscono un coinvolgimento dell'ossido nitrico (NO) e delle specie reattive dell'azoto (RNS) nell'effetto bystander tuttavia, il loro ruolo nel processo non è tuttora totalmente chiaro, considerato che essi possono sia inibire che sostenere la progressione del tumore. Inoltre, i metodi tradizionalmente usati per lo studio dell'ossido nitrico non riflettono necessariamente la produzione di NO in tempo reale nè consentono studi su complesse masse tumorali tridimensionali.

L'obiettivo principale di questo studio è stato quello di individuare e caratterizzare i segnali cellulari responsabili dell'effetto bystander all'interno del microambiente tumorale, rivolgendo particolare attenzione all'NO. A questo scopo, abbiamo utilizzato delle tecniche di microscopia intravitale, avvalendoci di una nuova sonda fluorescente per l'NO (CuFL) e del modello sperimentale delle camerette dorsali impiantate su topi affetti da tumore e sottoposti a terapia fotodinamica (PDT).

Da questo studio è emerso che l'effetto bystander indotto dalla terapia fotodinamica è associato alla generazione all'interno della massa neoplastica di onde molto rapide di segnali di NO e di Ca^{2+}. Questi eventi avallano l'ipotesi che l'attività delle isoforme costitutive dell'enzima NOS possa esercitare un ruolo cruciale nella diffusione delle risposte bystander e nella trasmissione dei segnali di morte. Questo lavoro inoltre ci ha consentito di dimostrare che la terapia fotodinamica è in grado di indurre l'apoptosi delle cellule vicine non trattate (bystander) attraverso i meccanismi di comunicazione intercellulare mediati dalle giunzioni comunicanti.

Infine, i risultati ottenuti hanno fornito la prima evidenza diretta della partecipazione dell'NO all'effetto bystander all'interno di una massa tumorale tridimensionale e corroborano efficacemente l'ipotesi che le giunzioni comunicanti formate da connesine siano essenziali per garantire la propagazione dei segnali di morte osservati nell'effetto bystander.

Introduction

Cancer represents the major public health problem for modern society. Despite major advances in conventional treatment, in the last 20 years the 5-year survival of many cancer patients has increased less than 10%. This poor clinical outcome illustrates an unmet clinical need for new therapeutic approaches, providing an effective long-lasting protection against disease recurrence. Since cell growth and cell death are two strictly regulated biological events that ultimately depend on the establishment of networks among neighbouring cells, the understanding of the molecular mechanisms underpinning intercellular communication within a tumour mass may represent a promising opportunity for the development of a successful cancer therapy.

Cellular communication, gap junctions and their implication in cancer biology

Cells do not live in isolation, but they receive and process a stream of information from the outside environment, thanks to a plethora of receptors capable of sensing mechanical, thermal and electrical stimuli. Moreover, cells can also receive other biological stimuli externally released, such as hormones, growth factors and cytokines, through which they indirectly establish connections to other cells. Additionally, cells may communicate directly each other through pathways requiring cell-cell contact. Direct communication among neighbouring cells is mainly mediated by gap junctions. Gap junctions (GJ) are intercellular membrane channels that typically gather in groups of 10 to 10,000, so-called plaques, at the plasma membrane surface. They arise from interaction of two opposing hemichannels, in turn consisting of six connexin proteins. Connexins are present in a wide variety of organisms. In humans, more than twenty connexin species have been characterized. They all share a similar structure of four membrane-spanning domains, two extracellular loops, one cytoplasmic loop, one cytosolic N-terminal tail, and one C-terminal region. The flux of molecules through these channels is called the gap junctional intercellular communication (GJIC) and includes the passive diffusion of ions, such as sodium, potassium and calcium and hydrophilic molecules (MW <1 kDa), such as metabolites

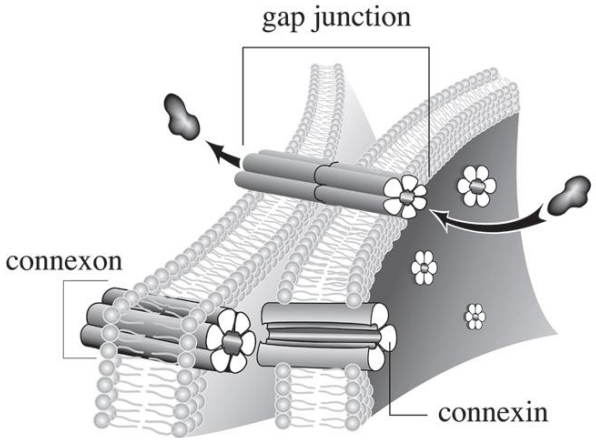

Figure1. Basic structure of the gap junction. Each intercellular gap junction channel is formed by the pairing of connexon hemichannels, located in the lateral plasma membrane of adjacent cells. Each connexon in turn is made up of six connexins. (https://www.landesbioscience.com/curie/chapter/852/)

(e.g. ADP/ATP), nutrients (e.g. glucose), and second messengers (e.g. cAMP/cGMP, IP3), resulting in the metabolic and electric coupling of cells (Alexander and Goldberg 2003). As numerous physiological processes are mediated by regulatory molecules that are exchanged via gap junctions, GJIC is considered a key mechanism in the control of virtually all aspects of the cellular life cycle (Vinken, Vanhaecke et al. 2006). The functional importance of gap junctions is widespread, with these channel proteins being expressed in nearly all excitable and non-excitable tissues of the body. For example, in excitable tissues, the establishment of direct electrical circuits is essential for cardiac muscle synchronization and neural networks. Although not molecularly defined, collective information suggests that connexins in non-excitable tissues play key roles in development, differentiation, metabolic homeostasis and growth control. One of the major differences between rat liver cancer and normal cells resides in the resistance to ion diffusion from cell to cell. Indeed, while the cells of healthy liver form a functional continuum, the cells of cancerous tissue behave like isolated functional units (Loewenstein and Kanno 1967). Connexin function is tighly regulated at the level of transcription, translation, processing, gating and protein/channel turnover. Phosphorylation of multiple serines, threonines and tyrosines, predominantly in the cytoplasmic tail, appears to contribute to the orchestration of these various regulatory steps for several connexin types (King and Bertram 2005). Moreover, connexin channels gating, which occurs within milliseconds, is triggered by a number of factors, including transmembrane voltage (voltage gating), and H^+ and Ca^{2+} ions (chemical gating). Numerous reports described variation in connexin expression according to different phase of cell cycle, thus claiming an important role in controlling cell growth. Moreover, during the last few years, most attention has been paid to unravelling GJ involvement in programmed cell death (Vinken, Vanhaecke et al. 2006). Apoptotic cell death is generally associated with drastic alterations in Ca^{2+} concentration, which is frequently exchanged via gap junctions, thus spreading the death wave from cell to cell (Contreras, Sanchez et al. 2004). Furthermore, inositol triphosphate (IP3), even if not sufficient for the spread of apoptosis – since it needs to team up with other factors to become a fully pro-apoptotic messenger – is a key necessary messenger for communicating apoptotic cell death via gap junctions (Decrock, Krysko et al. 2012). Additionally, different evidence supports the claim that connexins fulfil tumour suppression functions and, as tumour suppressor genes, their expression or function must also be abrogated to allow carcinogenic progression. First, connexins and/or gap junctions are typically downregulated in cell lines that are derived from various tumour types (Loewenstein and Kanno 1967). Second, rodent or human solid tissue tumours often lack gap junctions and exhibit reduced connexin levels. Intriguingly, numerous studies have demonstrated that human cancers are deficient in GJ either as a result of a downregulated expression of connexins, altered trafficking to the cell membrane or the inability to form functional junctions. Immunohistochemical analysis of primary excised human tumours revealed, indeed, downregulation of connexin expression in several cancer types, including lung, renal, endometrial

and breast carcinomas, gliomas, cervical and prostate carcinomas (King and Bertram 2005). Third, reagents and oncogenes that promote either tumour onset or progression frequently inhibit gap junction channel function and/or reduce connexin expression. Fourth, differential or subtractive gene profiling, as well as gene knockdown studies, have identified connexins as potential tumour suppressors. Fifth, ectopic reintroduction of connexins into tumour cells reduces cell proliferation and tumour growth, and partially re-differentiates transformed cells. Last, some connexin-knockout mice, as well as mice expressing reduced or dominant-negative connexins, have an increased incidence of tumour onset when challenged with a carcinogen. In addition to these lines of evidence linking connexins to cancer, other correlative studies have shown that retinoids and carotenoids might be involved in cancer prevention by upregulating connexins and GJIC through their nuclear retinoic acid receptor (RAR) (Chung, Choi et al. 2010).

Noteworthy, a recent study demonstrated that reduced expression of Cx43 in the cytoplasm of human colorectal tumours is associated with significantly poorer clinical outcome, thus suggesting that Cx43 could serve as prognostic biomarker to predict disease outcome (Sirnes, Bruun et al. 2012). Moreover, connexins expression and GJ networks may assume clinical relevance since their overexpression enhance the extent of tumour cell death, by allowing the transfer of toxic metabolites among neighbouring cells, thus assuring the so-called "bystander effect" of antitumour therapy by either pro-drugs (Mesnil, Piccoli et al. 1996) or other chemotherapeutic agents (Garcia-Rodriguez, Perez-Torras et al. 2011).

Cancer therapy and the bystander effect

The 'bystander effect' refers to a process whereby untreated cells exhibit either the deleterious or beneficial indirect effects as a result of signals received from nearby targeted cells. Most frequently, directly irradiated cells forward damaging signals to non-irradiated cells thereby inducing a response similar to that of irradiated ones (Baskar 2010). Despite radiation-induced bystander effects have become established in the radiobiology vocabulary as *a bona fide* radiation response, there is still no consensus on the precise definition of the radiation-induced bystander effect itself, which currently encompasses a number of distinct signalling-mediated events (Blyth and Sykes 2011). Notwithstanding, the bystander effect has been observed in response to a range of different insults including ultraviolet radiation, photodynamic therapy, heat and chemotherapy agents and is thought to involve direct cell–cell interactions through gap junctional intercellular communication (GJIC), requiring expression and surface location of connexin proteins (McMasters, Saylors et al. 1998; Garcia-Rodriguez, Perez-Torras et al. 2011). The hypothesis of metabolic cooperation to explain the bystander effect was supported by the transfer of toxic derivatives within the archetypal gene therapy model based on the herpes simplex virus-thymidine

kinase (HSV-TK) expression. TK/GCV system is probably the best documented example of a therapy that benefits from a bystander effect mediated by the traffic of phosphate derivatives through gap junctions. In this therapy, infact, cells are transfected with the HSV-TK gene and are thus incubated with the non-toxic agent ganciclovir (GCV), which is converted to a toxic analogue that diffuses and kills neighbouring cells, even if they were not transfected with HSV-TK (Mesnil and Yamasaki 2000). In this context, the bystander effect involved direct cell–cell communication through GJIC and required expression and surface location of Cx43 gap junctions (McMasters, Saylors et al. 1998). Moreover, a more recent study demonstrated that Cx26 participates in the gap junction–mediated bystander cytoxic effect of gemcitabine, providing evidence that upregulation of Cx26 improves gemcitabine anticancer efficacy on human pancreatic tumour cells (Garcia-Rodriguez, Perez-Torras et al. 2011). Surprisingly, a key characteristic of the radiation-induced bystander responses, in contrast to direct irradiation effects, is the a typical dose–response relationship.

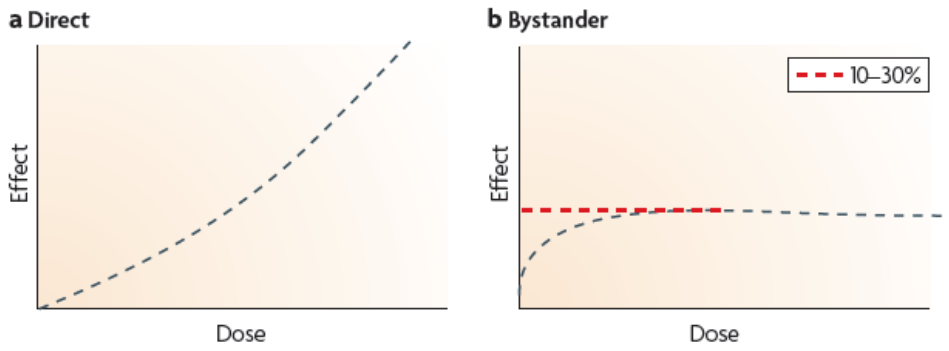

Figure2. Key aspects of radiation-induced bystander responses. Typical dose response curves for direct (a) and bystander (b) responses are shown, highlighting the commonly observed saturation of response for bystander effect (Prise and O'Sullivan 2009).

Instead of an increased response with increasing radiation dose, in fact, the bystander response becomes saturated at relatively low doses (typically less than 1 Gy). This saturation means that, above a sort of dose threshold level, no additional effect occurs, therefore not every nearby cell is engaged in the bystander effect. It has also been suggested that bystander effect might be triggered in a binary mode as a simple on–off response, whose probability increases with radiation dose. It should be emphasized, however, that bystander responses can have a significant role even after high doses (>10 Gy). Interestingly, in many models after low-dose exposure bystander responses are almost equally effective as the direct response, suggesting that at least under some conditions bystander responses could predominate in overall effectiveness. From a molecular point of view, radiation-induced bystander response is based on two main mechanisms of action, which involve both directly contacting cells via gap junctions and not physically connected cells through the release of soluble factors.

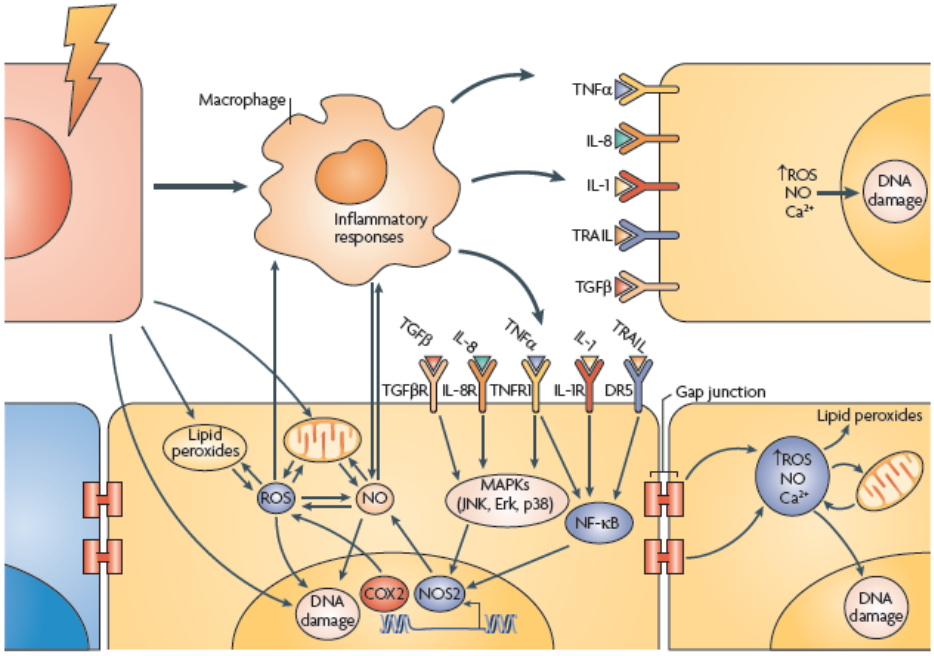

Figure3. Key pathways affecting bystander signals. Cells respond to direct radiation (red cell) by producing bystander responses through two key routes. One involves direct cell–cell communication through gap junctions and the second release of cytokine signals into the extracellular matrix. Not all cells respond (for example, the blue cell). *In vivo*, macrophages may be important mediators, which in response to radiation-induced tissue damage release bystander signals that affect non-irradiated cells (yellow cells). Some of the key pathways and mechanisms are now being elucidated, with roles for cytokine-mediated signalling, signal transduction through MAPKs and nuclear factor-κB (NF-κB) alongside the production of reactive oxygen and nitrogen species. COX2, cyclooxygenase 2; DR5, death receptor 5 (also known as TNFRSF10B); IL, interleukin; JNK, Jun N terminal kinase; NO, nitric oxide; NOS2, NO synthase 2; ROS, reactive oxygen species; TGFα, transforming growth factor-β; TGFβR, TGFβreceptor; TNFα, tumour necrosis factor-α; TRAIL, TNF-related apoptosis inducing ligand (Prise and O'Sullivan 2009).

These factors, preferentially transferred through extracellular medium from irradiated to non-irradiated cells, include lipid peroxide products, inosine nucleotides and cytokines such as tumour necrosis factor-α (TNFα). Moreover, reactive oxygen species (ROS), such as superoxide radicals, are vividly involved in bystander cell signals (Prise and O'Sullivan 2009). Several reports have shown a key role for cytokines, including interleukin 6 (IL-6), IL-8, transforming growth factor-β1 (TGFβ1) and TNFα, as well as ROS and reactive nitrogen species (RNS), relating the bystander-mediated signalling to inflammatory responses. For example, recent studies have shown that macrophages, which are key mediators of the inflammatory response and distinctive components of tumour microenvironment (Balkwill and Mantovani 2012), produce persistent levels of oxidative stress mediators after radiation exposure under bystander conditions, due to the activation of cyclooxygenase 2 (COX2) and inducible nitric oxide (NO) synthase (iNOS). Khan et al. found that pre-injection of rat with either superoxide dismutase (SOD) or the NOS inhibitor L-NAME led to a reduced response in the

non-irradiated shielded lung areas, indicating the involvement of ROS and NO in irradiation-induced bystander DNA damage, which is reported to be accompanied by waves of macrophage activation and production of cytokines, including IL-1α, IL-1β, IL-6, TNFα and TGFβ, lasting up to 16 weeks after irradiation (Khan, Van Dyk et al. 2003). Furthermore, a growing number of findings support the importance of NO in intercellular signal transduction pathways initiated by ionizing radiation. Irradiation with helium ions of individual glioblastoma cells and subsequent co-culture with non-irradiated cells in the presence of either a NOS inhibitor or anti-TGFβ1 antibody demonstrated that both TGFβ1 and NO were released independently from irradiated cells and induced a burst of free radicals and DNA damage in neighbouring cells. Additionally, stimulation of NO release influenced the increase in TGFβ1 production and, inversely, TGFβ1 stimulated the accumulation of iNOS, demonstrating a positive feedback between these two pathways (Shao, Folkard et al. 2008; Shao, Prise et al. 2008).

Tumour microenvironment heterogeneity and antitumour immunity

Since the last decade it became generally accepted that tumour mass are not only a collection of relatively homogenous cancer cells, but they rather form a sort of crowded organ composed of different cell populations, sustaining inflammation. Inflammation has indeed been extensively associated to cancer and the mediators and cellular effectors of inflammation are considered important constituents of the tumour microenvironment (Mantovani, Allavena et al. 2008; Grivennikov, Greten et al. 2010). The connection between cancer and inflammation dates back to 1863, when Rudolf Virchow noted leucocytes in neoplastic tissues, suggesting that the "lymphoreticular infiltrate" reflected the origin of cancer at sites of chronic inflammation (Balkwill and Mantovani 2001). Moreover, smouldering inflammation increases the risk of developing many types of cancer, including bladder, cervical, gastric, intestinal, oesophageal, ovarian, prostate and thyroid cancer (Porta, Riboldi et al. 2011), thus representing one of the novel additional hallmarks of cancers, namely sustaining proliferative signalling, evading growth suppressors, resisting cell death, enabling replicative immortality, inducing angiogenesis, activating invasion and metastasis, reprogramming energy metabolism, and evading immune destruction (Hanahan and Weinberg 2011). As a result of chronic inflammation, tumour microenviroment harbours different corrupted resident or purposely recruited cells which exert conflicting functions establishing a peculiar cytokine milieu. However, the stromal components of tumour microenvironment can be classified into three general classes: angiogenic vascular cells, cancer-associated fibroblastic cells and infiltrating immune cells (Hanahan and Coussens 2012).

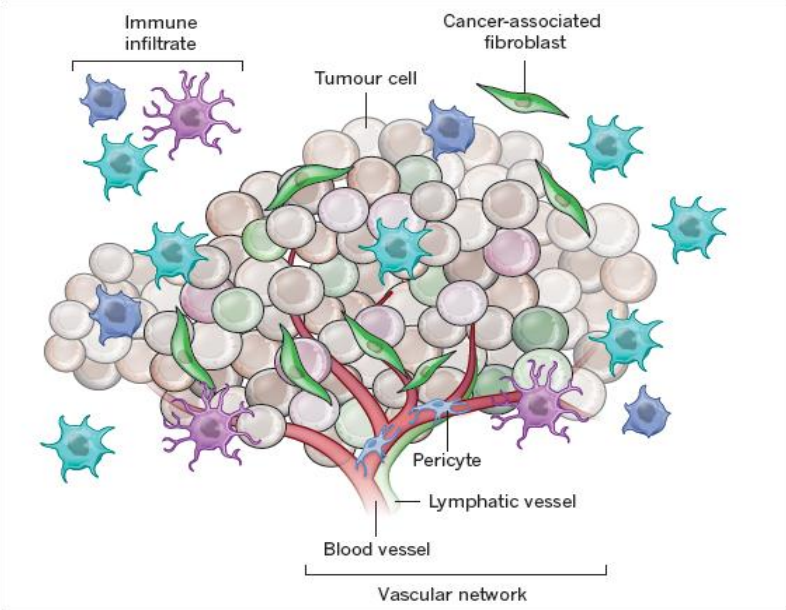

Figure4. Tumour microenvironment heterogeneity. Tumour microenviroment is a dynamic niche where vascular, immune and fibroblastic cells cluster. Infiltrating immune cells can include multiple cell types that provide both pro- and anti-tumour support. The vascular endothelial networks differ in regard to the vessel's tissue of origin and require accumulation of immature pericytes. Finally, cancer-associated fibroblasts drive tissue remodelling enhancing tumour invasiveness (Junttila and de Sauvage 2013).

Angiogenic vascular cells, accumulated within the neoplastic lesion thanks to pro-angiogenic factors – primarily vascular endothelial growth factor (VEGF) – secretion by tumour itself, restore the oxygen and nutrients supply to cancer cells, which would not otherwise survive in hypoxic conditions. Nonetheless, endothelial cells as well as pericytes – the mural cells of blood microvessels involved in endothelial cell stimulation and guidance, endothelial stabilization and maturation – arrange themselves in a pathological anarchic manner, thus facilitating dissemination of cancer cells from primary tumour (Raza, Franklin et al. 2010). Cancer-associated fibroblasts (CAFs), differently from normal fibroblasts, which typically suppress tumour formation, show pro-tumourigenic properties, since they enhance tissue remodelling, by increasing expression of proteolytic enzymes, such as matrix metalloproteinases, and extracellular matrix deposition (Junttila and de Sauvage 2013). Moreover CAFs secrete distinctive factors as the stromal cell-derived factor 1 (SDF1), VEGF, the platelet-derived growth factor (PDGF), and the hepatocyte growth factor (HGF), promoting immune cell recruitment at tumour site (Polanska and Orimo 2013). Notably, the different number, type and location of tumour infiltrating immune cells reflect peculiar biological aspects of individual cancers. Interestingly, large studies have proven that tumour immune infiltrate patterns and subsets in colorectal cancer are significant prognostic biomarkers (Ogino, Nosho et al. 2009; Nosho, Baba et al. 2010) thus paving the way for the clinical introduction of a novel parameter, the so-called "immunoscore". This new index supports cancer staging and identifies patients with high-risk of tumour recurrence, thus facilitating clinical decision-

making including rational stratification of patients who would benefit the most from adjuvant therapy. The "immunoscore" looks at the immune cell density, calculated by numerical quantification of two lymphocyte populations, cytotoxic and memory T cells both at the tumour core and the invasive margin (Galon, Pages et al. 2012). Tumour-infiltrating immune cells include however cell subsets belonging to both the adaptive and the innate immune compartments. Interestingly, very recent studies demonstrated the existence of peculiar organized tertiary lymphoid structures (TLS) within the tumours, consisting of segregated B and T cells, in the presence of high endothelial venule-like vasculature structures (Goc, Germain et al. 2013). Besides conventional B cells and αβ TCR–expressing $CD8^+$ and $CD4^+$ T cells crowding to the primary neoplastic lesion, natural killer (NK) cells, γδ T cells and natural killer T (NKT) cells are present within the tumour microenvironment. The role of these innate lymphocyte subsets in modulating immune response in cancer settings has not yet clearly elucidated, since they seem to either promote or suppress T cell activation depending on the cytokine milieu (Gajewski, Schreiber et al. 2013). Moreover, among myeloid cell populations observed at tumour site, there are both terminally differentiated cells, as dendritic cells (DCs), macrophages and granulocytes, and immature myeloid cells, named as myeloid-derived suppressor cells (MDSCs), which are generated from bone marrow as a consequence of a cancer-induced abnormal myelopoieis (Gabrilovich, Ostrand-Rosenberg et al. 2012). Nonetheless, DCs in tumour-bearing hosts do not adequately stimulate an effective immune response because of the down-regulated expression of the MHC class II and co-stimulatory molecules CD80 and CD86, thus favouring tumour immune evasion (Gabrilovich 2004). Macrophages flocked to the tumour, the so-called tumour associated macrophages (TAMs), generally show peculiar characteristics, typical of those macrophages exhibiting an M2 phenotype.

While M1 or 'classically activated' macrophages – stimulated by IFNγ and bacterial products and expressing high levels of IL-12 and low levels of IL-10 – are tumouricidal, M2 or 'alternatively activated' macrophages – activated by IL-4, IL-10, IL-13 and glucocorticoid hormones and secreting high levels of IL-10 and low levels of IL-12 – favour tumour progression (Mantovani, Sozzani et al. 2002). M2 macrophages display, infact, poor antigen presenting capacity, promote angiogenesis and lymphangiogenesis, sustain tissue remodelling, tumour invasion and metastasis, and suppress anti-tumoural adaptive immunity (Galdiero, Garlanda et al. 2013). Similarly to macrophages, tumour-associated granulocytes, which are prominently neutrophils, have been shown to shift from an antitumoural 'N1' phenotype to a pro-tumoural 'N2' phenotype after TGF-β exposure, which is frequently secreted by cancer cells. Whilst N1 TANs showed high expression of immunoactivating cytokines and chemokines, low levels of arginase, and high capability of killing tumour cells *in vitro*, N2 TANs exhibit pro-tumoural properties (Fridlender, Sun et al. 2009). Finally, MDSCs include direct progenitors of DCs, macrophages and granulocytes and exploit multiple redundant mechanisms to influence both innate and adaptive immune responses. First,

MDSCs induce the activation and expansion of regulatory T cells (T_{reg}) population by promoting antigen-specific natural T_{reg} clonal expansion and naive $CD4^+$ T cell conversion into induced T_{reg} cells. The second immunomodulating mechanism is based on nutrients depletion required by lymphocytes, i.e. L-cysteine sequestration and L-arginine depletion through arginase-1 (ARG1) dependent consumption, which cause TCR ζ-chain down-regulation and the proliferative arrest of antigen-activated T cells. Moreover, MDSCs interfere with lymphocyte trafficking and viability, by expressing at the plasma membrane ADAM17 (disintegrin and metalloproteinase domain-containing protein 17), which cleaves key proteins for T cell recirculation to lymph nodes, and galectin-9 (GAL-9), which induce T cell apoptosis. Finally, MDSCs produce ROS, NO and other RNS, thus sustaining oxidative stress within tumour microenvironment, by the synergistic activity of ARG1, iNOS and NADPH oxydase enzymes (Gabrilovich, Ostrand-Rosenberg et al. 2012).

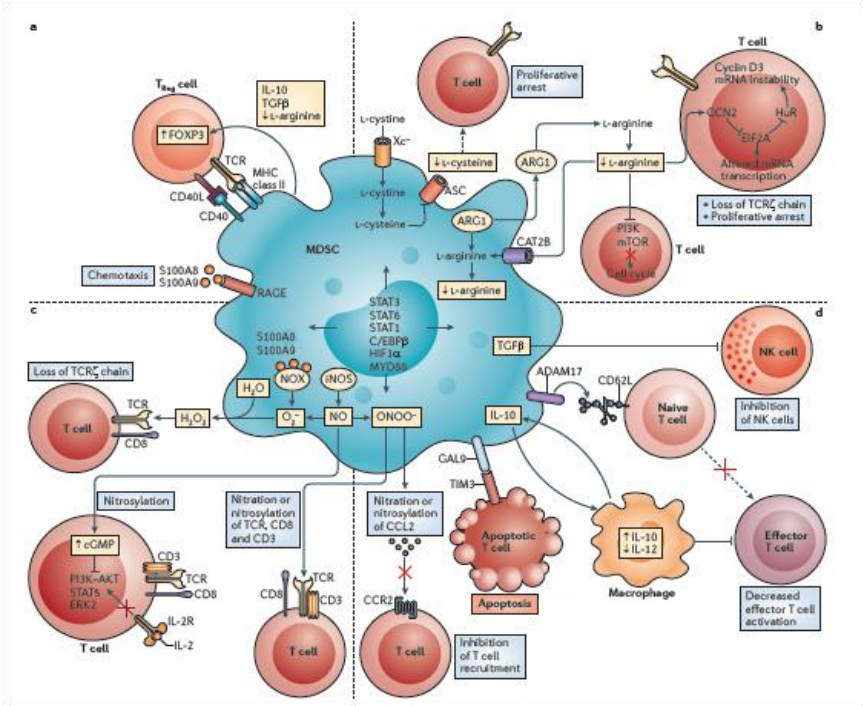

Figure5. Mechanisms of MDSC-dependent inhibition of T cell activation and proliferation. Myeloid-derived suppressor cells (MDSCs) can inhibit efficient antitumour T cell responses through a number of mechanisms. a) Tumour-associated MDSCs induce the development of regulatory T (T_{reg}) cells or expand existing T_{reg} cell populations. b) Tumour-associated myeloid cells deprive T cells of amino acids that are essential for their growth and differentiation. c) Tumour-associated myeloid cells release oxidizing molecules, such as hydrogen peroxide (H_2O_2) and peroxynitrite (ONOO–) which cause nitration and nitrosylation of components of the T cell receptor (TCR) signalling complex, and the loss of the TCR ζ-chain, thereby inhibiting T cell activation through the TCR. d) Tumour-associated myeloid cells can also interfere with T cell migration and viability through ADAM17 and GAL9 expression. (Gabrilovich, Ostrand-Rosenberg et al. 2012).

The dual role of nitric oxide in cancer biology

Nitric oxide (NO) is a lipophilic, highly diffusible, and short-lived physiological messenger (Lancaster 1997), which modulates a variety of important biological process. In particular, low NO concentration acts as a physiological signal transducer in many physiological processes, such as blood flow regulation, smooth muscle relaxation, iron homeostasis, platelet reactivity and neurotransmission. Conversely, high NO concentrations serve as a cytotoxic defensive mechanism against pathogens and, perhaps, tumours (Mocellin, Bronte et al. 2007). Several investigators have reported the expression of iNOS by malignant cells or within the tumour rmicroenvironment, both at mRNA and protein level. In breast carcinoma, an initial study suggested that iNOS activity was higher in less differentiated tumours and detected predominantly in TAMs (Thomsen, Miles et al. 1995). Subsequently, other reports demonstrated that iNOS was also expressed by breast carcinoma cells and positively correlated with tumour stage (Thomsen, Miles et al. 1995; Reveneau, Arnould et al. 1999) and microvessel density (Zhang, He et al. 2011). In addition to breast cancer, iNOS is markedly expressed in approximately 60% of human colon adenomas and in 20%–25% of colon carcinomas, while the expression is either low or absent in the surrounding normal tissues. Similar results were obtained for human ovarian cancer and melanoma. Other cancers that express iNOS are head and neck, esophagus, lung, prostate, bladder and pancreatic carcinomas, brain tumours, Kaposi's sarcoma, mesothelioma, and hematological malignancies. Moreover, the endothelial NOS isoform (eNOS) has been found in both endothelial and tumour cells of breast carcinomas, and the neuronal NOS isoform (nNOS) has been detected in some oligodendroglioma and neuroblastoma cell lines. However, the role of NO in cancer biology has not been clearly elucidated yet, since various studies have shown that NO may either promote or inhibit tumour progression and metastasis. The net effect of NO in tumours seems to depend on the activity and localization of NOS isoforms, concentration and duration of NO exposure, cellular sensitivity and hypoxia/re-oxygenation process within tumour microenvironment (Fukumura, Kashiwagi et al. 2006). In general, high concentrations of NO and RNS can arrest cell cycle (cytostatic effect) or induce cell death, whereas low concentrations may protect cells from apoptosis. Infact, generation of high levels of NO/RNS is a very effective tool to induce cell death, and macrophages use it as a major weapon in their arsenal against invading pathogens and tumour cells (Weigert and Brune 2008). High levels of NO/RNS post-translationally modify death-related target proteins, as the death receptors of the TNFα superfamily, and block respiration in target cells by affecting the mitochondrial respiratory chain and its outer membrane permeability and thus leading to the release of cytochrome c and apoptosis initiation (Leon, Jeannin et al. 2008). Moreover, high NO concentrations, oxidizing and/or deaminating the DNA bases, result in DNA breaks, DNA base modifications or DNA cross-links, which cause mutations that may either activate oncogenes or deactivate tumour suppressor genes. In addition, NO/RNS-driven protein modifications such as S-

nitrosylation or nitration may inhibit proteins belonging to the DNA repair systems, driving to genomic instability (Lechner, Lirk et al. 2005). Importantly, DNA damages that cannot be repaired, cause apoptosis induction, by the activation of DNA-damage-sensing proteins (e.g., p53, PARP, DNA-PK, BRCA1, ATM) (Norbury and Zhivotovsky 2004). However, NO has been demonstrated to inhibit programmed cell death in endothelial cells and some liver cancer cell lines, mainly through S-nitrosylation of the active-site cysteine of caspases (Dimmeler, Haendeler et al. 1997), thus perpetuating mutations and consequently sustaining transformation (Torok, Higuchi et al. 2002; Muntane, De la Rosa et al. 2013). On the other hand, NO may induce apoptosis either via downregulation of the anti apoptotic protein survivin, as observed in human lung carcinoma cells (Chao, Kuo et al. 2004), or upregulation of Fas expression, as shown in ovarian carcinoma cell lines, through the specific inactivation of the transcription repressor yin-yang-1, which binds to the silencer region of the Fas promoter (Garban and Bonavida 2001). Besides enhancing citotoxicity, NO plays a role in angiogenesis and metastasis since several reports showed a positive correlation between NOS expression/activity in tumour tissues and lymphatic metastasis in head and neck, thyroid, breast, stomach, gallbladder cancers (Fukumura, Kashiwagi et al. 2006; Lahdenranta, Hagendoorn et al. 2009) and melanoma (Massi, De Nisi et al. 2009).

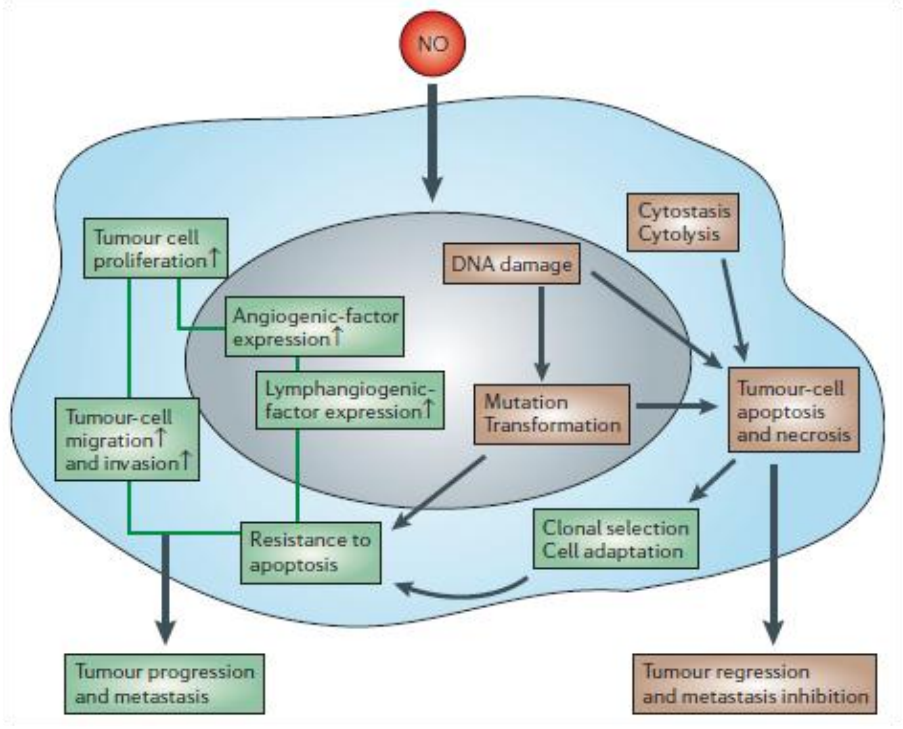

Figure6. Mechanisms of action of NO on tumour cells. NO can induce both tumour progression and metastasis (green) and tumour regression and inhibition of metastasis (brown) depending on the dose and duration of NO exposure and on cellular sensitivity to NO. NO promotes tumour progression and metastasis by direct induction of tumour-cell proliferation, migration and invasion, and indirectly through the expression of angiogenic and lymphangiogenic factors in tumour cells. On the other hand, the cytotoxic effects of NO that are typically induced by high doses promote DNA damage, gene mutation and tumour-cell death, which result in tumour regression and inhibition of metastasis (Fukumura, Kashiwagi et al. 2006).

As under physiologic conditions, NO maintains blood flow by dilatation of arterial vessels, promotes perivascular cell recruitment and vessel remodelling and maturation within tumours (Fukumura, Kashiwagi et al. 2006). NO exposure of A-431 squamous carcinoma cells and MDA-MB-231 breast cancer cells was, infact, able to induce VEGF-C expression, which mediates lymphangiogenesis and metastasis (Franchi, Massi et al. 2006). However, NO may also inhibit the aggregation of platelets through a cGMP-dependent mechanism, preventing aggregates formation with tumour cells, which may facilitate their adhesion to vascular endothelial cells and haematogeneous dissemination (Mehta 1984). Finally, as previously mentioned, NO/RNS can suppress tumour-specific adaptive immunity through several mechanisms. One mechanism involves the inhibition of phosphorylation, and thereby the activation of important signalling proteins in the IL-2-receptor pathway (including Janus activated kinase 1 (JAK1), JAK3, STAT5, extracellular-signal-regulated kinase (ERK) and AKT) in T cells (Bingisser, Tilbrook et al. 1998). Additionally, NO promotes tumour immunosuppression, by affecting the stability of IL-2 encoding mRNA and the release of IL-2 by activated human T cells (Macphail, Gibney et al. 2003). Finally, NO/RNS may dampen antitumour immunity through post-translational modifications of key proteins for T cell activation, such as CD8 and TCR complex α/β chains molecules (Nagaraj, Gupta et al. 2007), and T lymphocyte recruitment to the tumour site, such as the chemokine CCL2 (Molon, Ugel et al. 2011).
Thus, interfering with NO/RNS production within tumour microenvironment may represent a promising successful strategy to implement the efficacy of antitumour therapy alone or, even better, in combination with conventional chemotherapy, radiotherapy, photodynamic therapy and immunotherapy approaches.

Structure and function of NOS enzymes

The enzymes responsible for the generation of endogenous NO through L-arginine oxidation in mammals are known as NO synthases (NOS). Three quite distinct isoforms of NOS have been identified. These isoforms are referred by the most common nomenclature: nNOS (also known as Type I, NOS-I and NOS-1) being the first isoform found and predominating in neuronal tissue; iNOS (also known as Type II, NOS-II and NOS-2), which is inducible in a wide range of cells and tissues, primarily in macrophages; and eNOS (alsoknown as Type III, NOS-III and NOS-3) predominantly found in endothelial cells. nNOS synthesizes NO in a neuron in response to glutamate while iNOS produces NO in a macrophage following its induction by cytokines and microbial products; eNOS generates NO in a vascular endothelial cell in response to acetylcholine (Knowles and Moncada 1994). These different enzymes are products of different genes, with different localization, regulation, catalytic properties and inhibitor sensitivity, and with 51-57% homology between the human isoforms, suggesting the existence of a common ancestral NOS gene. The nNOS gene appears to be an intron-containing gene of at least 20 kb, and is unequivocally localized to a single position on

human chromosome 12 (Hall, Antoniou et al. 1994). The iNOS gene maps to chromosome 17 (Charles, Palmer et al. 1993), whereas eNOS gene is located on chromosome 7 (Janssens, Shimouchi et al. 1992). Whilst both nNOS and eNOS are commonly considered constitutive enzymes, since they are permanent cell and tissue constituents, even if expressed at low levels, iNOS remain virtually not expressed unless induced by endotoxins, such as lipopolysaccharides (LPS), or inflammatory cytokines such as IFN-γ and TNF-α (Alderton, Cooper et al. 2001). All NOS enzymes are usually referred to as `dimeric' in their active form, even if they require calmodulins (CaMs), thus forming tetramers of two NOS monomers associated with two CaMs (Crane, Arvai et al. 1998). Nevertheless, only nNOS and eNOS activity is considered calmodulin/Ca^{2+} dependent, having a much higher Ca^{2+} requirement than iNOS. Infact, for half-maximal activity NOS purified from cells other than macrophages requires Ca^{2+} concentrations of 200-400 nM, which exceed the 70-100 nM levels in resting cells (Cheung 1980). In contrast, CaM associates with iNOS at Ca^{2+} concentrations in the range of 39 nM, therefore even in cells whose Ca^{2+} remains at the resting level (Cho, Xie et al. 1992). All NOS isoforms exhibit a bidomain structure with an N-terminal oxygenase domain containing binding sites for haem and (6R)-5,6,7,8-tetrahydrobiopterin (BH4) cofactors, and a C-terminal reductase domain contains binding sites for NADPH and for FAD and FMN cofactors (Crane, Arvai et al. 1997). CaM binding at its binding site located between the two NOS domains, increases the rate of electron transfer from NADPH to the reductase domain and triggers electron transfer from the reductase domain to the haem centre (Matsuda and Iyanagi 1999). CaM effect is however only kinetic, rather than thermodynamic, since CaM-Ca^{2+} binding has little effect on redox potential of the flavins (Noble, Munro et al. 1999).

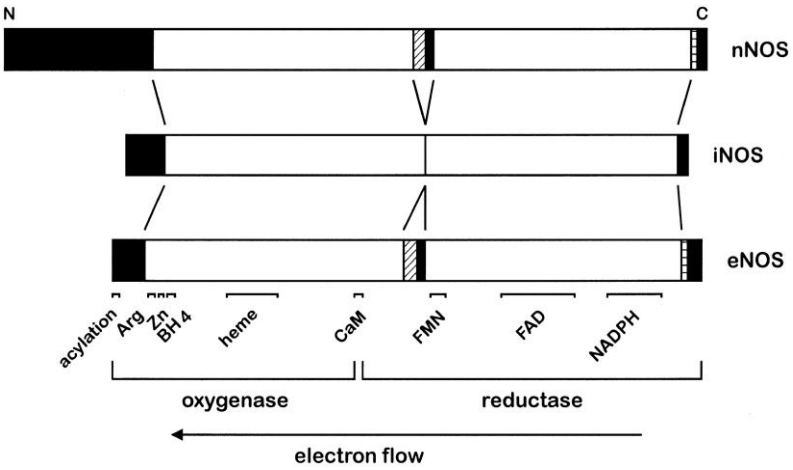

Figure8. Structure of nitric oxide isoforms. NH_2(N) and COOH(C) termini are indicated. Homology in amino acid sequences are depicted: open boxes, homologous regions; hatched boxes, homologous in neuronal (nNOS) and endothelial nitric oxide synthase (eNOS); solid boxes, isoform-specific sequences. For eNOS, regions involved in acylation and binding of substrates and cofactors are indicated, as well as the oxygenase and reductase domain and the direction of the intramolecular electron flow. Arg, arginine; BH4, tetrahydrobiopterin; CaM, calmodulin; FMN, flavin mononucleotide; FAD, flavin adenine dinucleotide (Govers and Rabelink 2001).

Noteworthy, the reason why NOS monomer is not active resides in a peculiar electron flow, which requires that the reductase domain of one polypeptide chain donates its electrons to the oxygenase domain of the other (Siddhanta, Wu et al. 1996). NOS dimerization involves a large interface in the oxygenase domain, including the BH4 binding site, which contributes to structure the active-site pocket (Crane, Rosenfeld et al. 1999). Moreover, BH4, together with haem and L-arginine, promotes and/or stabilizes the active dimer of all three isoforms.

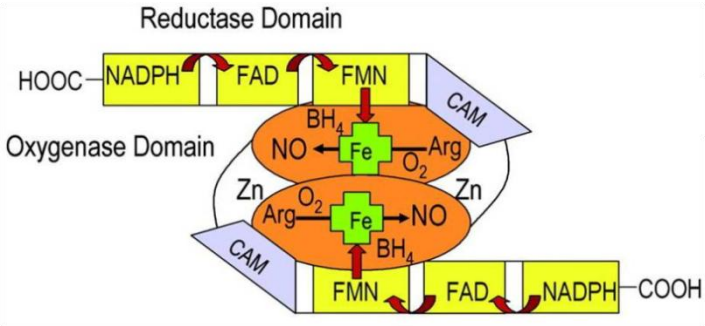

Figure9. Scheme depicting electron flow in NOS dimers. Electron flow starts from NADPH to flavins FAD and FMN of the reductase domain, which transfer the electrons to the iron of the heam in the oxygenase domain. BH4 and Calmodulin (CAM) contribute to stabilize the active dimer (Munzel, Daiber et al. 2005).

NOS catalyze the oxidative conversion of L-arginine to L-citrulline and NO by requiring NADPH and O_2 as substrates. This reaction has been divided into two major mono-oxygenation steps, which produce N^{ω}-hydroxy-L-arginine as intermediate (Stuehr, Kwon et al. 1991)

The first step of the reaction (monooxygenase I) is reported as follows:

$$\text{L-arginine} + \text{NADPH} + H^+ + O_2 \rightarrow N^{\omega}\text{-hydroxy-L-arginine} + NADP^+ + H_2O$$

Then the second step (monooxygenase II) is stated as:

$$N^{\omega}\text{-hydroxy-L-arginine} + 0.5\ \text{NADPH} + 0.5\ H^+ + O_2 \rightarrow$$

$$\text{Citrulline} + 0.5\ NADP^+ + H_2O + \bullet NO$$

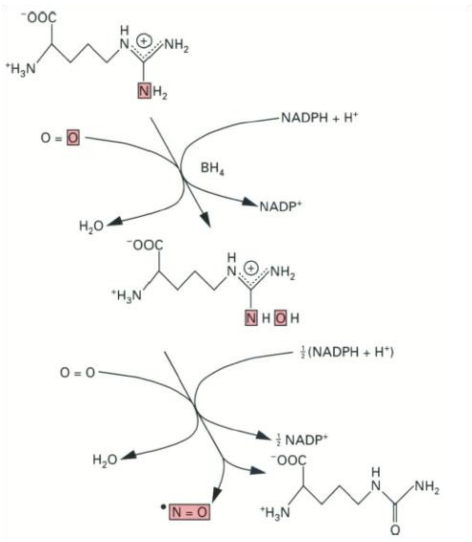

Figure10. NO synhtesis reaction steps

(Knowles and Moncada 1994).

The essential role of FAD and FMN cofactors in the reductase domain is to accept two electrons from NADPH and pass them on to a one-electron acceptor haem domain by forming stable semiquinone radical intermediates. Electron flow between the two flavins has been suggested to be the control point where CaM acts, since electron transfer from FAD to FMN is slow in the absence of CaM/Ca^{2+} (Matsuda and Iyanagi 1999). The monooxygenase II step involves the reduction of haem ferric to ferrous ion and O_2 binding. This form of the enzyme then reacts with N^{ω}-hydroxy-L-arginine to form its radical and a haem-peroxy complex. The N^{ω}-hydroxy-L-arginine radical and the peroxy complex then react with each other in a 'radical rebound' mechanism to generate citrulline and NO, and to re-generate the ferric haem iron (Alderton, Cooper et al. 2001). Interestingly, NOS activity does not only yield NO, since in the presence of superoxide dismutase (SOD), peroxynitrite ($ONOO^-$) and other RNS are detected (Schmidt, Hofmann et al. 1996). When superoxide ($O_2\bullet^-$) is not efficiently removed by the scavenging enzyme SOD accumulating at high concentrations, NO and superoxide spontaneously combine within few cell diameters, thus yielding peroxynitrite (Huie and Padmaja 1993). Physiologically, NO is efficiently removed by reacting with oxyhemoglobin to form nitrate, which prevents nitrogen dioxide formation. Nonetheless, under pro-inflammatory conditions, simultaneous production of superoxide and NO can be strongly activated, thus increasing peroxynitrite formation by a 1,000,000-fold (Pacher, Beckman et al. 2007).

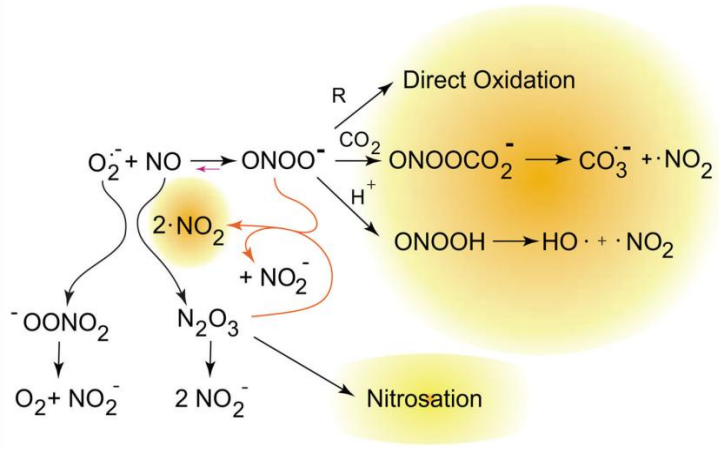

Figure11. The interplay of nitric oxide, superoxide, peroxynitrite, and nitrogen dioxide. When nitric oxide and superoxide are both present, they may also react with nitrogen dioxide to form N_2O_3 and peroxynitrate. Peroxynitrate decomposes to give nitrite and oxygen, while N_2O_3 can react with thiols to give nitrosothiols or with hydroxide anion to give nitrite (Pacher, Beckman et al. 2007).

Although the half-life of peroxynitrite is short (~10–20 ms), peroxynitrite can rapidly diffuse to nearby cells (Denicola, Souza et al. 1998) and significantly modify critical biomolecules. The most common reaction occurs under peroxynitrite exposure include cystein oxidation (Radi, Beckman et al. 1991), tyrosine nitration (Greenacre and Ischiropoulos 2001), tryptophan, methionine, and histidine oxidation on proteins (Alvarez and Radi 2003), beyond lipid peroxidation in membranes (Radi, Beckman et al. 1991) and lipoproteins and oxidation of both nucleobases and sugar-phosphate backbone on nucleic acids (Burney, Caulfield et al. 1999).

Calcium signalling in cancer

Regulation of constitutive NOS activity is not the main function of calcium ions, since Ca^{2+} is a ubiquitous intracellular signal which modulates a plethora of cellular processes. The key to this pleiotropic role is the complex spatiotemporal organization of the intracellular Ca^{2+} rise evoked by extracellular agonists, which allows selected effectors to be recruited and specific actions to be initiated (Rizzuto and Pozzan 2006). Resting cells show indeed cytosolic free Ca^{2+} concentration of 100 nM, but they may be activated when this level rises to roughly 1 μM. Ca^{2+} signalling is required for fertilization, cell proliferation and differentiation, transcription factor activation and apoptosis modulation (Berridge, Lipp et al. 2000). Since its versatile activity, it is conceivable that Ca^{2+} mediated signalling pathways play important roles in cancer initiation, tumour formation, tumour progression, metastasis, invasion and angiogenesis (Parkash and Asotra 2010). Ca^{2+} signalling pathways are, infact, remodelled or deregulated in cancer because of the altered expression of key molecules of the so-called Ca^{2+} signalling toolkit, which includes receptors and messengers able to generate Ca^{2+} signals by using both external and internal sources of Ca^{2+} ions. The Ca^{2+} toolkit includes environmental sensors and Ca^{2+} mobilizing messengers that are generated when stimuli bind to cell surface receptors, and other second messengers modulating Ca^{2+} concentration in intracellular stores (Berridge, Lipp et al. 2000). External Ca^{2+} entry is mediated by different families of Ca^{2+} channels localized on plasma membrane, which are defined by the way they are activated. Among these, there are voltage-operated channels (VOCs), activated by membrane depolarization; receptor-operated channels (ROCs), which open in response to the binding of an extracellular ligand, usually transmitters such as glutamate, ATP or acetylcholine; store-operated channels (SOCs) (Roderick and Cook 2008), which open in response to the depletion of internal Ca^{2+} stores, as the (STIM)/Ora1-mediated store-operated Ca^{2+} channels and, finally, the second messenger-operated channels (SMOCs), as the permeable transient receptor potential channels TRPCs (Berridge, Bootman et al. 2003).

Ca^{2+} release from intracellular stores is mainly mediated by the activation of the inositol 1,4,5-trisphosphate receptors (InsP3Rs) and ryanodinereceptors (RYR),

localized on the endoplasmic reticulum (ER). These two channels are regulated by several factors that involve phospholipase C (PLC) activation, but the most important is Ca^{2+} itself, which triggers the so-called Ca^{2+}-induced-Ca^{2+}-release (CICR) from intracellular stores. CICR is responsible for intercellular Ca^{2+} signal spreading and for the generation of Ca^{2+} waves capable of coordinating the activity of many neighbouring cells (Robb-Gaspers and Thomas 1995; Parkash and Asotra 2010). Once Ca^{2+} has carried out its signalling functions, it is rapidly removed from the cytoplasm to return intracellular Ca^{2+} concentration to pre-stimulation levels by various pumps and exchangers, localized both on plasma membrane and ER. These signal terminators include plasma membrane-localized Ca^{2+} ATPases (PMCA) and plasma membrane exchangers as the Na^{+}–$Ca2^{+}$ exchanger (NCX) on cell surface, and the sarco-endoplasmic reticulum ATPases (SERCA) on ER. Moreover also mitochondria, through the mitochondrial calcium uniporter (MCU) (De Stefani, Raffaello et al. 2011) and Golgi apparatus and lysosomes, contribute to maintain intracellular Ca^{2+} homeostatic levels, through the secretory pathway Ca^{2+}ATPases (SPCA) (Monteith, Davis et al. 2012; Feng and Rao 2013). Interestingly, many recent reports demonstrated deregulation of at least one of these Ca^{2+} signalling toolkit components in human tumour samples, thus providing additional evidence for the critical roles of Ca^{2+} ions in cell integrity and function maintenance. The most dysregulated channels identified in human tumours are TRPM8, ORAI1 and TRPV6 which are upregulated in prostate, breast and colon cancers; SERCA2 is downregulated in lung, colon and thyroid tumours and PMCA, whose isoforms are deregulated in breast, lung colon and oral neoplasia (Lee, Davis et al. 2011).

Moreover, ORAI1 and TRPM7 are reported to be overexpressed in human breast cancer where they promote tumour cell migration, invasion and metastasis (Chen, Chen et al. 2013) and SPCA1 and SPCA2 are upregulated in breast cancer, where they accumulate at plasma membrane thus activating ORAI1 and the downstream activation of the transcription factor NFAT (Feng, Grice et al. 2010; Grice, Vetter et al. 2010). This altered expression or activity of Ca^{2+} channels and pumps could either cause or promote cancers through modulation of Ca^{2+} concentrations in cytoplasm, ER, and mitochondria as well as spatio-temporal nature of Ca^{2+} signalling (Berridge, Bootman et al. 2003). Either the overexpression of proteins such as IP3R channels, which can cause an increase in Ca^{2+} leakage from the ER thus reducing theCa^{2+} content of the ER Ca^{2+} stores, or the reduced sequestration of Ca^{2+} as a consequence of lower levels of SERCA2 could lead to decrease in the apoptotic rates. Therefore, Ca^{2+} release from the ER and its uptake and accumulation into mitochondria play a pivotal role in triggering apoptotic signals, and one of the mechanisms through which overexpression of antiapoptotic proteins (or ablation of proapoptotic ones) counteracts cell death is the reduction in the amount of available Ca^{2+} in the ER (Rizzuto, Pinton et al. 2003).

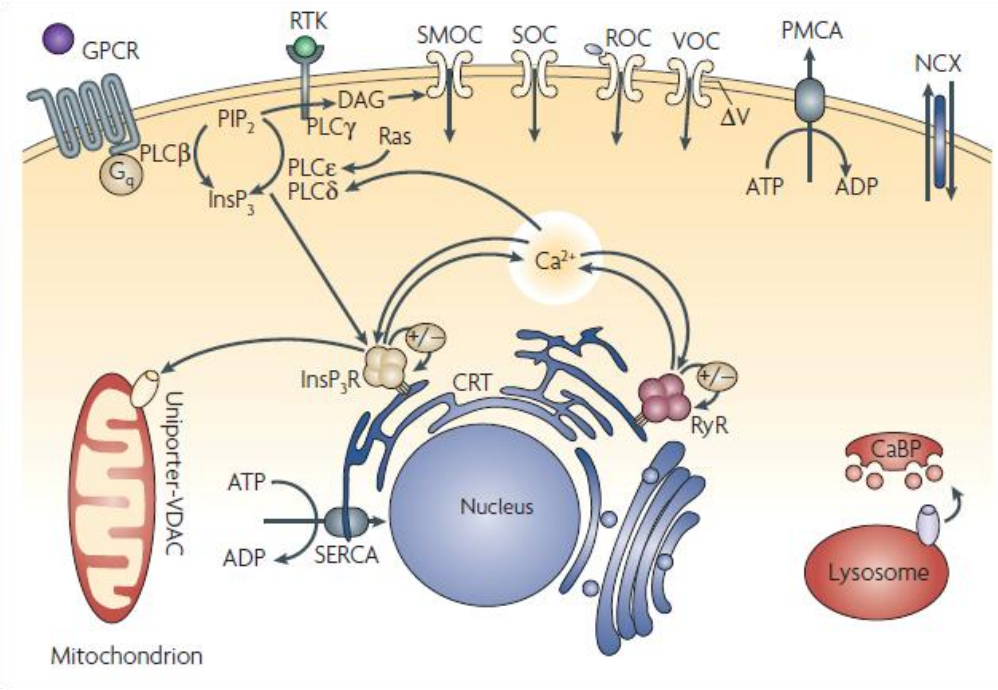

Figure12. The Ca^{2+} signalosome. In response to a change in their environment, intracellular Ca^{2+} levels increase and induce changes in cell physiology. Ca^{2+} signals are generated as a result of influx from the extracellular space through channels located at the plasma membrane (receptor-operated channels (ROCs), voltage-operated channels (VOCs), second-messenger-operated channels (SMOCs) and store-operated channels (SOCs)) or via release from intracellular stores, predominantly through inositol 1,4,5- trisphosphate receptors (InsP3Rs) or ryanodine receptors (RyRs). Ca^{2+} channels and pumps are also functionally expressed in lysosomes and the Golgi. Ca^{2+} signals return to pre-stimulated levels through the concerted action of cytosolic Ca^{2+} buffer proteins (CaBPs), mitochondria, ATP-dependent pumps on the intracellular Ca^{2+} stores (SERCA) and plasma membrane (PMCA), as well as through the Na^{+}–Ca^{2+} exchanger (NCX). Ca^{2+} is stored within the endoplasmic reticulum bound to the low-affinity, high-capacity Ca^{2+} storage protein calreticulin (CRT). DAG, diacylglycerol; GPCR, G-protein coupled receptor; PIP2, phosphatidylinositol bisphosphate; PLC, phospholipase C; RTK, receptor tyrosine kinase; VDAC, voltage-dependent anion channel (Roderick and Cook 2008).

Notwithstanding, among the calcium-related proteins that are altered in cancer microenvironment, another family, the S100 proteins, have recently drawn oncoimmunologists attention. S100 family comprises more than 25 different members, requiring calcium-induced dimer and oligomer formation for their functional activity. In addition to acting intracellularly, where they are involved in the activation of specific biochemical pathways modulatingcell proliferation, survival, differentiation and motility (Santamaria-Kisiel, Rintala-Dempsey et al. 2006), S100 proteins can be extracellularly secreted, by the activation of protein kinase C (Rammes, Roth et al. 1997), and act as chemo-attractants by actively promoting phagocyte migration (Ryckman, Vandal et al. 2003). Additionally, S100A8 and S100A9 are presumed to bind to the pathogen-recognition receptors (PRRs), including the toll-like receptor 4 (TLR4), the formyl-methionine receptors, and the receptor for advanced glycation end-products (RAGE); the

evidence that S100A9 is also apotent activator of various neutrophil functions, such as degranulation and phagocytosis, further support the S100 protein role as a danger-associated molecular patterns (DAMP) (Simard, Girard et al. 2010). Since their involvement in chronic inflammation, S100A8 and S100A9 have been also implicated in tumour development and progression (Gebhardt, Nemeth et al. 2006) and are currently being explored in the clinic as potential diagnostic markers or therapeutic targets, as enhanced expression of S100A8/A9 is associated with poor prognosis (Arai, Takano et al. 2008). Although the S100A8/A9 molecular function in growing tumours remains uncertain, the increased S100 protein expression in tumour-infiltrating myeloid cells in many epithelial tumours (Gebhardt, Nemeth et al. 2006; Salama, Malone et al. 2008) suggested that these proteins contributed to the activation and accumulation of MDSCs during the induction of tumour-immune tolerance (Sinha, Okoro et al. 2008), and to the inhibition of DC and macrophage differentiation (Cheng, Corzo et al. 2008). Moreover, S100A8/A9 binding to the RAGE receptor on colon tumour cells stimulates NF-kB signalling and activates the transcription of genes such as CXCL1 (GROa/KC), CCL2 (MCP-1), CCL5 (RANTES), and CCL7 (MCP-3) whose expression strongly promotes tumour growth, migration, invasion, and metastatic progression (Lukanidin and Sleeman 2012). Finally, recent reports showed that S100A8 and S100A9 induce the secretion of several pro-inflammatory cytokines, including IL-6, TNFα, and IL-1β by stimulating the production of ROS in human PBMCs, which, in turn, activate the transcription factor NF-kB, leading to cytokine secretion and expression and activation of the NLRP3 inflammasome (Simard, Cesaro et al. 2013). Inflammasomes, which are multiprotein complexes operating as activation platforms for caspase-1, may have contrasting roles in tumourigenesis since they positively affect cell-autonomous death pathways and anticancer immunosurveillance, but they also stimulate autocrine or paracrine processes that favour carcinogenic inflammation, tumour growth, metastasis and angiogenesis (Zitvogel, Kepp et al. 2012). Therefore, intracellular Ca^{2+} pumps and channels, but also extracellular calcium-activated proteins, as S100, may play crucial role in tumour progression and antitumour immunity, and require further investigation representing potential effective targets for novel successful therapeutic approaches.

Photodynamic therapy and antitumour immunity

The increasing incidence of cancer and the insistent need for the development of more effective therapies with minimal side effects have prompted studies to find alternative new treatments. Among new therapies, photodynamic therapy (PDT) appears as a promising modality in cancer treatment with the lowest rates of side effects. PDT involves two individually non-toxic components that are combined to induce cellular and tissue effects in an oxygen-dependent manner. The first component of PDT is a photosensitizer (PS), a systemically (intravenously) or

topically administered light-sensitive molecule that, after a specific time interval for distribution, localizes more or less specifically to neoplastic tissue (Dolmans, Fukumura et al. 2003). The mechanisms by which the PS selectively accumulates in tumours are complex and not fully understood. It is presumably because of the lack of lymphatic drainage and the high vascular permeability of the agents across a favourable leaky vasculature, as well as their affinity for proliferating endothelium within the tumour stroma. Moreover, the presence of TAMs and the acidic pH of tumour stroma promote the selective uptake of PS by cancer cells (Dougherty, Gomer et al. 1998). The second component of the PDT is light of a specific wavelength, which locally activates the PS. PS activation induces photochemical and photophysical phenomena, marked by the energy transfer to the nearby oxygen, locally generating ROS, as singlet oxygen, hydroxyl radical, and superoxide anions (Portilho, Cavalcanti et al. 2013). More specifically, following the absorption of light (photons), one of the two electrons with opposite spins in the low energy molecular orbital (this is known as singlet state) of the ground state PS is boosted into a high-energy orbital keeping its spin (first excited singlet state). This is a short-lived (nanoseconds) species and can lose its energy by emitting light (fluorescence) or by internal conversion into heat. Alternatively, this excited singlet state PS may also undergo the process known as intersystem crossing whereby the spin of the excited electron inverts to form the relatively long-lived (microseconds) excited triplet-state that has electron spins parallel. The long lifetime of the PS triplet state is explained by the fact that the loss of energy by emission of light (phosphorescence) is a ‘‘spinforbidden’’process as the PS would move directly from a triplet to a singlet state. Additionally, the excited triplet state PS can induce chemical changes in a neighbouring molecule via two main pathways, called type-I and type-II photochemical reaction. Firstly, in a type-I reaction, activated triplet state PS can react directly with other adjacent molecules and transfer a proton or an electron to form a radical anion or radical cation, respectively, which may further react with molecular oxygen or NO^- to produce ROS and RNS, respectively. Alternatively, in a type-II reaction, the triplet PS can transfer its energy directly to molecular oxygen (itself a triplet in the ground state), to form excited state singlet oxygen (Plaetzer, Krammer et al. 2009).

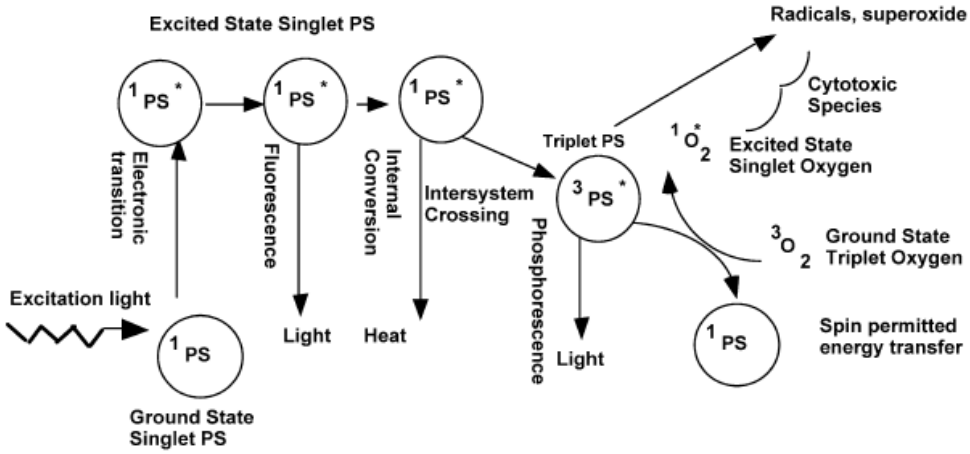

Figure13. Graphical illustration of the photophysical and photochemical mechanisms of PDT

Both type-I and type-II reactions can occur simultaneously, and the ratio between these processes depends on the type of PS used, the concentration of substrate and oxygen (Castano, Demidova et al. 2004). As a result of these photoreactions, cellular organelles and membranes are subjected to a so-called photodamage, whose extent and cytotoxicity depends on several independent factors: the type of PS, its extracellular and intracellular localization, the total dose administered, the total light exposure dose (the total energy of exposed light across a sectional area of irradiated spot, expressed in J/cm^2), the light fluence rate (the radiant energy incident per second across a sectional area of irradiated spot, expressed in W/cm^2), the oxygenation state of the tissue and the time between the administration of the drug and light exposure (Dolmans, Fukumura et al. 2003). However, the anti-cancer effects of PDT are thought to occur at two different levels: direct lethal effects on tumour cells and vascular impairment that limits blood supply to the region (Dougherty, Gomer et al. 1998). The direct PDT effects on tumour cells result in activation of both apoptosis, which may occur via either extrinsic or intrinsic pathway, and necrosis (Castano, Demidova et al. 2005). Crucial determinants for the type of cell death after PDT are cell type, subcellular localization of the PS, and the light dose applied. In general, lower doses are reported to induce apoptosis, while higher doses lead to necrosis (Plaetzer, Kiesslich et al. 2002). Nevertheless, several studies reported the induction of apoptosis after PDT, through the involvement of the death receptor FAS and its ligand FASL and subsequent activation of caspase-8 activation (Ahmad, Gupta et al. 2000; Yokota, Ikeda et al. 2000; Ali, Chee et al. 2002). However, also loss of mitochondrial membrane potential and structural integrity were demonstrated to be involved in apoptosis induction upon PDT via cytochrome c release and caspase-9 activation (Kim, Luo et al. 1999; Grebenova, Kuzelova et al. 2003; Almeida, Manadas et al. 2004). Notably, the targets of PDT also include the microvasculature of the tumour bed, as well as normal microvasculature, and the inflammatory and immune host system. Singlet oxygen causes, infact,

microvascular acute injury and blood vessel blockage in tumour, enhancing apoptosis of tumour cells because of the reduction of blood supply, besides tissue oxygen consumption (Portilho, Cavalcanti et al. 2013). Moreover, since PDT response involves apoptosis induction and microvasculature alteration, it has been suggested that the intrinsic level of tumour NO may be a determinant in the response to PDT, enhancing apoptosis, reducing ischaemia-reperfusion injury and impairing immune response (Reeves, Reed et al. 2009). However the NO role in PDT is still a matter of debate since different studies have shown conflicting results. On one hand, tumours generating low levels of NO are reported to be much more sensitive to PDT than those containing high levels of NO, and the administration of the NOS inhibitor with PDT treatment, enhanced tumour regression (Korbelik, Parkins et al. 2000), while pre-incubation of cells with NO donors or L-arginine decreased cell death induced by photosensitization (Gomes, Almeida et al. 2002). On the other hand, NO positively participates in the events associated with PDT-mediated tumour destruction, particularly in the vascular response. High NO levels may, infact, maintain vessel dilation during PDT treatment, resulting in increased tumour oxygenation, thereby enhancing the oxygen-dependent generation of phototoxic damage, thus promoting tumour regression (Korbelik, Parkins et al. 2000). Moreover, NO participate in modulating antitumour immunity upon PDT treatment (Kawczyk-Krupka, Czuba et al. 2011). PDT may play, infact, a significant role in modulating antitumour immune response, which may be both immunostimulatory and immunosuppressive (Castano, Mroz et al. 2006). Several reports demonstrated that PDT induces the upregulation and extracellular release from necrotic tumour cells of the heat shock protein Hsp70 that, once induced in stress conditions, remains intracellular to chaperone unfolded protein and prevent cell death. Extracellular HSP70 binds to high-affinity receptors expressed on the surface of antigen presenting cells (APC), thus promoting DCs activation and maturation, which allow cross-presentation of antigen cargo of HSP70 by the APCs to $CD8^+$ cytotoxic T cells (Todryk, Melcher et al. 1999).

Additionally, other studies demonstrated that PDT promotes overexpression of HSP family members, such as HSP47and HSP60 (Hanlon, Adams et al. 2001; Verrico, Haylett et al. 2001). Moreover, many reports showed increased serum levels of inflammatory cytokines, such as IL-6, IL1β, IL-10 and IL-8, and local recruitment of neutrophils, mast cell and monocytes after PDT, thus enhancing antitumour immunity (Castano, Mroz et al. 2006). Conversely, PDT was also reported to induce cell death mainly in activated lymphocytes (Jiang, Granville et al. 2002).

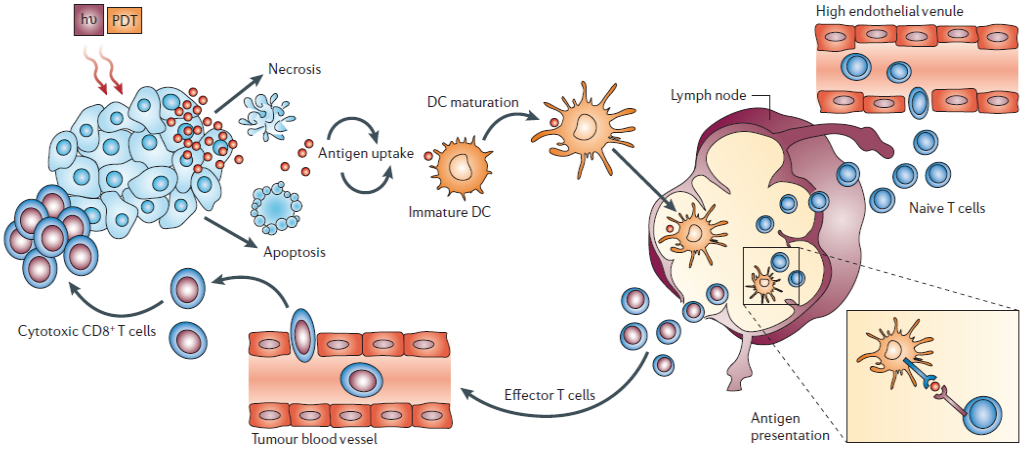

Figure14. Photodynamic therapy induces activation of antigen-specific T cells. When light (hν) is delivered to a photosensitizer (PS)-loaded tumour it induces both apoptotic and necrotic cell death. These cells are phagocytosed by dendritic cells (DCs) that have accumulated owing to the acute inflammatory response triggered by photodynamic therapy (PDT). DCs mature after stimulation by cytokines, which are released at the site of inflammation, and home to the regional lymph nodes where they present antigens to the T lymphocytes. Activated T lymphocytes become effector T cells and, attracted by chemokines, migrate to the tumour and kill the tumour cells (Castano, Mroz et al. 2006).

Notably, PDT induce nuclear translocation of the transcription factor NFκB, thus promoting inflammatory cytokines secretion (Ryter and Gomer 1993). Since its immunomodulating properties, PDT was also tested in combinatorial settings with microbial adjuvant (Korbelik, Sun et al. 2001), exogenous cytokines administration (Golab, Wilczynski et al. 2000) and adoptive cell therapy (ACT) with immature DCs (Jalili, Makowski et al. 2004; Saji, Song et al. 2006), showing very promising results. Notwithstanding, to date PDT is not widely employed, particularly in countries with well-developed infrastructure for cancer care. However, starting from the 1980s, Photofrin®, a hematoporphyrin derivative, has achieved regulatory approval in North and South America, Europe and Asia for treatment of tumours in almost all anatomic sites. Amino levulonic acid (ALA) has been commercially formulated for topical, oral or intravenous introduction for treatment of deeper-seated lesions of the head and neck, lung or esophagus in North and South America, Europe and Asia. Foscan®, a chlorine-based PS, is approved in Europe, South America and Asia for squamous cell cancers of the head and neck that have failed prior therapy. Thanks to the development of novel optic fibers that may be used to drive light to tumours of the cavities, many clinical trials are running for clinical translation of PDT to successful treatment of pulmonary, gastrointestinal and genitouninary tract tumours (Allison 2014).

Aim of the study

Cell death and the bystander effect are crucial for both the efficacy of cancer therapy and the modulation of anti-tumour immune response. Photodynamic therapy (PDT), a form of therapy based on light-sensitive compounds, which are not toxic unless locally photoactivated, provides the opportunity to investigate intercellular communication networks among bystander cells. Although various mediators and pathways have been suggested to mediate cell–cell communication and death signals propagation, to date it is not known which are the key molecules and crucial cellular mechanisms involved for the paucity of studies focusing on the three-dimensional tumour mass. Among the molecules reported to be involved, nitric oxide (NO) and reactive nitrogen species (RNS) appear to be instrumental for cancer therapy success. In fact, NO and RNS act as a double edged sword in cancer biology: depending on the location, amount, and duration of release, in fact, NO can either kill or sustain proliferation of tumour cells. So far, few methods such as chemiluminescence and spectroscopy have been applied for NO tracking, however they suffer from low spatial resolution and, in some cases, require complicated instrumentation.

Therefore, the primary aim of this study was to investigate and characterize the cell signals responsible for bystander effect occurring upon PDT within the intact tumour microenvironment, paying particular attention to NO. To this purpose a focal PDT approach focused on one single cell was exploited on tumour-bearing mice in which dorsal skinfold window chambers were surgically implanted. Intravital microscopy on tumour-bearing mice allows to image clearly individual cells, including tumour, stromal and immune cells, disclosing in real time the dynamics of cell communication after PDT. Instrumental for the study was the setting of a valuable tool to dynamically monitor in real-time intracellular NO by fluorescence microscopy on live animals and cell cultures. Since nitric oxide synthase (NOS) enzymes activity may be modulated by intracellular calcium concentration depending on the specific NOS isoform involved, to characterize deeper the molecular mechanisms triggered by PDT intracellular calcium level variations were also investigated. Moreover, the involvement of gap junctions and connexins in PDT bystander effect was evaluated.

Materials and methods

Animals and surgical procedures for intravital microscopy

Adult male BALB/c (27-30 grams) mice were purchased from Charles River Laboratories (Calco, Italy). All mice were maintained under specific pathogen-free conditions in the animal facilities of the Venetian Institute of Molecular Medicine, and experiments were performed according to state guidelines and approved by the local ethics committee. Dorsal skinfold window chambers (DSWC) were surgically implanted into the backs of mice as follows and entire implantation procedure was conducted within a laminar flow hood to preserve a sterile field. Mice were anesthetized with Ketamine/Xylazine i.p. at a dose of 80mg/kg Ketamine and 5mg/kg Xylazine and maintained at 38° C on a steel heating plate. Both chamber pieces containing a round window were placed on the mouse dorsal skin, tightened together by the appropriate screws and finally sutured to the skin by non-absorbable monofilament sutures. An area of 10 mm diameter circle of cutaneous tissue was carefully cut away from the skin fold inside the DSWC window, exposing the blood vessels of the subcutaneous tissue adjacent to the striated muscles of the opposing skin fold by ophthalmic scissors. Then, a 12-mm round glass coverslip was placed in the chamber to cover the exposed tissue and secured with a snap C-ring. A more detailed procedure can be found in (Huang, Shan et al. 1999; Roberts and Lin 2004). After surgery mice were treated twice a day for 3 days with Tramadol i.m. at a dose of 10mg/kg/die and finally tumour cells were dropped within the chamber. Therefore, the C-ring and glass cover slip was temporarily removed from the chamber and the single cell suspension was injected s.c. into the opposing fold of skin. Mice were checked daily for general health as well as for vessel formation/tumour progression and chamber-skin interaction. At day 5-7 of tumour growth, the tumour-bearing mouse was anesthetized with ketamine/xylazine (80mg/kg and 5mg/kg) and prepared for PDT treatment and intravital microscopy.

Cell culture and tumour injection

C26GM mouse colon carcinoma cell line was derived from C26 colon carcinoma (H-2^d) genetically modified to release GM-CSF. Briefly, GM-CSF cDNA obtained by RT-PCR from ConA-stimulated murine blasts was cloned into the LXSN retroviral vector, and used to infect C26 cells, as previously described (Bronte, Serafini et al. 2003). C26GM cells were grown in DMEM (Invitrogen), supplemented with 2mM L-glutamine, 10mM HEPES, 50µM 2-Mercaptoethanol, 150U/mL streptomycin, 200 U/mL penicillin, and 10% heat-inactivated FBS (Gibco). For tumour challenge, 0.5 x 10^6 C26GM cells were labeled with 5µM

Carboxyfluorescein diacetate succinimidyl ester (CFDA-SE, Molecular Probes) and injected in a total volume of 20µl s.c. into the DSWC. For *in vitro* studies, 1.5-2.0 x 10^5 C26GM were plated on 12-mm round glass coverslips into 24-well culture plates.

In vivo photodynamic therapy and intravital microscopy

Aluminum phthalocyanine chloride (AlPC) (Sigma) was dissolved in dimethyl sulfoxide (Sigma) at 10mM and kept in the dark. Five days after tumour cell challenge, mice were anesthetized with Ketamine/Xylazine i.p. at a dose of 80mg/kg Ketamine and 5mg/kg Xylazine and maintained at 38°C on a steel heating plate under an upright microscope with the window opening facing the objective lens. Then mice received an intratumoural microinjection of 20µM AlPC diluted in DMEM, by a glass micropipette and after one hour of incubation, subjected to focal PDT. For focal photosensitization, the output of a 671 solid state laser was injected into a permissive fibre optic cable (62.5µm core, Thorlabs), whose output was projected onto the specimen plane by an aspheric condenser lens (20mm effective focal length, Thorlabs) and the re−collimated beam was directed onto a dichromatic mirror (650 shortpass, Chroma) placed at 45° just above the objective lens of the microscope. By carefully adjusting the position of the fiber in front of the aspheric lens we projected a sharp image of the illuminated fiber core (spot) onto the specimen focal plane selected by the (infinity corrected) objective lens. For focal PDT treatment, an irradiation time of 60 sec was used to deliver 0.06mW/µm^2 of light (Power = 5 mW centered on a circular area of 80µm^2) from a 671 nm solid state laser, using a 40x water immersion objective (NA1.15, UApoN340, Olympus) connected to a microscope (BX51, Olympus) equipped with a spinning disk unit (DSU, Olympus). For intravital microscopy, tumour mass was incubated with AlPC 20µM and co-loaded for 60 min with Fura-2 AM 30µM (Molecular Probes) by micro-injection with a glass micropipette. The incubation medium contained also pluronic F–127 (0.01% w/v), and sulphinpyrazone (250µM) to prevent dye sequestration and secretion. AlPC-Fura-2 loaded tumour was alternately illuminated by light from a 365 nm and 385 nm LEDs, directed onto the sample through a DM480HQ dichromatic mirror (Chroma) and fluorescence emission was selected at around 510 nm using an interference filter (BA495-540HQ, Chroma). Images were recorded on a sCMOS camera (PCO.Edge) at a rate of 1 couple of frame per second, with 200ms exposure time/frame. Signals were measured as dye emission ratio changes, $\Delta R = R(_t) - R(_0)$, where t is time and $R(_t)$ is emission intensity excited at 360 nm divided by the intensity excited at 380 nm, and $R(_0)$ indicates pre−stimulus ratio. For NO detection, after one hour AlPC incubation, tumour was loaded with the fluorescent probe selective for NO, 2-{4,5-Bis[(6-(2-ethoxy-2-oxoethoxy)-2-methylquinolin-8-ylamino)methyl]-6-hydoxy-3-oxo-3H-xanthen-9-yl}benzoic acid FL (CuFL) (Lim, Xu et al. 2006) at the final concentration of

40μM (Strem Chemicals) and AlPC-CuFL loaded cells were excited by light from a collimated 470 nm LED (M470L2–C1, Thorlabs) for 200 ms. Signals were measured as relative changes of fluorescence emission intensity ($\Delta F/F_0$), where F_0 is prestimulus fluorescence, F is fluorescence at post–stimulus time *t* and $\Delta F = F – F_0$.

In vitro PDT, ratiometric calcium imaging and NO imaging

C26GM cell cultures were incubated with AlPC 10 μM and co-loaded with Fura-2 AM 15 μM (Molecular Probes) for 60 min at 37° in DMEM containing pluronic F–127 (0.01%, w/v), and sulphinpyrazone (250 μM). For NO detection, after one hour of AlPC and Fura-2 incubation, cells were loaded with CuFL 20 μM for 20 min at room temperature. C26GM cells were then transferred to the stage of an upright wide–field fluorescence microscope and continually superfused with an extracellular medium containing NaCl 150mM, KCl 5mM, $MgCl_2$ 1mM, Sodium Pyruvate 2mM, Hepes−NaOH 10mM, D−glucose 5mM (pH 7.2, 310 mOsm). When present, $CaCl_2$ was added at the final concentration of 1mM. AlPC-Fura-2-CuFL co-loaded C26GM cells were alternately illuminated by light from a 365 nm and 385 nm LEDs for Fura-2 and 470 nm LED for CuFL. The same objective, filter settings and PDT parameter of *in vivo* PDT approach were used for *in vitro* experiments. Images were recorded at a rate of 1 couple of frame/second for Fura-2 and 1frame/second for CuFL, (camera exposure time 50ms/frame). Experiments with EGTA (adjusted to pH 7.3 with NaOH), U73122 and Flufenamic Acid (FFA)(Sigma-Aldrich) were performed by adding the reagents in extracellular medium bath at room temperature. For NOS inhibition, L- NAME (Tocris) was diluted in culture medium, incubated overnight and cells were maintained in solution supplemented with the inhibitor for all steps of the experiments.

Real-time live cell imaging of apoptosis

AlPC incubated C26GM were loaded only with Fura 2 for focal PDT treatment, as previously described. After photosensitization, ,pSIVA-IANBD and Propidium Iodide (Imgenex) were added directly to the extracellular medium enriched with $CaCl_2$ to the final concentration of 2.5 mM.. Cells were imaged by time lapse microscopy of the same field of view. pSIVA-IANBD fluorescence was excited by light from a collimated 470 nm LED (M470L2, Thorlabs), through a DM480HQ dichromatic mirror (Chroma) and fluorescence emission was selected at around 510 nm using an interference filter (BA495-540HQ, Chroma), whilst Propidium Iodide was illuminated by a 535 nm LED, through a DM560 dichromatic mirror (Chroma), and fluorescence emission was collected by a 590LPV2 emission filter.

Focal photostimulation with caged IP3

For focal photostimulation with caged IP3, the output of a Transistor–Transistor Logic-controlled laser diode (10 mW, 375 nm; Power Technology,) was injected into a UV permissive fibre optic cable (multimode step index 0.22 N.A., 105 µm core, Thorlabs). Fibre output was projected onto the specimen plane by an aspheric condenser lens (20 mm effective focal length, Thorlabs) and the re−collimated beam was directed onto a dichromatic mirror (400 dclp, Chroma) placed at 45° just above the objective lens of the microscope. C26GM cells were loaded with 5µM caged IP3 AM, 10-µM Fura Red-AM, pluronic F–127 (0.01% w/v), and sulphinpyrazone (250µM) and incubated for 60 min at 37°. Then, cells were loaded with CuFL 20µM for 20 min at room temperature. Fura Red-AM and CuFL fluorescence was excited by a 470 LED, through a dichromatic mirror (400 dclp, Chroma) and detected using a dichroic beam splitter 585 DCXR (Chroma) and an emission filter 660/50 nm and 535/30 nm, respectively. Cultures were observed with a 60x water immersion objective (N.A. 1.0, Fluor; Nikon), and emission was monitored with a sCMOS camera (PCO.Edge).

qRT-PCR

mRNA was extracted from C26GM cultured cells using RNAeasy kit (Qiagen). cDNA was obtained by reverse transcription of mRNA with random hexamers and ThermoScript RT-PCR system (Life technologies) according manufacturer instruction. qPCR was performed on cDNA to amplify Cx26, Cx30, Cx30.3, Cx40, Cx43, NOS1, NOS2 and NOS3 and was normalized to GAPDH expression. Amplification was carried out using SYBER Green (Applied Biosystems) on the ABI 7700 sequence detection system equipped with ABI Prism 7700 SDS software (Applied Biosystems) through the following amplification cycles:
50°C: 2 min
95°C: 10 min
95°C: 15sec , 60°C: 1 min (40 cycles)
For Real-Time PCR the following primers were used:
Cx26f: 5'−CGG AAG TTC ATG AAG GGA GAG AT −3'
Cx26r: 5'−GGT CTT TTG GAC TTT CCT GAG CA −3'
Cx30f: 5'− GTC ATC GGT GGC GTG AAC AAG CAC −3'
Cx30r: 5'− GAG CAG CAT GCA AAT CAC GGA TGC −3'
Cx30.3f: 5'− TCA AAC ATG GGC CCA ATG −3'
Cx30.3r: 5'− GGG AGT CAC AGA GCA AGC −3'
Cx40f: 5'− CTG TCC CCA CCC AGT CAA CT −3'
Cx40r: 5'− CCG TTT GTC ACT ATG GTA GC −3'
Cx43f: 5'− TAC CAC GCC ACC ACC GGC CCA −3'
Cx43r: 5'− GGC ATTTTGGCTGTCGTCAGGGAA −3'
NOS1f: 5'−TCA AAG CCA TCC AGC GCA TA −3'
NOS1r: 5'− TGG TAC CGG TTG TCA TCC CT −3'
NOS2f: 5'− GAC ATT ACG ACC CCT CCC AC −3'

NOS2r: 5'− ACT CTG AGG GCT GAC ACA AG −3'
NOS3f: 5'− GGG AAA GCT GCA GGT ATT TG −3'
NOS3r: 5'− CTG TGA TGG CTG AAC GAA GA −3'
GAPDHf: 5'−ATG TGT CCG TCG TGG ATC TGA C−3'
GAPDHr: 5'−AGA CAA CCT GGT CCT CAG TGT AG−3'
Connexin and NOS mRNA expression relative to GAPDH was performed using the ΔΔCT method .

Electrophysiology and fluorescence imaging

Vf2.1.Cl (Miller, Lin et al. 2012) was provided by Roger Y. Tsien (University of California, San Diego). For voltage imaging, C26GM cell cultures were incubated for 15 min at 37°C in extracellular medium (see above) supplemented with Vf2.1.Cl (200nM) and pluronic F–127 (0.1% w/v), thereafter cultures were continually superfused with extracellular medium. Vf2.1.Cl fluorescence was excited by light from a 470 nm LED (M470L2, Thorlabs) passing through a BP460–480 filter (Olympus) and directed onto the sample through a 515 dcxr dichromatic mirror (Chroma) while Vf2.1.Cl fluorescence emission was selected by an ET535/30M filter (Chroma). All fluorescence images were formed by a 60x water immersion objective (NA 1.0, Fluor, Nikon) and projected on a sCMOS camera (PCO.Edge) controlled by software developed in the laboratory. Image sequences of Vf2.1.Cl fluorescence were acquired continuously at 10 frames per second with 100 ms exposure time. To synchronize image acquisition and electrical recordings, we sampled the 5 V pulse (FVAL) that signals active exposure of the CCD camera Vf2.1.Cl signals were measured as relative changes of fluorescence emission intensity ($\Delta F/F_0$), where F_0 is prestimulus fluorescence, F is fluorescence at time t and $\Delta F = F - F_0$ (Ceriani and Mammano 2013)

Immunofluorescence and confocal microscopy

C26GM cells, treated or not with AlPC, were fixed in 4% paraformaldehyde for 20 min at room temperature, rinsed in phosphate buffered saline (PBS), and permeabilized with 0.1% Triton X–100, dissolved in bovine serum albumin (BSA) 1% solution and incubated with anti NOS (1:200, Santa Cruz), anti NOS2 (1:200, Abcam), anti NOS3 (1:200, BD transduction laboratories), anti Cytochrome C (1:200, BD Pharmingen). The appropriate AlexaFluor488-conjugated secondary antibodies were used. Nuclei were counterstained with 1 μg/ml Hoechst 33258 and mounted with ProLong (Invitrogen). Images were acquired using a confocal microscope (TCS SP5, Leica) equipped with an oil–immersion objective (63x HCX PL APO 1.25 N.A., Leica). Laser line intensities and detector gains were carefully adjusted to minimize signal bleed through outside the designated spectral windows.

Data analysis and statistics

Images, acquired using software developed by Prof. Mammano's group, were analyzed based on Matlab platform (Release 14, MathWorks, Inc., Natick, MA, USA). Specific regions of interest (ROIs), corresponding to different cells located at different distance from the PDT-targeted cell, were drawn in order to measure, the amplitude, the rate of increase and area under the curve of the fluorescence traces of Fura-2 and CuFl signals per single cell. Specifically, amplitude was measured as maximal fluorescence variation in response to a specific stimulus,, whereas the rate of increase was estimated as the slope of the line tangent to each fluorescence trace in the linear range of amplitude response. Statistical comparisons of means for paired samples were made by one-way ANOVA test. p–values are indicated by letter p and $p< 0.05$ was selected as the criterion for statistical significance. The wave invaded area was computed as the field of view fraction where fluorescence levels exceeded an arbitrary threshold, corresponding to a 10% increase over the pre-stimulus values for both ratiometric Fura-2, and CuFL fluorescence changes. The rate of wave propagation was calculated as the slope of the line tangent to each wave invaded area curve in the linear range of increase. Statistical comparison between rate of wave propagation was performed by using Student's t test. In figures, asterisks were used as follows: * $p\leq0.05$; ** $p\leq0.01$; *** $p\leq0.001$. Pseudocolor images were generated using the hue-saturation-value (HSV) visualization algorithm: hue was used to represent fluorescence changes; value (brightness) carried pixel intensity from a reference image that was either updated on a frame-by-frame basis or obtained as an average over a specified number of frames; saturation was set to 1.0. Frames so constructed were converted to ordinary RGB images by a single call to the Matlab library function hsv2rgb, and displayed.

Results

Focal PDT triggers NO and Ca^{2+} release within tumour microenvironment

Radiation-induced bystander effects have become established in the radiobiology vocabulary as a *bona fide* radiation response, however key messengers and signalling pathways are only partially characterized. This lack of information reflects the paucity of studies focusing on the three-dimensional tumour mass. Several reports suggest the involvement of NO and RNS in bystander effects, even if no direct evidence of NO release after PDT has been published. Chemiluminescence and spectroscopy have been used for NO tracking, however these methods suffer from low spatial and temporal resolution and, in some cases, require complicated instrumentation.

Small molecule–based fluorescent probes for NO, including o-diaminonaphthalene (DAN), o-diaminofluoresceins (DAFs) and o-diaminocyanines (DACs), are now commercially available, but their changes in fluorescence require reactions with oxidized NO products rather than NO itself, thus, their fluorescence-response does not necessarily reflect real-time NO production. For these reasons, we based our studies on CuFL, a Cu(II) fluorescein-based compound which reacts rapidly, is substantially more selective for NO compared to other potentially interfering molecules and can be utilized to visualize NO production in living cells by fluorescence imaging (Lim, Xu et al. 2006).

To single out the key mediators of bystander effects and to define the role of NO, dorsal skinfold window chambers (DSCW) were surgically implanted on BALB/c mice. Few days after recovery from surgery, 0.5×10^6 C26GM colon carcinoma cells were injected into the DSCW. Owing to its GM-CSF secretion and aggressiveness (animals are killed by the tumour in less than 2 weeks), the C26GM colon carcinoma cell line is suitable for intravital microscopy on DSCW-bearing mice, where it induces immune cell accumulation at tumour site. Five days after tumour challenge, the implanted tumour was co-loaded with the PS aluminum phtahlocyanine chloride (AlPC) and fluorescent indicators (CuFl, Fura-2) by intra-tumour microinjection with a glass micropipettes (see Methods). Mice were transferred on the stage of an up-right spinning disk confocal microscope and AlPC was activated in a single cell of the tumour mass by focussing 670 nm laser light into an $80\mu m^2$ area (see Methods). We refer to this type of stimulation as *focal PDT*. NO produced by cells within the tumour was monitored by intravital microscopy of CuFl fluoresence emission, which raises rapidly when NO levels increase and binds irreversibly to this probe (Lim, Xu et al. 2006). As shown in **Figure1**, focal PDT ensued in CuFl increase not only in the irradiated but also in a vast population of sorrounding (and, by definition, bystander) cells within the tumour microenvironment.

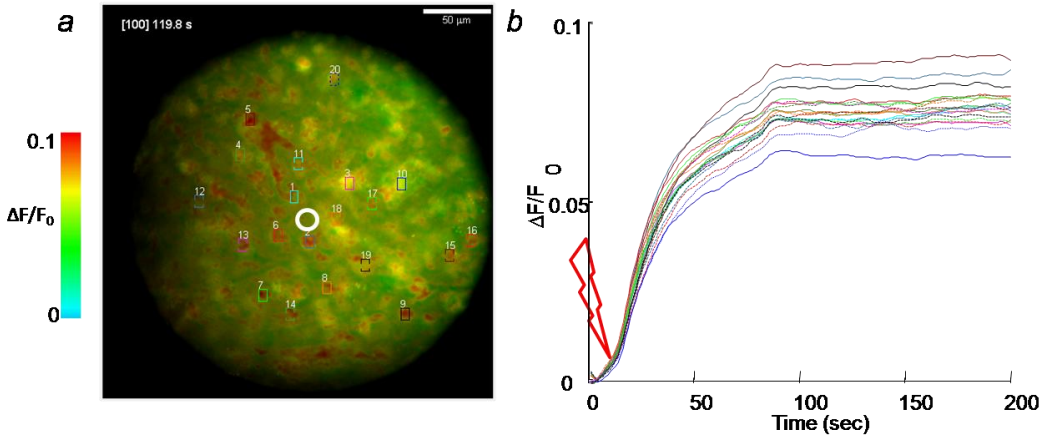

Figure1. Focal PDT induces NO release within the tumour microenvironment.
a. Representative false-color image showing CuFL fluorescence changes ($\Delta F/F_0$), encoded as shown by the color scale bar, obtained as maximal projection rendering of all frames recorded in C26GM tumour, transplanted into the DSWC and imaged for 4 min at one frame per second. After 10 s of baseline recording, the PS was activated by a 60 s light step from a 670 nm laser focused on the white circled cell. (Scale bar, 50 µm.). *b.* NO fluorecence traces obtained by averaging signals within 20 regions of interest (ROIs) corresponding to individual bystander cells at different distance from the irradiated one.

Since NOS activation may depend on intracellular Ca^{2+} concentration, which is known to modulate a plethora of cellular processes, we took advantage of the ratiometric Ca^{2+} indicator Fura-2 to measure intracellular Ca^{2+} level variations. Following focal PDT, we observed a rapid increase in intracellular Ca^{2+} concentration (max ΔR = 40%). Also this type of signal was detected both in the irradiated and in bystander cells (**Figure2**). These data provide direct evidence that focal PDT induces NO production from irradiated as well as non-irradiated cells, which may release ions, cytokines and other second messengers establishing a signalling intercellular network responsible for bystander effects within the tissue. Our Fura-2 data suggest that Ca^{2+} signalling may play an important role in these processes.

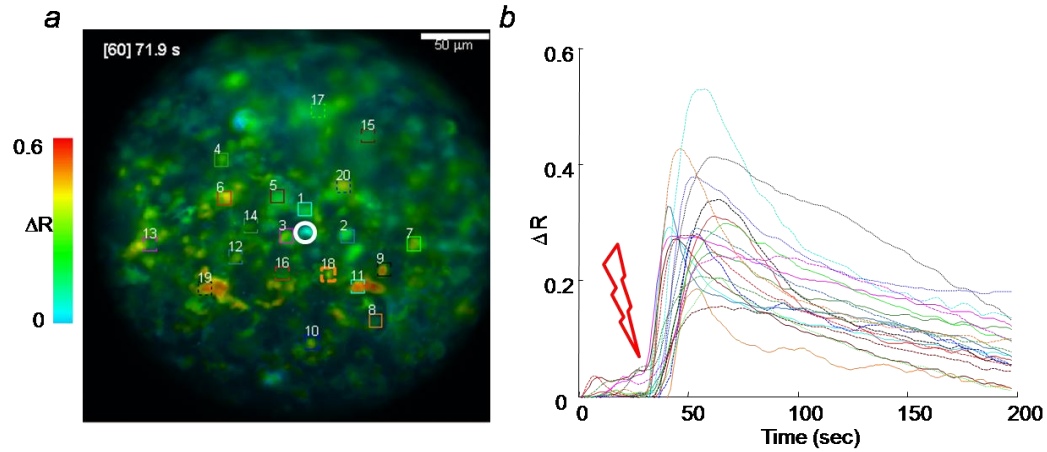

Figure2. Focal PDT induces intracellular Ca^{2+} transients within the tumour mass.
a. Representative false-color image of Fura-2 fluorescence ratio changes (ΔR), encoded as shown by the color scale bar, obtained as maximal projection rendering of all frames recorded in C26GM tumour, transplanted into the DSWC. Images were acquired for 4 min at 2 frame per second. After 30 s of baseline recording, the PS was activated by a 60 s light step from a 670 nm laser focused on the white circled cell. (Scale bar, 50 µm) *b.* Sample traces of Ca^{2+} responses obtained by averaging Fura-2 ratio signals within 20 randomly selected ROIs corresponding to individual bystander cells at different distance from the irradiated one.

Bystander effects produced by focal PDT are sensitive to stimulus duration

The analysis of bystander effects within the whole tumour mass is complicated by the presence of different cell populations and the difficulty of performing intravital microscopy experiments. In particular, Fura-2 excitation requires short wavelengths (360nm and 380nm light sources), which do not penetrate deep into the tissues. To circumvent these problems, we performed the same experiments on C26GM cancer cell monolayers grown on glass coverslips and co-loaded with Fura-2 and CuFL. We used a 3-wavelength sequential excitation protocol (360 nm, 380 nm, 470 nm) to record both Ca^{2+} and NO signals from the same cell population and we analyzed signal correlation under these simplified *in vitro* conditions (**Figure3 a, b, c**). Analysis of Fura-2 fluorescence traces shows that focal PDT induced a rapid raise of intracellular Ca^{2+} levels in the irradiated cell which propagated to all the cells in the field of view within 10 seconds. Of notice, this radial intercellular Ca^{2+} wave was followed by a slower wave of NO release that progressed from the irradiated cell to the bystander population. To quantify these phenomena, the wave invaded area was computed as the field of view fraction where fluorescence levels exceeded an arbitrary threshold (corresponding to a 10% increase over the pre-stimulus values). We measured this area for different values (15, 30 and 60 s) of the time interval during which the targeted cell was exposed to light from the 670 nm laser light (light step). Focal PDT evoked a Ca^{2+} wave that invaded the whole field of view (corresponding to an area of 60×10^3 µm^2) for each one of these light steps (**Figure3 a, b, c**). As for NO, both the rate of area invasion and its extent varied with light step duration

(**Figure3 d, e, f)**. Specifically, NO signals evoked by a 15 s light step invaded only 50% of bystander cells. With a 30 s step, the intercellular NO wave required 20 seconds to reach 50% of its maximal invaded area (90%). Finally, a 60 s light step promoted a faster NO wave that invaded 50% of the cells within 12 s and thereafter propagated to all cells within the analyzed area (**Figure3 g, h, i**).

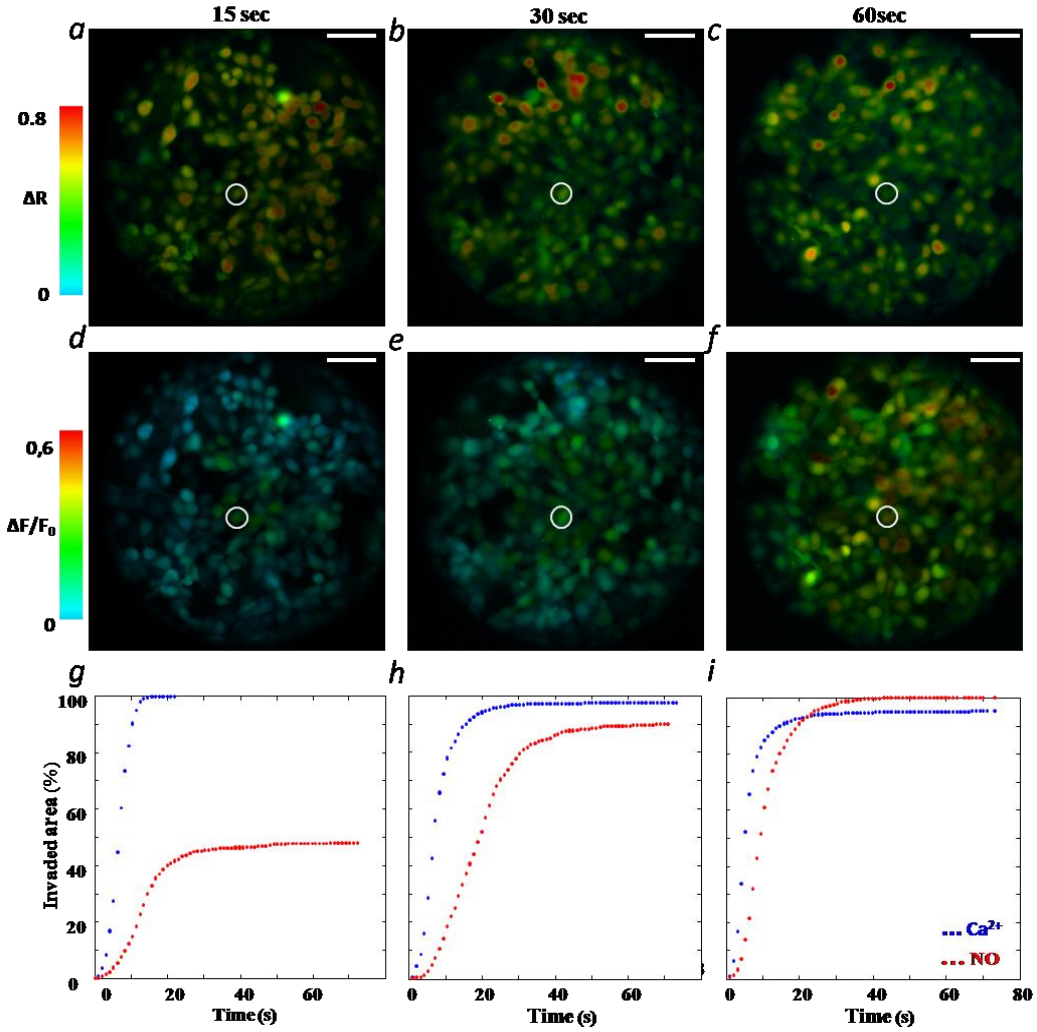

Figure3. Focal PDT duration modulates the extent of bystander effects.
a-c Representative false–color images of Fura-2 fluorescence ratio variations obtained as maximal projection rendering of all frames recorded in C26GM cells; laser light was focused on the white circled cell for 15 s *(a)*, 30 s *(b)* and 60 s (*c*). *d-f* Maximal projection rendering of CuFL fluorescence variation during focal PDT for light steps of 15 s *(d)*, 30 s *(e)* and 60 s (*f*); scale bar, 50 µm. *g-i* The percentage of field of view invaded by Ca^{2+} (blue dots) and NO (red dots) intercellular waves is shown as function of time for light steps of 15 s *(g)*, 30 s *(h)* and 60 s (*i*).

NO production is strictly dependent on the distance of bystander cells from the irradiated cell

To maximize the number of NO-producing bystender cells within the field of view, for the rest of these experiments we used only 60 s light steps. We spatially averaged Fura-2 and CuFl fluorescence signals from regions of interest (ROIs) corresponding to individual cells generating families of time-dependent fluorescence traces. We then quantified both amplitude and rate of increase of Ca^{2+} and NO signals in response to focal PDT . Amplitude was measured as maximal fluorescence variation, whereas the rate of increase was estimated as the slope of the line tangent to each fluorescence trace in the linear range of amplitude response. We also quantified the the area under the trace, which depends on both the signal amplitude and the duration of the intracellular signal variation. Data analysis shows that intracellular Ca^{2+} concentration increased rapidly in bystander cells (**Figure4 a)** whereas NO production followed a slower time course (**Figure4 b**). For statistical comparison, we divided the field of view (total area 60×10^3 μm^2) into three concentric regions centred on the irradiated cell (**Figure S1**). The first region, r_1, was a circle with a radius of 35µm; the second region, r_2, was an annulus with an inner radius of 35µm and outer radius of 75µm; the third region, r_3, was a larger annulus with inner radius of 75µm and outer radius of 120µm. In each region, we selected a number of cells proportional to the analyzed area (5, 18 and 35 cells respectively within r_1, r_2 and r_3). We then pooled and analyzed data from three independent experiments. Amplitudes of Ca^{2+} signals as well as the area under the trace increased at increasing distance from the irradiated cell, whereas the temporal rate of signal increase displayed an opposite trend (**Figure4 c**). In the case of NO, all three parameters decreased at increasing distance from the irradiated cell (**Figure4 d**). These data support the notion that bystander cells actively participate in the spreading of the PDT response, as intracellular Ca^{2+} concentration and NO production may be detected also at distant site from the targeted cell. The mechanism underpinning this crosstalk, however required further investigations.

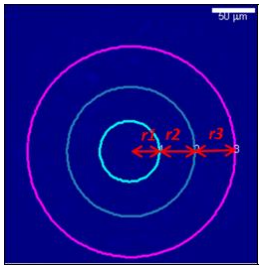

Figure S1. Scheme depicting the analyzed areas *r1, r2, r3.*

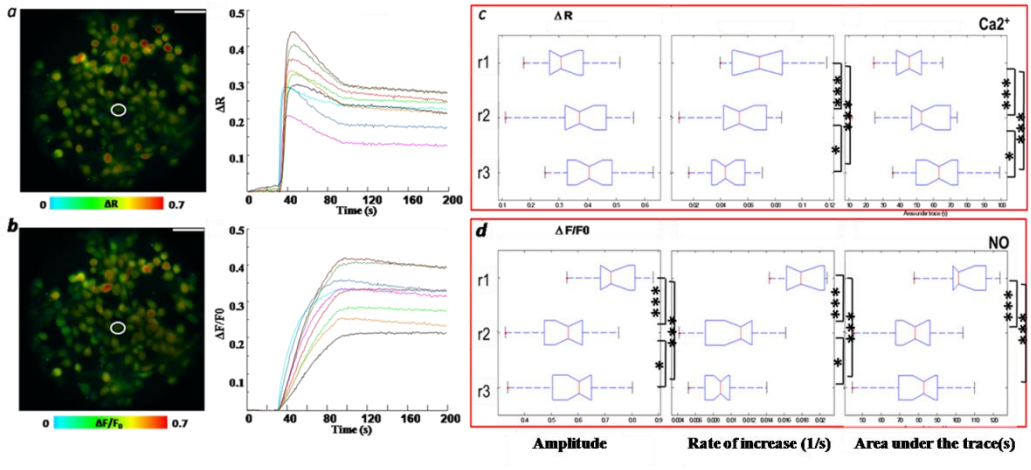

Figure4. NO release is strictly dependent on the distance from the targeted cell. Representative false–color images and sample traces of Fura-2 (*a*) and CuFL (*b*) fluorescence variations induced by 60 second-focal PDT, (30 sec baseline recording). Box plots showing distribution of amplitude, rate of increase and area under the trace of Ca^{2+} (*c*) and NO (*d*) signals in cells located within the areas *r1*,*r2* and *r3*. Data in (*c*) and (*d*) were pooled from three independent experiments. Asterisks indicate significant differences between data distributions *, $p \leq 0.05$; **, $p \leq 0.01$; ***, $p \leq 0.001$ (Anova test).

NO signals evoked by PDT are likely due to constituive NOS

The correlation between intracellular Ca^{2+} transient and NO production evoked by PDT raised the hypothesis that NO might be the product of NOS enzymes. Only constitutive NOS1 and NOS3 activity is considered calmodulin/Ca^{2+} dependent. However several reports demonstrated NOS2 positivity in human tumour samples, including colon cancers. Therefore we performed mRNA analysis to identify the NOS isoforms expressed by the C26GM cell line. We detected low absolute mRNA levels of all three isoforms (particularly low in the case of NOS2) and the highest signal corresponded to NOS3 (**Figure5 a**). To corroborate these findings, NOS expression was tested at the protein level by confocal immunofluorescence imaging using an antibody that cross-reacts with all three isoforms (**Figure5 b)**. Using specific antibodies for NOS2 and NOS3, we verified that the NOS3 signal, albeit weak, is clearly detectable (**Figure5 c, d)**.

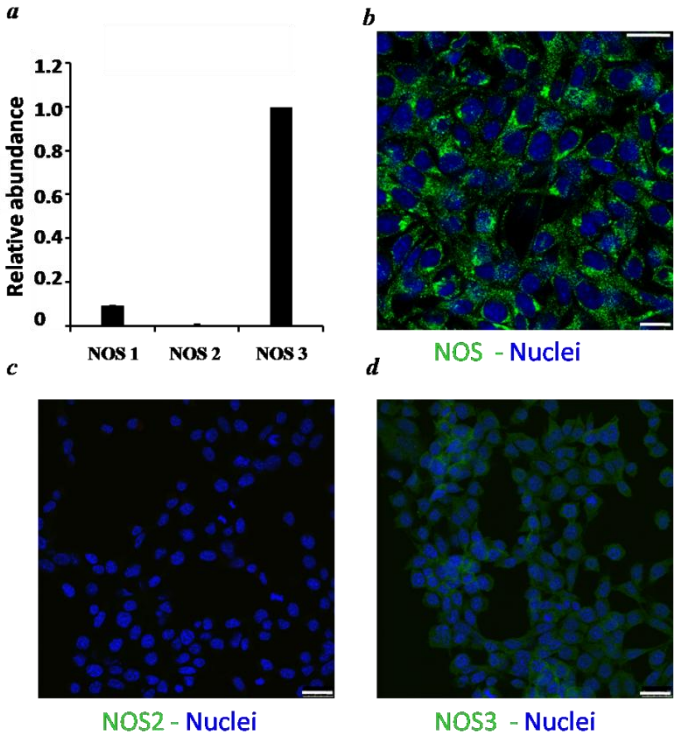

Figure5. C26GM cells show low levels of NOS. *a*. Total RNA was isolated from C26GM and qRT-PCR for NOS1, NOS2 and NOS3 content was performed. Data, reported as relative abundance, are normalized to NOS3. GAPDH was used as internal control. .Confocal images of C26GM colon carcinoma cells immunostained for total NOS protein *(b)*, NOS2 (*c)* and NOS3 (*d)* (green fluorescence). Nuclei were counterstained with Hoechst (blue). (Scale bar, 25 µm)

We further tested NOS involvement in PDT bystander responses using the cell-permeable NOS inhibitor L-N^{ω}-nitro-L-arginine methyl ester (L-NAME), a more soluble analogue of L-arginine. After overnight incubation with 1µM L-NAME, focal PDT was performed as described above. This inhibitor significantly reduced bystander NO release, which showed lower amplitudes and slower rate of signal increases (**Figure6 a-h**). In the presence of L-NAME, the NO wave was delayed with respect to the control, whereas the Ca^{2+} wave was nearly unaffected (**Figure6 i**). However Ca^{2+} signal amplitude and rate of signal increase were reduced by treatment with L-NAME (**Figure6 e, g**), suggesting that a positive feedback mechanism links NO production to the increase of intracelluar Ca^{2+} levels promoted by PDT. In central neurons, NO has been recently demonstrated to directly activate ryanodine receptors (RyRs), which mediate Ca^{2+} release from intracellular stores (Kakizawa, Yamazawa et al. 2012). Our results therefore suggest that NO increase following PDT in tumour cells may trigger a Nitric Oxide Induced Calcium release (NICR) mechanism similar to that involved in NO-induced neuronal cell death (Kakizawa, Yamazawa et al. 2012).

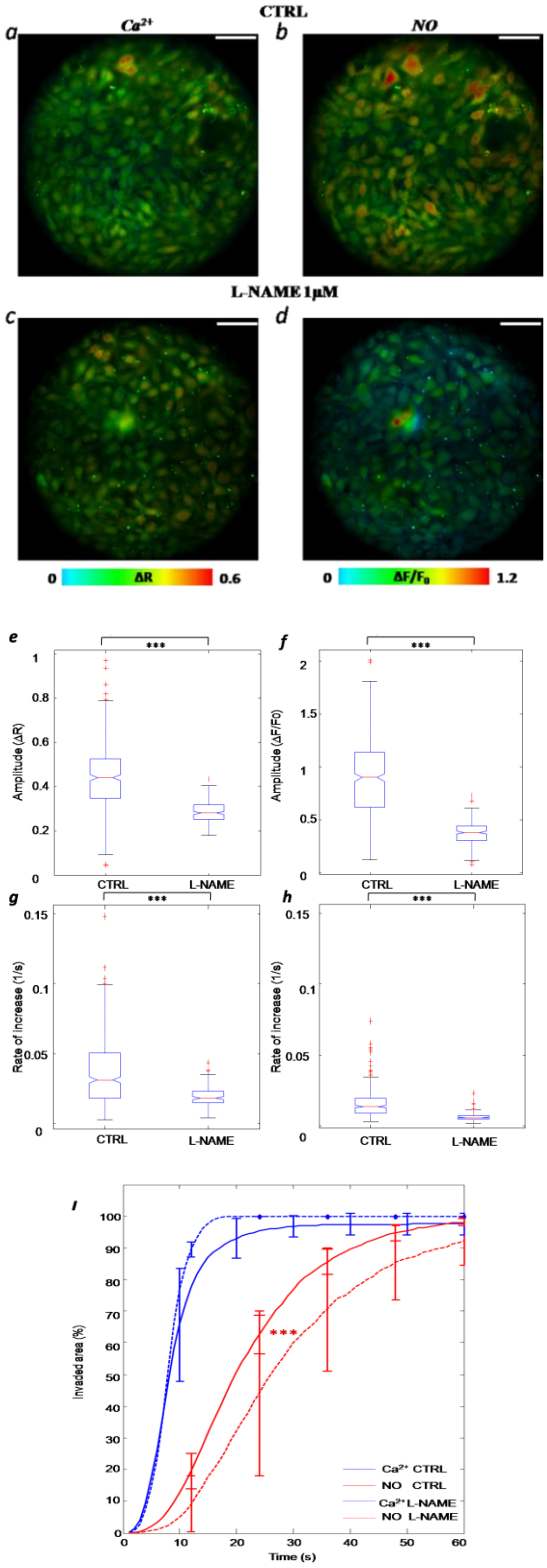

Figure6. PDT triggers NOS activation. Representative false–color images of Fura-2 and CuFL fluorescence variations, encoded as shown by the color scale bars, induced by focal PDT in either control (*a, b*) or L-NAME-treated (*c, d*) C26GM cells (scale bar, 50 µm). Ca^{2+} and NO signal amplitude (*e, f*) and rate of increase (*g, h*) in control or L-NAME-treated C26GM cells . Data were pooled from three independent experiments. Asterisks indicate significant differences between data distributions (*** $p \leq 0.001$, Anova test). *i.* Area invaded by Ca^{2+} and NO waves vs. time (mean ± s.d.) for C26GM cells incubated or not with L-NAME. Red asterisks indicate significant differences between the rates of NO wave propagation in control or L-NAME treated cells. (*** $p \leq 0.001$, Student's *t* test).

PDT-induced bystander effects trigger apoptosis via cytochrome c release

Both Ca^{2+} and NO are reported to be involved in the induction of apoptosis. Indeed, the loss of Ca^{2+} homeostasis may lead to cell injury as well as high levels of NO/RNS which, through modifications of death-related target proteins, mediate inhibition of cellular respiration, thus affecting mitochondrial membrane permeability, finally leading to cytochrome c release and initiation of apoptosis (Leon, Jeannin et al. 2008). PDT has been indeed demonstrated to trigger both apoptosis and necrosis. (Castano, Demidova et al. 2005). Thus, we performed focal PDT with AlPC and we evaluated the expression of specific apoptotic markers. In particular, we used pSIVA, an annexin-based, polarity sensitive probe for the spatiotemporal or kinetic analysis of apoptosis (Kim, Chen et al. 2010). In these experiments, we monitored only Ca^{2+} (with Fura-2) and not NO due to the overlap between CuFL and Psiva fluorescence emission spectra. After focal PDT, we added pSIVA and propidium iodide (PI) to the extracellular medium. Fluorescence images were acquired every 30 min (1 frame for pSIVA and 1 frame for PI). The irradiated cell displayed a clearly detectable pSIVA signal afters 30 min (data non shown). Within 1 hour following PDT, both pSIVA and PI signals were detected in the irradiated cell and its nearest neighbours; thereafter the signals propagated to more remotely located bystander cells (**Figure7**). By 4 hours about 40% of cells has at least entered apoptotic cell death. No toxic effects were observed in control experiment, in which the PS AlPC was loaded but not photoactivated. These data demonstrate that unless photostimulated, the PS is not able to trigger any Ca^{2+} wave (**Figure7**). As internal positive control of the staining, control cells were treated with staurosporine, a well known apoptosis inducer (20 µM, 2 hour incubation) after 4 hours of recording (**Figure7 e**). Altogether, these results support the notion that PDT promotes bystander cell death and suggest that these effects may contribute significantly to the efficacy of PDT in cancer treatment.

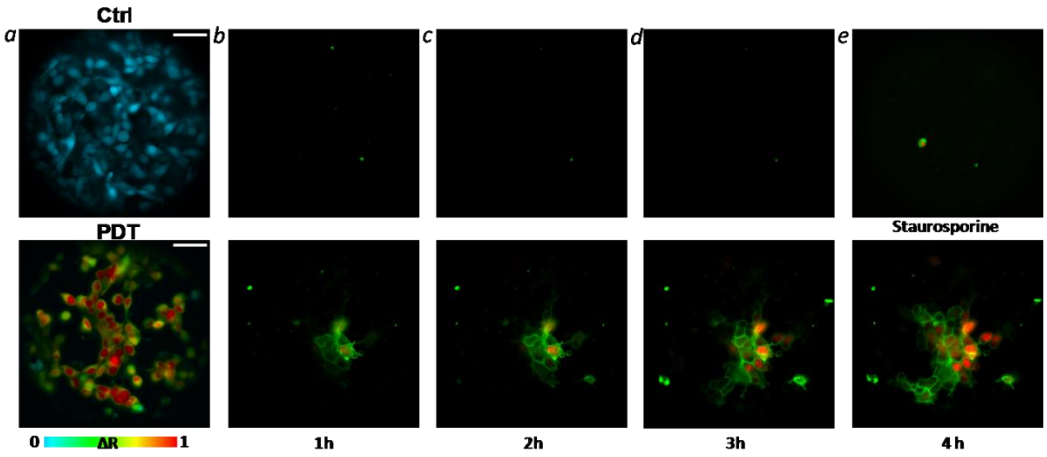

Figure7. Photosensitization induces an "apoptotic death-wave". *a*. Representative false–color images of Fura-2 fluorescence ratio variation during focal PDT in AlPC-treated C26GM cells either non-photostimulated (ctrl) or photosensitized (PDT). Fura-2 fluorescence ratio variation is encoded as shown by the color scale bar. Time-lapse microscopy was used to monitor apoptosis by real-time detection of phosphatidylserine externalization in C26GM cells subjected (PDT) or not (ctrl) to focal PDT. Representative color-merged images of C26GM cells; propidium iodide fluorescence (red) and pSIVA fluorescence (green) at the indicated time (h, hours) following or not focal PDT. As an apoptosis positive-control, cells were incubated with Staurosporine (*e*, *upper image*). Scale bars, 50 μm.

Several studies of apoptotic cell death induced by PDT claimed the involvement of both the extrinsic or intrinsic pathway (Castano, Demidova et al. 2005). While the extrinsic pathway requires the binding of death receptor Fas to its ligand FasL and subsequent activation of caspase-8, the intrinsic pathway involves the loss of mitochondrial membrane potential, cytochrome c release and caspase-9 activation. To single out the prevailing pathway in the apoptotic process triggered by focal PDT, cells were maintained at 37°C and fixed at different time points following AlPC photoactivation. Immunofluorescence staining demonstrated that cytochrome c was released in the cytosol after 1 hour, from bystander cells within 1 mm from the PDT target, as well as in those located 5-8 mm from it (**Figure8).** Control samples provided additional evidence of the PS safety unless photoactivated.

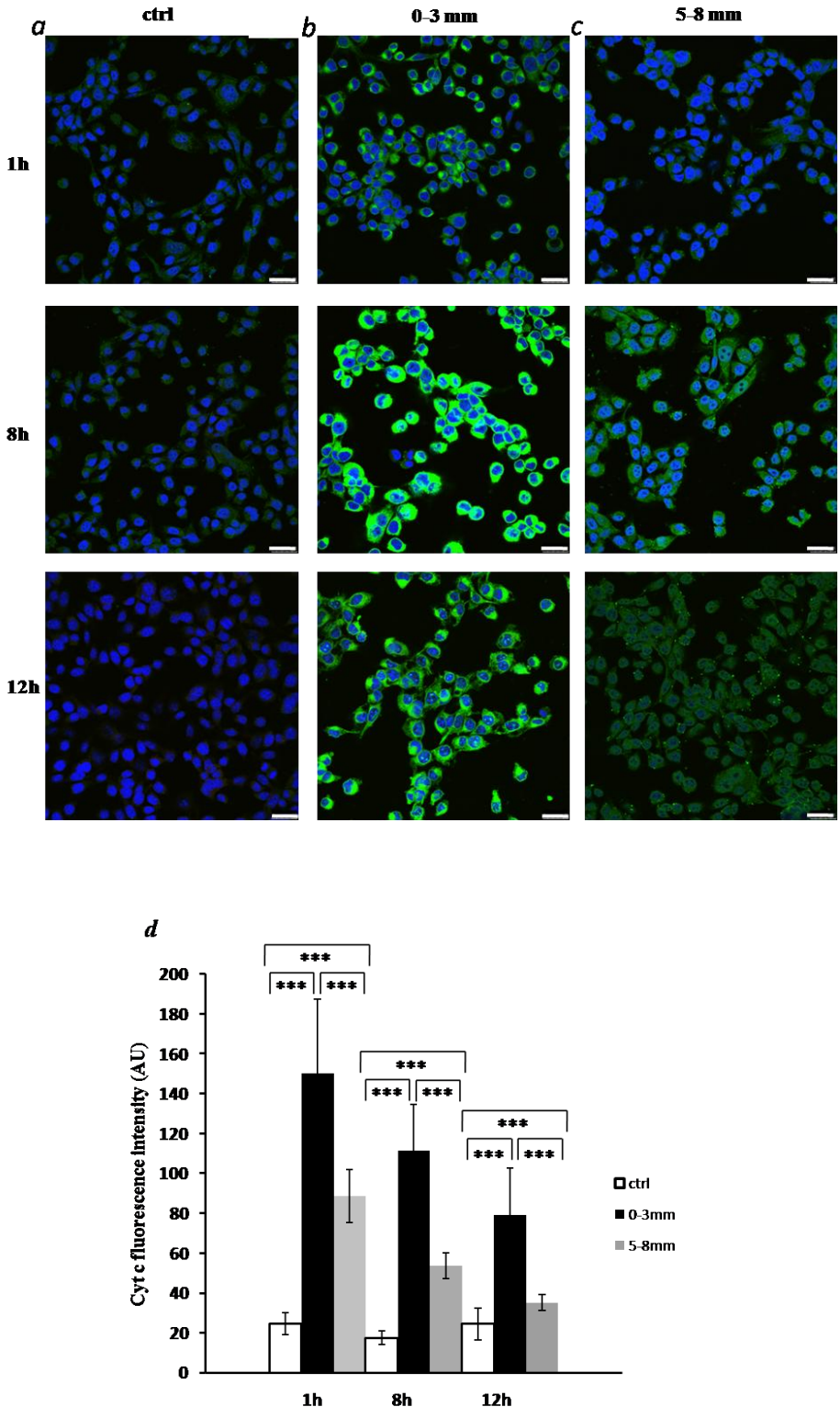

Figure8. PDT induced apoptosis via cytochrome c release. Confocal images of control and PDT-treated C26GM cells immunostained for cytochrome c (green fluorescence) and counterstained with the nuclear dye Hoechst (blue). *a* AlPC-loaded but not photosensitized cells (ctrl) were fixed at the indicated time points. Cytochrome c immunostaining of C26GM cells located within 1 mm (*b*) or 5-8 mm (*c*) from the PDT-targeted cell. (Scale bar, 25 µm)**.** *d***.** Graph depicting quantification of cytocrome c staining (mean of fluorescence intensty, n = 50 ROIs per field). Statistical analysis was performed using Student's *t* test.

NO release during PDT is partially dependent on extracellular Ca^{2+}

The notion that NO production from constitutive NOS is dependent on intracellular Ca^{2+} concentration is generally accepted. However, it is not clear whether NOS activation is caused by Ca^{2+} release from intracellular stores or Ca^{2+} influx through store-operated or other plasma membrane channels permeable to Ca^{2+} ions. Studies with pulmonary artery endothelial cells showed that Ca^{2+} release from internal stores has a small but significant effect on NO production after ATP stimulation (Wang, Shin et al. 1996). Conversely, another report suggested that store-operated Ca^{2+} influx can activate NOS3 in endothelial cells, and NOS activity is more sensitive to Ca^{2+} entry through store-operated Ca^{2+} channels than to Ca^{2+} release from intracellular stores (Lin, Fagan et al. 2000). To dissect the link between intracellular Ca^{2+} increase and NO production in bystander responses triggered by PDT, we performed focal PDT experiments after removing Ca^{2+} from the extracellular medium (using the Ca^{2+} chelator EGTA, 100 μM). To minimize the variability due to the difference in fluorescent probe cell loading, for each EGTA experiment, control recordings were acquired from different fields of view of the same C26GM monolayer before incubation in a nominally Ca^{2+} free medium supplemented with EGTA. As expected, both amplitude and rate of increase of intracellular Ca^{2+} variations were significatly reduced ($p<0.03$ and $p<10^{-14}$, respectively). Notably, analysis of NO fluorescence traces showed a dramatic reduction in both parameters ($p<10^{-14}$). In the absence of extracelluar Ca^{2+}, only 80% of cells were involved in NO wave propagation, which spread slower with respect to the control. A similar reduction affected also the Ca^{2+} wave, corroborating the hypothesis that NO production is partially dependent on Ca^{2+} influx. Furthemore, we noted a remarkable difference when comparing the rate of propagation between Ca^{2+} and NO waves in control versus EGTA. The control NO wave showed a 10 s delay with respect to the Ca^{2+} wave, whereas in the EGTA experiment this delay was increased to 20 s (**Figure9**). The residual Ca^{2+} signal which persisted in the presence of EGTA suggests the involvement of additional Ca^{2+} sources in the bystander responses evoked by PDT. Nevertheless, these data provide clear evidence that NO production by NOS during PDT may be, at least in part, dependent on Ca^{2+} influx from the extracellular medium.

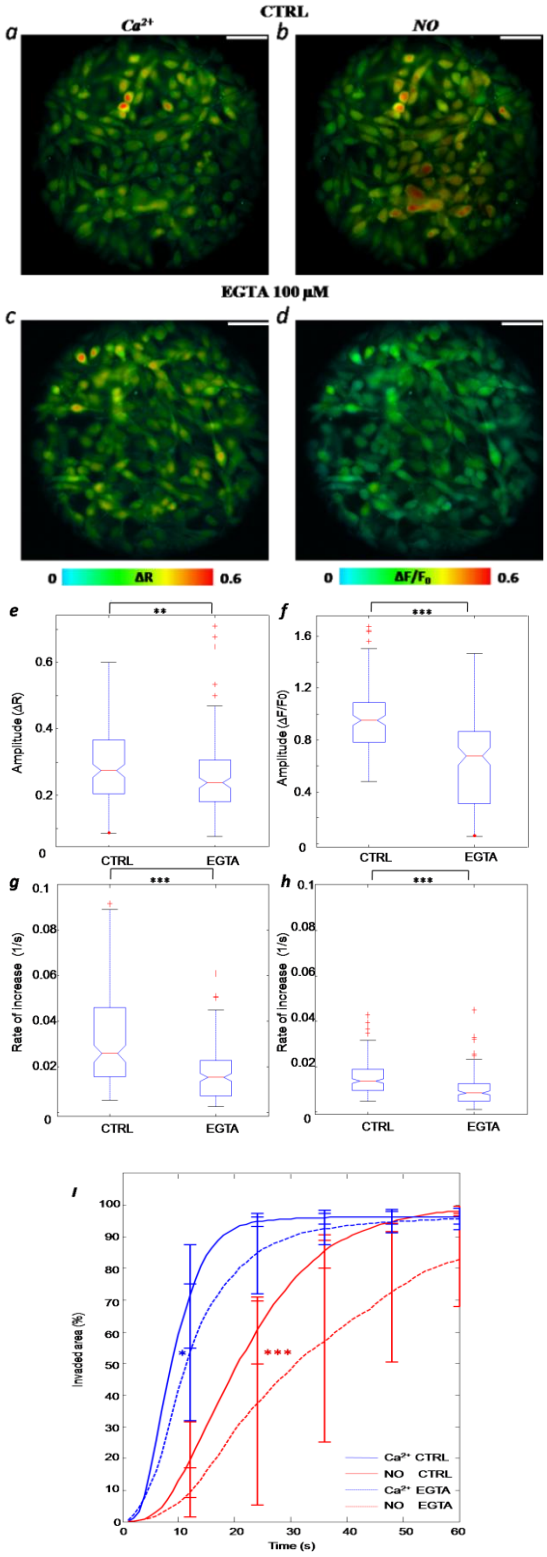

Figure9. NO synthesis during PDT is partially regulated by extracellular Ca^{2+} influx. Representative false–color images of Fura-2 and CuFL fluorescence variations, encoded as shown by the color scale bars, induced by focal PDT in control (*a, b*) and EGTA incubated C26GM (*c, d*) (Scale bar, 50 µm). *e-h*, Ca^{2+} and NO signal amplitude (*e, f*) and rate of increase (*g, h*) in control and EGTA incubated C26GM cells. *g, h.* Data were pooled from three independent experiments. Asterisks indicate significant differences between data distributions (Anova test) *i.* Area invaded by Ca^{2+} and NO waves vs. time (mean ± s.d.) for C26GM cells incubated or not with EGTA. Asterisks indicate significant differences between Ca^{2+} (blue asterisk) and NO (red asterisks) rates of wave propagation in control or EGTA incubated cells. (Student's *t* test). * $p \leq 0.05$; ** $p \leq 0.01$; *** $p \leq 0.001$.

NO synthesis during PDT is modulated by Ca^{2+} release from intracellular stores

Experiments in Ca^{2+}-free conditions showed that NO production during PDT was not totally abolished, although reduced and delayed. To investigate further the correlation between the observed intracellular Ca^{2+} and NO waves, we performed a different sets of experiments. Firstly, we used the phospholipase C (PLC) inhibitor U73122. After activation, PLC hydrolyzes phosphatidyl inositol-4,5-diphosphate (PIP2) subsequently producing diacylglycerol (DAG), which is known to activate protein kinase C (PKC), and IP3, that acting on its receptors (IP3R) on intracellular Ca^{2+} stores, triggers Ca^{2+}release (Berridge, Bootman et al. 2003). Thus, we performed focal-PDT after 10 min incubation with U73122 (2.5 μM). To minimize the variability due to the difference in fluorescent probe cell loading, control experiments were performed in different fields of view of the same C26GM samples, before U73122 incubation. Interestingly, PLC inhibition, significantly decreased both amplitude and rate of increase of intracellular Ca^{2+} variations ($p< 10^{-14}$). Noteworthy, analysis of NO fluorescence traces showed a remarkable reduction in both parameters ($p<10^{-14}$). The variance in both Ca^{2+} and NO signals induced by focal PDT resulted in delayed waves propagation which spread slower with respect to the control. (**Figure10**).

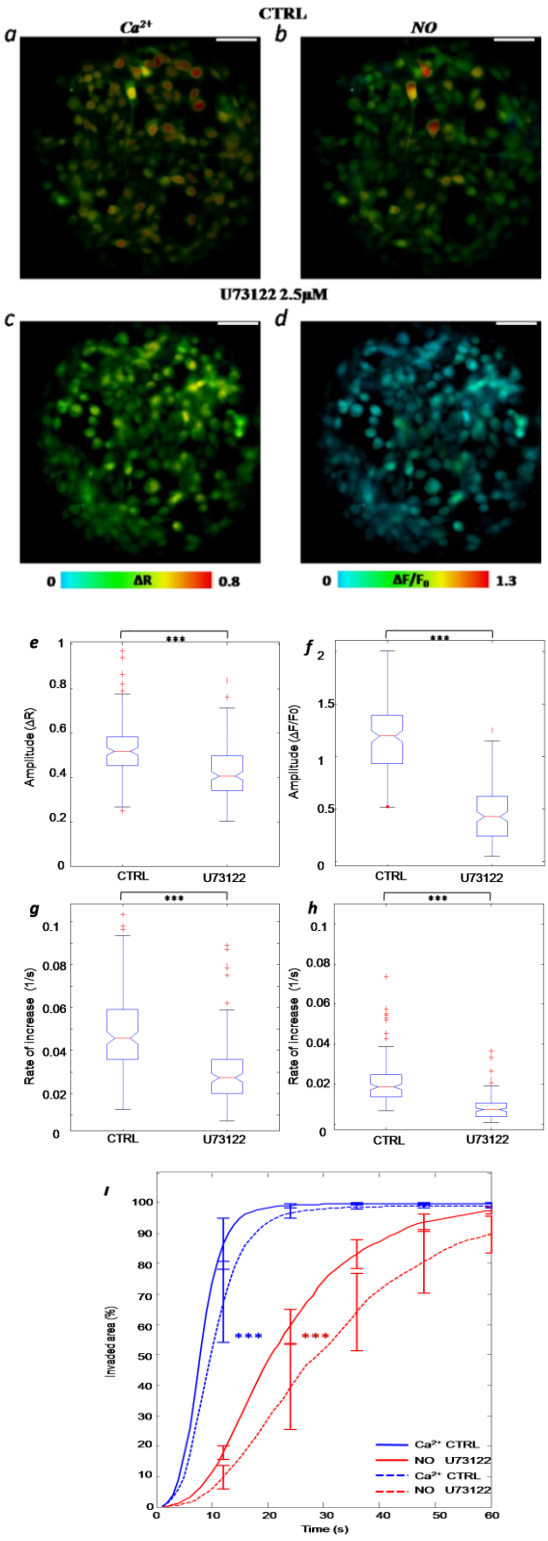

Figure10. NO production during PDT in modulated by Ca^{2+} release from intracellular stores. Representative false–color images of Fura-2 and CuFL fluorescence variations, encoded as shown by the color scale bars, induced by focal PDT in control (*a, b*) and U73122 treated C26GM cells (*c, d*) (Scale bar, 50 µm). *e-h*, Ca^{2+} and NO signal amplitude (*e, f*) and rate of increase (*g, h*) in control and U73122 incubated C26GM cells. *g, h.* Data were pooled from three independent experiments. Asterisks indicate significant differences between data distributions (Anova test). *i.* Area invaded by Ca^{2+} and NO waves vs. time (mean ± s.d.) for C26GM cells incubated or not with U73122. Asterisks indicate significant differences between Ca^{2+} (blue asterisks) and NO (red asterisks) rates of wave propagation in control or U73122 treated cells. (Student's *t* test). *** $p \leq 0.001$.

We then asked whether NO release during photosensitization could be mimicked by more "physiologic" processes not requiring the presence of the PS. In particular, we exploited the possibility to induce a cell-localized release of Ca^{2+} and evaluate its effect on nearby cells. To this end, we set up the focal photostimulation of caged- inositol 1,4,5-trisphosphate (caged-IP3) in cultured C26GM cells, which were co-loaded with Fura-red and CuFL. Since the uncaging required UV-light exposure that was also necessary for Fura-2 excitation, we used an alternative Ca^{2+} indicator (Fura-red) in combination with CuFL. Flash photolysis of caged-IP3 induced activation of its receptors (IP3R) on intracellular Ca^{2+} stores in the UV-flashed C26GM cell, triggering Ca^{2+} release (**Figure11**). Notably, when we performed 100 ms focal photostimulation of caged-IP3, we recorded a decrease of fura-red fluorescence emission (excited at 470 nm), indicative of a corresponding increase in the intracellular Ca^{2+} concentration, and a simultaneous increase of CuFL fluorescence both in the UV-flashed cell and in nearby unirradiated cells. These findings suggest that photosensitization with AlPC might trigger NO release simply by promoting Ca^{2+} realease from intracellular stores in the irradiated cell, which then generates a Ca^{2+} wave that propagates to surrounding cells and contributes to determine the therapeutic effects initiated by the PS.

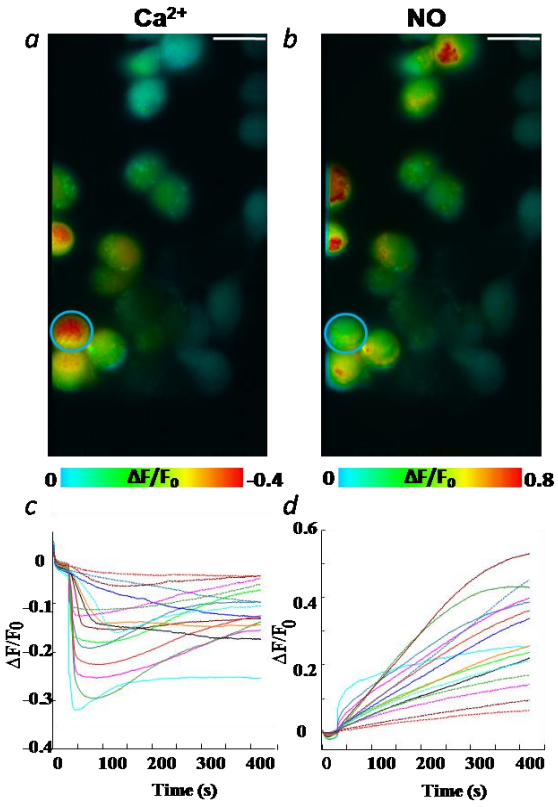

Figure11. Ca^{2+} leakage from intracellular store activate NO synthesis. *a.* Fura-red fluorescence variations (measured as $\Delta F/F_0$) of Ca^{2+} responses evoked by 100 ms focal photostimulation of the blue circled C26GM cell with caged IP3. *b.*Representative false–color images of CuFL fluorescence variations after IP3 uncaging encoded, as shown by the color scale bar (Scale bar, 50 μm). Fluorescence traces of Ca^{2+}(*c*) and NO (*d*) responses induced by focal photostimulation with caged-IP3.

Gap junction intercellular communication mediates bystander effect and apoptosis

The observed fast electrical coupling underpinning the Ca^{2+} and NO waves among bystander cells suggested the involvement of connexins and gap junctions in bystander response. Cx26 has been indeed reported to mediate bystander effect of gemcitabine (Garcia-Rodriguez, Perez-Torras et al. 2011) in human pancreatic tumours; while Cx43 has been demonstrated to be involved in bystander effect of HSV/tk-based cancer therapy in rat glioma cells (Sanson, Marcaud et al. 2002). Therefore, we assessed gap-junction contribution in the spread of the apoptotic death after PDT. To this aim, we performed focal PDT on C26GM cells after 15 minute incubation with the gap junction blocker flufenamic acid (FFA) (100µM). After photosensititazion, FFA was removed, cells were carefully washed by perfusion and then imaged in the presence of pSIVA and PI to monitor apoptosis spreading. FFA incubation highly reduced the percentage (16%) of both late apoptotic (pSIVA-PI double positive cells) and early apoptotic cell (pSIVA positive, PI negative cells) with respect to the control cells (37%). These data strikingly demonstrate that connexin gap junctions are necessary for mediating bystander cell death (**Figure12**).

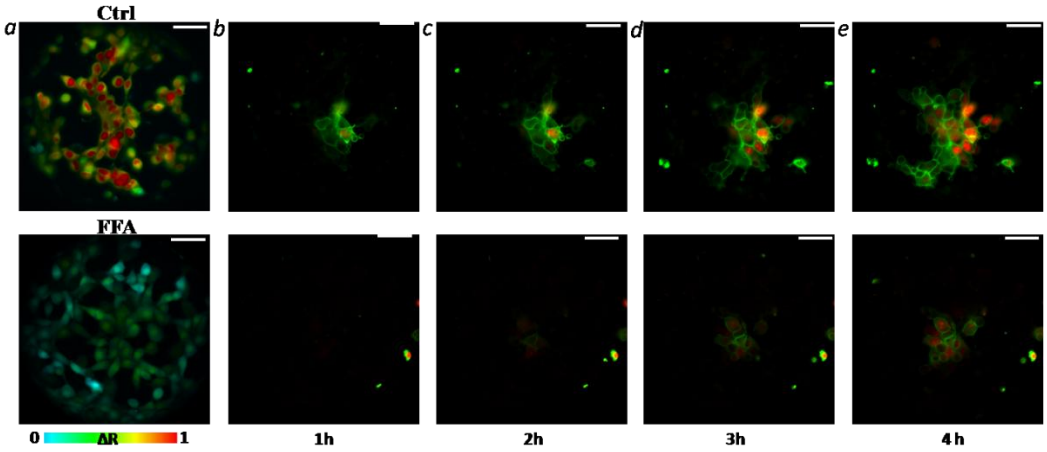

Figure12. PDT bystander cell death is mediated by connexin gap junctions. *a.* Representative false–color images of Fura-2 fluorescence ratio variation, encoded as shown by the color scale bar, during focal PDT in control and FFA incubated C26GM cells. *b-d* Time-lapse microscopy was performed to monitor apoptosis by real-time detection of phosphatidylserine externalization in C26GM cells incubated (FFA) or not (ctrl) with FFA. Representative color-merged images of C26GM cells; propidium iodide fluorescence (red) and pSIVA fluorescence (green). The hours shown indicate the time after focal PDT. (Scale bar, 50 µm).

To unveil the contribution of gap junction intercellular communication in PDT bystander signals propagation, we performed focal PDT experiments after 15 minute incubation with FFA (100μM). Under these conditions, we photosensitized the cell, located in the center of the field of view and analyzed the amplitude, rate of signal increase and extent of the Ca^{2+} and NO "death waves". FFA incubation extremely reduced the amplitude and rate of increase of intracellular Ca^{2+} transients evoked by focal PDT ($p<10^{-14}$). Noteworthy, gap junction blocking also dramatically decreased both the parameters of NO signals ($p< 10^{-14}$). These data strongly supported our hypothesis concerning the tight correlation between the two analyzed waves. Strikingly, gap junction blocking provided additional evidence for the engagement of connexins in bystander effect. Our results depict a scenario where Ca^{2+} signalling spread among juxtapposed cells via gap junctions, which allows the transfer from one cell to another of Ca^{2+} and IP3. IP3 activates its receptors on intracellular stores, thus triggering Ca^{2+} release, which in turn might be exchanged with the closest cells. This self-amplifying circuit might not be necessary for the mere NO gas diffusion. Notably, the rates of both $Ca^{2+}$and NO waves in FFA-treated cells showed a striking decrease with respect to control cells. Remarkably, the extent of NO wave during PDT was dramatically reduced in FFA-treated cells since it involved only 30% of cells in 60 seconds (**Figure13**).

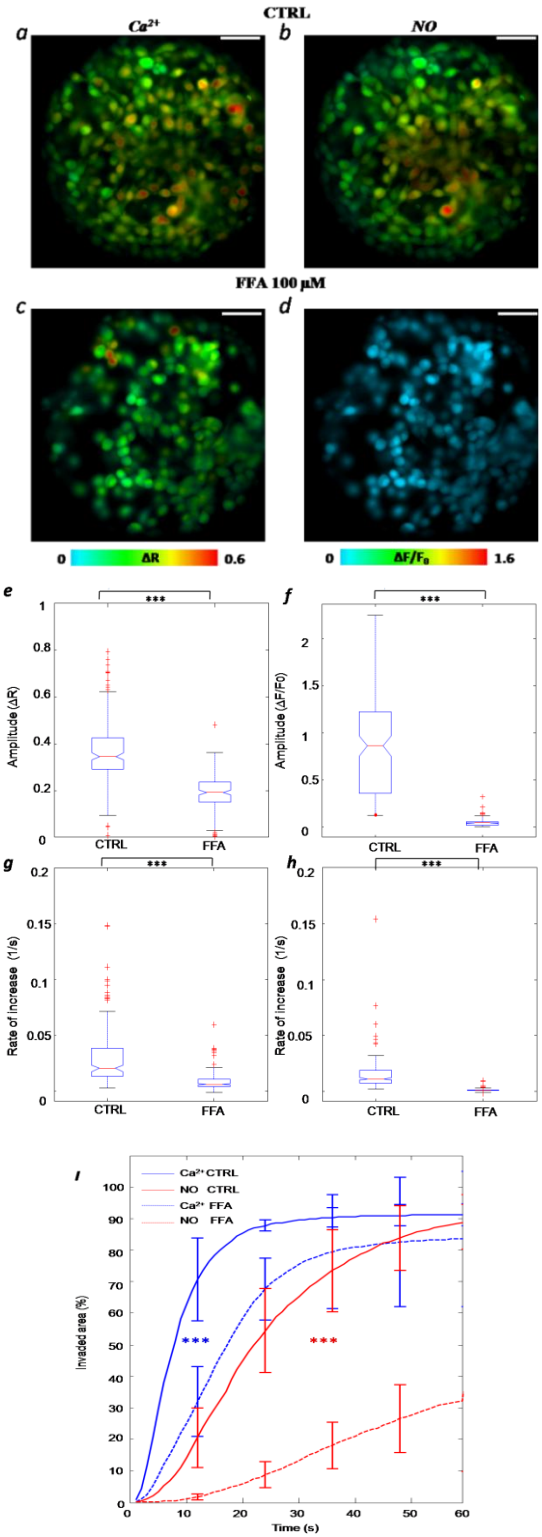

Figure13. PDT bystander effect is dependent on GJIC. Representative false–color images of Fura-2 and CuFL fluorescence variations, encoded as shown by the color scale bars, induced by focal PDT in control (*a, b*) or FFA incubated C26GM cells (*c, d*) (Scale bar, 50 µm). Ca^{2+} and NO signal amplitude (*e, f*) and rate of increase (*g, h*) in control or FFA incubated C26GM cells. Data were pooled from three independent experiments.Asterisks indicate significant differences between data distributions (Anova test). *i.* Area invaded by Ca^{2+} and NO waves vs. time (mean ± s.d.) for C26GM cells incubated or not with FFA. Asterisks indicate significant differences between Ca^{2+} (blue asterisks) and NO (red asterisks) rates of wave propagation in control or FFA incubated cells. (Student's *t* test). *** $p \leq 0.001$.

Furthermore, to corroborate our findings, we tested the expression of connexins and function of gap junctions in resting C26GM cells. We assessed the expression of five different connexins, at transcription level in C26GM cells by semi-quantitative RT-PCR. We selected Cx26, Cx30, Cx30.3, Cx40 and Cx43, because Cx26, Cx40 and Cx43 were reported to be present in human breast cancer, while Cx43 and Cx30 were detected in colon and gastrointestinal tumours, as well as head and neck cancers (Ozawa, Matsunaga et al. 2007; Sirnes, Bruun et al. 2012; Teleki, Krenacs et al. 2013) Among those tested, Cx43 resulted the most abundant in C26GM cells, whilst the other Cxs were poorly represented (**Figure14**).

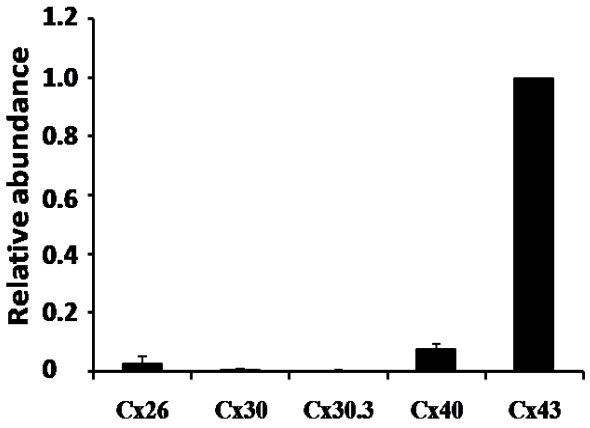

Figure14. Cx43 is highly expressed in mouse colon carcinoma C26GM cells. Total RNA was isolated from C26GM and qRT-PCR for content of indicated connexins. Data, reported as relative abundance are normalized to Cx43. GAPDH was used as positive control.

Moreover, we exploited the novel Vf2.1.Cl voltage sensitive dye (Miller, Lin et al. 2012) to probe dynamically the extent of gap junction coupling in C26GM cells by a combination of single cell electrophysiology, large scale optical recordings and a digital phase–sensitive detector of fluorescence signals (Ceriani and Mammano 2013). Intercellular coupling of C26GM cells was confirmed by probing electrical connectivity using Vf2.1.Cl, combined with voltage low frequency stimulation of one cell through a patch pipette, eliciting fluorescence responses with the same frequency in coupled cells. The incubation with carbenoxolone (CBX), a known blocker of gap junctions, dramatically reduced the number of coupled cells thus highlighting the role of gap junction in C26GM intercellular communication (**Figure15**).

Finally, these findings substantiate the established paradigm that gap junctions are instrumental for the propagation of bystander signals within tumour environment.

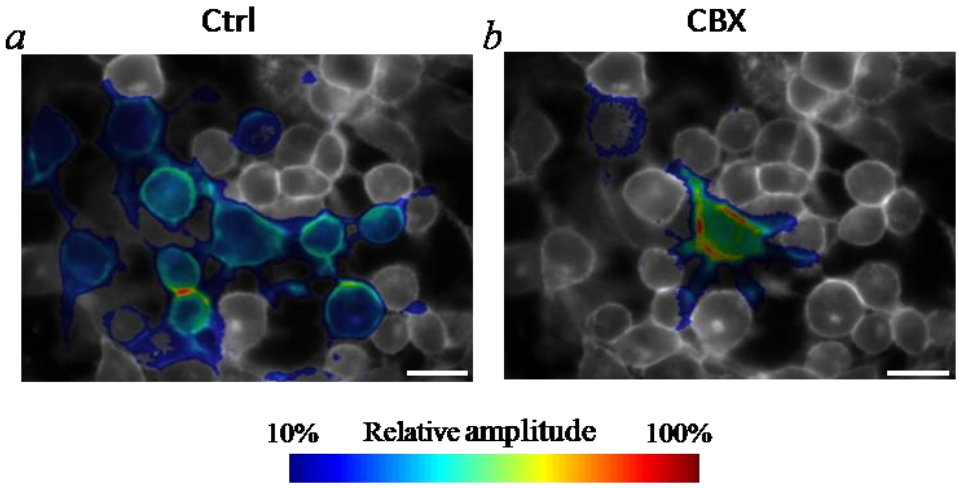

Figure15. C26GM cells are electrically coupled by gap-junctions. Intercellular coupling in C26GM cells was assayed by probing electrical connectivity using the phase–sensitive detector tecnique recently developed by prof. Mammano group (Ceriani F. et al., 2013). Cells were loaded with the Vf2.1.Cl voltage sensitive dye and voltage stimuli that consisted of low frequency (0.5 Hz) sinusoidal waveforms were delivered to one cell through a patch pipette, eliciting fluorescence rresponses with the same frequency in coupled cells. A phase sensitive detector was used offline to extract the relative amplitude of the optical signal at each pixel location (x,y) within tha field of view. Cells not connected to the one stimulated with the patch pipette are displayed in gray (*a).* Incubation with carbenoxolone (CBX) decreases the number of coupled cells (*b*).

Discussion

For a long time, radiation oncologists have reported the so-called bystander effect, meaning that the irradiation of a lesion might also have an impact on nearby non-irradiated tissues. Beyond unwanted side effects of radiotherapy, bystander effect may also enhance the efficacy of cancer treatment. Local bystander effect can, infact, induce irradiated cells to release soluble mediators that exert a direct or indirect cytotoxic activity on non-irradiated, neighbouring cells. Additionally, long-range bystander response, also known as "abscopal effect", is thought to reflect the elicitation of an adaptive immune response against malignant cells (Prise and O'Sullivan 2009; Kroemer and Zitvogel 2012; Postow, Callahan et al. 2012). Similarly to radiotherapy, photodynamic therapy (PDT) is capable of triggering bystander responses in non-irradiated cells, acting as an inducer of immunogenic cell death, thus efficiently promoting antitumour immune response (Dabrowska, Gos et al. 2005; Vacchelli, Vitale et al. 2013). Although various mediators and pathways have been suggested to be involved in bystander response and death signals propagation, to date it is not known which are the key molecules and crucial cellular mechanisms engaged for the paucity of studies focusing on the three-dimensional tumour mass. Infact, much of our knowledge on bystander effect derives from static studies that do not necessarily reflect the natural dynamics of biological processes. Therefore, many outstanding questions remain: how do cells behave, interact with one another, and exchange information within the tumour microenvironment? And how do cells respond individually and collectively to therapeutic intervention? Notwithstanding, the development of high-performing instruments and procedures for imaging of live animals at microscopic resolution, by the so-called intravital microscopy, makes it possible addressing these questions. Intravital microscopy can, infact, reveal cellular responses over time and space and can be conducted under conditions closely approximating those of a natural environment (Pittet and Weissleder 2011).

In order to image the signalling events occurring in bystander cells during antitumour treatment, we exploited intravital microscopy by taking advantage of the dorsal skinfold chamber model. This sophisticated experimental model provides the opportunity to examine, with high-resolution imaging, the whole complex cancer tissue (Baron, Welsh et al. 2011) on living tumour-bearing mice subjected to PDT. Notably, to visualize the molecular cross-talk supporting bystander response, we slightly adjusted the PDT conventional protocol (Allison 2014), since we focused the photosensitizing light to one single cell rather than to a macroscopic lesion. Since NO and RNS are crucial determinants of cancer therapy success (Khan, Van Dyk et al. 2003), we aimed at investigating NO production and spreading or diffusion within the intact tumour mass. However, the conventional methods applied for NO tracking, such as chemiluminescence and spectroscopy, suffered from low spatial resolution tracking, additionally requiring complicated instrumentation. Moreover, the widely used fluorescent

probes for NO, including o-diaminonaphthalene (DAN), o-diaminofluoresceins (DAFs) and o-diaminocyanines (DACs), require reactions with oxidized NO products rather than NO itself, thus their fluorescence-response does not necessarily reflect real-time NO production (Lim, Xu et al. 2006). Notwithstanding, the use of the novel fluorescent probe CuFl, which reacts rapidly and specifically with NO over other potentially interfering molecules, allowed us to dynamically monitor in real-time NO production from bystander cells by intravital microscopy (Lim, Xu et al. 2006). Importantly, this study provides the first direct evidence of NO involvement in bystander response within a three-dimensional tumour mass.

Noteworthy, the PDT-triggered NO wave investing bystander cells appeared to be spatially and temporally associated to generation of a very fast Ca^{2+} wave within the whole tumour mass. These data, consistently with the notion that NO synthesis may be Ca^{2+} -dependent, at least for the constitutive NOS isoforms (McMurry, Chrestensen et al. 2011) supported the hypothesis that constitutive NOS activity might be crucial for the beneficial spread of bystander response and death signals propagation. Additionally, in agreement with previous reports, this study demonstrates that NO induces apoptotic cell death through the intrinsic apoptotic pathway and cytochrome c release (Snyder, Shroff et al. 2009). However, despite numerous studied showed the involvementof NOS2 in response to cancer therapy, the role of constitutive NOS has not yet well investigated. Several findings suggested that photosensitization of breast cancer as well as prostate cancer cells resulted in a rapid and prolonged upregulation of NOS2 following irradiation; in this case, by acting as cyto-protector, NO induces both a pro-survival and pro-growth response, thus compromising PDT efficacy (Bhowmick and Girotti 2013). Conversely, other evidence demonstrated that blocking NO production by L-NAME administration, significantly reduced the efficacy of a combinatorial therapy, based on IL-3-enhanced HSV-tk/GCV viral system (Yu, Hong et al. 2013). Therefore, our data highlight the need to investigate further the role of constitutive NOS, primarily NOS3, in response to cancer treatment.

Although the aforementioned notion that NO release may be dependent on intracellular Ca^{2+} concentration, it is not clear whether constitutive NOS activation is caused by the release from either intracellular stores or Ca^{2+} influx through store-operated Ca^{2+}channels. It has infact been demonstrated that only the Ca^{2+} release from internal stores might affect NO production following ATP stimulation (Wang, Shin et al. 1996). Conversely, other evidence suggested that NOS activity is more sensitive to Ca^{2+} entry through store-operated Ca^{2+} channels than the release from intracellular stores (Lin, Fagan et al. 2000). Importantly, our data demonstrated that PDT induced bystander effect is accompanied by a NO wave, only partially dependent on Ca^{2+}entry from the extracellular space, but significantly influenced by Ca^{2+}release from intracellular stores. Furthermore, PLC inhibition did not result in the complete abrogation of Ca^{2+} transients in bystander cells, suggesting that other intracellular Ca^{2+} stores might be engaged in PDT-induced bystander response. Indeed, besides the well-characterized endoplasmic reticulum endowed with the capacity of accumulating and releasing

Ca^{2+}, other vesicular compartments, such as mitochondria, the Golgi apparatus, secretory granules, lysosomes, and endocytic vesicles, are known to accumulate Ca^{2+} and to be capable of releasing it under some conditions (Rizzuto and Pozzan 2006; Rizzuto, De Stefani et al. 2012). Infact, several line of evidence support the participation of mitochondria in Ca^{2+} homeostasis maintenance and regulation of apoptotic process, as they may release caspase cofactors (Pinton, Giorgi et al. 2008). Nonetheless, increasing findings demonstrated aberrant expression of Ca^{2+} transporters in various cancer types, (Chen, Chen et al. 2013; Leanza, Biasutto et al. 2013) thus adding further complexity to the understanding of Ca^{2+} signalling in bystander response within the tumour. Moreover, Ca^{2+} permeable ion channels have emerged as important regulators of autophagy, the cellular catabolic process for the degradation and recycling of protein aggregates and damaged organelles, which participates in the maintenance of cellular homeostasis. Additionally, current evidence indicates that elevated autophagy is often detected in cancer cells in response to radiation and chemotherapy, as well asto PDT, where it contributes to the therapy resistance of cancers (Andrzejak, Price et al. 2011; Kondratskyi, Yassine et al. 2013). Conversely, chemotherapy-induced autophagy in tumour cells was associated with enhanced antitumour effect of combined immunotherapy, as a consequence of the upregulation of the mannose-6-phosphate receptor on tumour cell surface (Ramakrishnan, Huang et al. 2012). Thus, unravelling the molecular and cellular networks sustained by Ca^{2+} signalling within the tumour microenvironment might prompt the development of more successful combined strategy against cancer.

The present study also points out the crucial role of gap junctions in mediating the bystander effect, in agreement with other reports suggesting that Cx26 as well as Cx43, act as key factors in mediating either gemcitabine or HSV-TK based-therapy bystander effect, respectively (McMasters, Saylors et al. 1998; Garcia-Rodriguez, Perez-Torras et al. 2011). Noteworthy, connexin expression in tumours might serve as prognostic biomarker to predict disease outcome. Specifically, reduced expression of Cx43 in human colorectal tumours has been associated with a significantly poorer clinical outcome (Sirnes, Bruun et al. 2012), as well as increased Cx46 positivity together with reduced Cx26 expression in breast cancer, was reported to improve the assessment of pathological response to neoadjuvant chemotherapy (Teleki, Krenacs et al. 2013). Taken together, our results raise the opportunity to develop novel combinatorial approaches for cancer therapy, aimed at enhancing intercellular communication mediated by gap junctions, thus amplifying bystander response. Intriguingly, the administration of all-trans retinoic acid (ATRA) has been demonstrated to increase gap junctional intercellular communication (GJIC) in a number of cancer cell types (Wang, Dai et al. 2013; Wu, Taylor et al. 2013), and increase the efficacy of chemotherapy in human hepatocellular carcinoma (Yang, Qin et al. 2014). Moreover, the administration of the gap junction enhancer quinoline in tumour-bearing mice was recently reported to increase Cx43 expression in tumour, significantly reducing tumour growth (Heiniger, Gakhar et al. 2010; Shishido, Delahaye et al. 2014). Our data indicate that, although infrequently exploited, PDT might represent an

excellent promising option for cancer treatment, thanks to its ability to trigger a powerful bystander response. Additionally, data also suggest that the use of Ca^{2+} mobilizing agents, such as IP3, NO-donors, and gap junction enhancers could strikingly modulate the bystander effect of cancer therapy and their appropriate combinations might promote tumour eradication (Rapozzi, Della Pietra et al. 2013). Lastly, the powerful immunostimulatory properties ascribed to PDT, such as macrophage activation (Song, Zhou et al. 2013) and T lymphocyte stimulation (Mroz, Vatansever et al. 2013), pave the way for the development of novel strategies to eradicate cancer by multiple attacks.

Abbreviations

AlPC	Aluminum Phthalocyanine Chloride
Ca^{2+}	Calcium ion
CBX	Carbenoxolone
CuFL	2-{4,5-Bis[(6-(2-ethoxy-2-oxoethoxy)-2-methylquinolin-8 ylamino)methyl] 6-hydoxy-3-oxo-3H-xanthen-9-yl}benzoic acid FL
Cx	Connexin
Cyt c	Cytochrome c
DSWC	Dorsal Skinfold Window Chamber
EGTA	Ethylene Glycol-bis(beta-aminoethyl ether)-N,N,N',N'-Tetraacetic Acid
FFA	Flufenamic Acid
GJIC	Gap junction intercellular communication
GM-CSF	Granulocyte Macrophage Colony Stimulating Factor
IP3	Inositol 1,4,5-trisphosphate
L-NAME	L-N^{ω}-nitro-L-Arginine Methyl Ester
NO	Nitric Oxide
NOS	Nitric Oxide Synthase
PDT	Photodynamic Therapy
PI	Propidium Iodide
PS	Photosensitizer
pSIVA	Polarity Sensitive Indicator of Viability and Apoptosis
RNS	Reactive Nitrogen Species
ROI	Region Of Interest

References

Ahmad, N., S. Gupta, et al. (2000). "Involvement of Fas (APO-1/CD-95) during photodynamic-therapy-mediated apoptosis in human epidermoid carcinoma A431 cells." J Invest Dermatol **115**(6): 1041-1046.

Alderton, W. K., C. E. Cooper, et al. (2001). "Nitric oxide synthases: structure, function and inhibition." Biochem J **357**(Pt 3): 593-615.

Alexander, D. B. and G. S. Goldberg (2003). "Transfer of biologically important molecules between cells through gap junction channels." Curr Med Chem **10**(19): 2045-2058.

Ali, S. M., S. K. Chee, et al. (2002). "Photodynamic therapy induced Fas-mediated apoptosis in human carcinoma cells." Int J Mol Med **9**(3): 257-270.

Allison, R. R. (2014). "Photodynamic therapy: oncologic horizons." Future Oncol **10**(1): 123-124.

Almeida, R. D., B. J. Manadas, et al. (2004). "Intracellular signaling mechanisms in photodynamic therapy." Biochim Biophys Acta **1704**(2): 59-86.

Alvarez, B. and R. Radi (2003). "Peroxynitrite reactivity with amino acids and proteins." Amino Acids **25**(3-4): 295-311.

Andrzejak, M., M. Price, et al. (2011). "Apoptotic and autophagic responses to photodynamic therapy in 1c1c7 murine hepatoma cells." Autophagy **7**(9): 979-984.

Arai, K., S. Takano, et al. (2008). "S100A8 and S100A9 overexpression is associated with poor pathological parameters in invasive ductal carcinoma of the breast." Curr Cancer Drug Targets **8**(4): 243-252.

Balkwill, F. and A. Mantovani (2001). "Inflammation and cancer: back to Virchow?" Lancet **357**(9255): 539-545.

Balkwill, F. R. and A. Mantovani (2012). "Cancer-related inflammation: common themes and therapeutic opportunities." Semin Cancer Biol **22**(1): 33-40.

Baron, E. D., C. L. Malbasa, et al. (2010). "Silicon phthalocyanine (Pc 4) photodynamic therapy is a safe modality for cutaneous neoplasms: results of a phase 1 clinical trial." Lasers Surg Med **42**(10): 728-735.

Baron, V. T., J. Welsh, et al. (2011). "Intravital microscopy in the mouse dorsal chamber model for the study of solid tumors." Am J Cancer Res **1**(5): 674-686.

Baskar, R. (2010). "Emerging role of radiation induced bystander effects: Cell communications and carcinogenesis." Genome Integr **1**(1): 13.

Berridge, M. J., M. D. Bootman, et al. (2003). "Calcium signalling: dynamics, homeostasis and remodelling." Nat Rev Mol Cell Biol **4**(7): 517-529.

Berridge, M. J., P. Lipp, et al. (2000). "The versatility and universality of calcium signalling." Nat Rev Mol Cell Biol **1**(1): 11-21.

Bhowmick, R. and A. W. Girotti (2013). "Cytoprotective Signaling Associated with Nitric Oxide Upregulation in Tumor Cells Subjected to Photodynamic Therapy-like Oxidative Stress." Free Radical Biology and Medicine **57**: 39-48.

Bingisser, R. M., P. A. Tilbrook, et al. (1998). "Macrophage-derived nitric oxide regulates T cell activation via reversible disruption of the Jak3/STAT5 signaling pathway." J Immunol **160**(12): 5729-5734.

Blyth, B. J. and P. J. Sykes (2011). "Radiation-induced bystander effects: what are they, and how relevant are they to human radiation exposures?" Radiat Res **176**(2): 139-157.

Bronte, V., P. Serafini, et al. (2003). "IL-4-induced arginase 1 suppresses alloreactive T cells in tumor-bearing mice." J Immunol **170**(1): 270-278.

Burney, S., J. L. Caulfield, et al. (1999). "The chemistry of DNA damage from nitric oxide and peroxynitrite." Mutat Res **424**(1-2): 37-49.

Castano, A. P., T. N. Demidova, et al. (2004). "Mechanisms in photodynamic therapy: part one–photosensitizers, photochemistry and cellular localization." Photodiagnosis and Photodynamic Therapy **1:** 279-293.

Castano, A. P., T. N. Demidova, et al. (2005). " Mechanisms in photodynamic therapy: part two–cellular signaling, cell metabolism and modes of cell death." Photodiagnosis and Photodynamic Therapy **1:** 1-23.

Castano, A. P., P. Mroz, et al. (2006). "Photodynamic therapy and anti-tumour immunity." Nat Rev Cancer **6**(7): 535-545.

Ceriani, F. and F. Mammano (2013). "A rapid and sensitive assay of intercellular coupling by voltage imaging of gap junction networks." Cell Commun Signal **11**(1): 78.

Chao, J. I., P. C. Kuo, et al. (2004). "Down-regulation of survivin in nitric oxide-induced cell growth inhibition and apoptosis of the human lung carcinoma cells." J Biol Chem **279**(19): 20267-20276.

Charles, I. G., R. M. Palmer, et al. (1993). "Cloning, characterization, and expression of a cDNA encoding an inducible nitric oxide synthase from the human chondrocyte." Proc Natl Acad Sci U S A **90**(23): 11419-11423.

Chen, Y. F., Y. T. Chen, et al. (2013). "Remodeling of calcium signaling in tumor progression." J Biomed Sci **20**: 23.

Cheng, P., C. A. Corzo, et al. (2008). "Inhibition of dendritic cell differentiation and accumulation of myeloid-derived suppressor cells in cancer is regulated by S100A9 protein." J Exp Med **205**(10): 2235-2249.

Cheung, W. Y. (1980). "Calmodulin plays a pivotal role in cellular regulation." Science **207**(4426): 19-27.

Cho, H. J., Q. W. Xie, et al. (1992). "Calmodulin is a subunit of nitric oxide synthase from macrophages." J Exp Med **176**(2): 599-604.

Chung, S. S., C. Choi, et al. (2010). "Aberrant distribution of junctional complex components in retinoic acid receptor alpha-deficient mice." Microsc Res Tech **73**(6): 583-596.

Contreras, J. E., H. A. Sanchez, et al. (2004). "Role of connexin-based gap junction channels and hemichannels in ischemia-induced cell death in nervous tissue." Brain Res Brain Res Rev **47**(1-3): 290-303.

Crane, B. R., A. S. Arvai, et al. (1997). "The structure of nitric oxide synthase oxygenase domain and inhibitor complexes." Science **278**(5337): 425-431.

Crane, B. R., A. S. Arvai, et al. (1998). "Structure of nitric oxide synthase oxygenase dimer with pterin and substrate." Science **279**(5359): 2121-2126.

Crane, B. R., R. J. Rosenfeld, et al. (1999). "N-terminal domain swapping and metal ion binding in nitric oxide synthase dimerization." EMBO J **18**(22): 6271-6281.

Dabrowska, A., M. Gos, et al. (2005). ""Bystander effect" induced by photodynamically or heat-injured ovarian carcinoma cells (OVP10) in vitro." Medical Science Monitor **11**(9): Br316-Br324.

De Stefani, D., A. Raffaello, et al. (2011). "A forty-kilodalton protein of the inner membrane is the mitochondrial calcium uniporter." Nature **476**(7360): 336-340.

Decrock, E., D. V. Krysko, et al. (2012). "Transfer of IP(3) through gap junctions is critical, but not sufficient, for the spread of apoptosis." Cell Death Differ **19**(6): 947-957.

Denicola, A., J. M. Souza, et al. (1998). "Diffusion of peroxynitrite across erythrocyte membranes." Proc Natl Acad Sci U S A **95**(7): 3566-3571.

Dimmeler, S., J. Haendeler, et al. (1997). "Suppression of apoptosis by nitric oxide via inhibition of interleukin-1beta-converting enzyme (ICE)-like and cysteine protease protein (CPP)-32-like proteases." J Exp Med **185**(4): 601-607.

Dolmans, D. E., D. Fukumura, et al. (2003). "Photodynamic therapy for cancer." Nat Rev Cancer **3**(5): 380-387.

Dougherty, T. J., C. J. Gomer, et al. (1998). "Photodynamic therapy." J Natl Cancer Inst **90**(12): 889-905.

Feng, M., D. M. Grice, et al. (2010). "Store-independent activation of Orai1 by SPCA2 in mammary tumors." Cell **143**(1): 84-98.

Feng, M. Y. and R. Rao (2013). "New insights into store-independent Ca(2+) entry: secretory pathway calcium ATPase 2 in normal physiology and cancer." Int J Oral Sci **5**(2): 71-74.

Franchi, A., D. Massi, et al. (2006). "Inducible nitric oxide synthase activity correlates with lymphangiogenesis and vascular endothelial growth factor-C expression in head and neck squamous cell carcinoma." J Pathol **208**(3): 439-445.

Fridlender, Z. G., J. Sun, et al. (2009). "Polarization of tumor-associated neutrophil phenotype by TGF-beta: "N1" versus "N2" TAN." Cancer Cell **16**(3): 183-194.

Fukumura, D., S. Kashiwagi, et al. (2006). "The role of nitric oxide in tumour progression." Nat Rev Cancer **6**(7): 521-534.

Gabrilovich, D. (2004). "Mechanisms and functional significance of tumour-induced dendritic-cell defects." Nat Rev Immunol **4**(12): 941-952.

Gabrilovich, D. I., S. Ostrand-Rosenberg, et al. (2012). "Coordinated regulation of myeloid cells by tumours." Nat Rev Immunol **12**(4): 253-268.

Gajewski, T. F., H. Schreiber, et al. (2013). "Innate and adaptive immune cells in the tumor microenvironment." Nat Immunol **14**(10): 1014-1022.

Galdiero, M. R., C. Garlanda, et al. (2013). "Tumor associated macrophages and neutrophils in tumor progression." J Cell Physiol **228**(7): 1404-1412.

Galon, J., F. Pages, et al. (2012). "Cancer classification using the Immunoscore: a worldwide task force." J Transl Med **10**: 205.

Garban, H. J. and B. Bonavida (2001). "Nitric oxide inhibits the transcription repressor Yin-Yang 1 binding activity at the silencer region of the Fas promoter: a pivotal role for nitric oxide in the up-regulation of Fas gene expression in human tumor cells." J Immunol **167**(1): 75-81.

Garcia-Rodriguez, L., S. Perez-Torras, et al. (2011). "Connexin-26 is a key factor mediating gemcitabine bystander effect." Mol Cancer Ther **10**(3): 505-517.

Gebhardt, C., J. Nemeth, et al. (2006). "S100A8 and S100A9 in inflammation and cancer." Biochem Pharmacol **72**(11): 1622-1631.

Goc, J., C. Germain, et al. (2013). "Dendritic cells in tumor-associated tertiary lymphoid structures license the positive prognostic value of tumor-infiltrating CD8+ T cells." Cancer Res.

Golab, J., G. Wilczynski, et al. (2000). "Potentiation of the anti-tumour effects of Photofrin-based photodynamic therapy by localized treatment with G-CSF." Br J Cancer **82**(8): 1485-1491.

Gomes, E. R., R. D. Almeida, et al. (2002). "Nitric oxide modulates tumor cell death induced by photodynamic therapy through a cGMP-dependent mechanism." Photochem Photobiol **76**(4): 423-430.

Govers, R. and T. J. Rabelink (2001). "Cellular regulation of endothelial nitric oxide synthase." Am J Physiol Renal Physiol **280**(2): F193-206.

Grebenova, D., K. Kuzelova, et al. (2003). "Mitochondrial and endoplasmic reticulum stress-induced apoptotic pathways are activated by 5-aminolevulinic acid-based photodynamic therapy in HL60 leukemia cells." J Photochem Photobiol B **69**(2): 71-85.

Greenacre, S. A. and H. Ischiropoulos (2001). "Tyrosine nitration: localisation, quantification, consequences for protein function and signal transduction." Free Radic Res **34**(6): 541-581.

Grice, D. M., I. Vetter, et al. (2010). "Golgi calcium pump secretory pathway calcium ATPase 1 (SPCA1) is a key regulator of insulin-like growth factor receptor (IGF1R) processing in the basal-like breast cancer cell line MDA-MB-231." J Biol Chem **285**(48): 37458-37466.

Grivennikov, S. I., F. R. Greten, et al. (2010). "Immunity, inflammation, and cancer." Cell **140**(6): 883-899.

Hall, A. V., H. Antoniou, et al. (1994). "Structural organization of the human neuronal nitric oxide synthase gene (NOS1)." J Biol Chem **269**(52): 33082-33090.

Hanahan, D. and L. M. Coussens (2012). "Accessories to the crime: functions of cells recruited to the tumor microenvironment." Cancer Cell **21**(3): 309-322.

Hanahan, D. and R. A. Weinberg (2011). "Hallmarks of cancer: the next generation." Cell **144**(5): 646-674.

Hanlon, J. G., K. Adams, et al. (2001). "Induction of Hsp60 by Photofrin-mediated photodynamic therapy." J Photochem Photobiol B **64**(1): 55-61.

Heiniger, B., G. Gakhar, et al. (2010). "Second-generation substituted quinolines as anticancer drugs for breast cancer." Anticancer Res **30**(10): 3927-3932.

Huang, Q., S. Shan, et al. (1999). "Noninvasive visualization of tumors in rodent dorsal skin window chambers." Nat Biotechnol **17**(10): 1033-1035.

Huie, R. E. and S. Padmaja (1993). "The reaction of no with superoxide." Free Radic Res Commun **18**(4): 195-199.

Jalili, A., M. Makowski, et al. (2004). "Effective photoimmunotherapy of murine colon carcinoma induced by the combination of photodynamic therapy and dendritic cells." Clin Cancer Res **10**(13): 4498-4508.

Janssens, S. P., A. Shimouchi, et al. (1992). "Cloning and expression of a cDNA encoding human endothelium-derived relaxing factor/nitric oxide synthase." J Biol Chem **267**(21): 14519-14522.

Jiang, H., D. J. Granville, et al. (2002). "Selective action of the photosensitizer QLT0074 on activated human T lymphocytes." Photochem Photobiol **76**(2): 224-231.

Junttila, M. R. and F. J. de Sauvage (2013). "Influence of tumour micro-environment heterogeneity on therapeutic response." Nature **501**(7467): 346-354.

Kakizawa, S., T. Yamazawa, et al. (2012). "Nitric oxide-induced calcium release via ryanodine receptors regulates neuronal function." EMBO J **31**(2): 417-428.

Kawczyk-Krupka, A., Z. Czuba, et al. (2011). "The role of photosensitized macrophages in photodynamic therapy." Oncol Rep **26**(1): 275-280.

Khan, M. A., J. Van Dyk, et al. (2003). "Partial volume rat lung irradiation; assessment of early DNA damage in different lung regions and effect of radical scavengers." Radiother Oncol **66**(1): 95-102.

Kim, H. R., Y. Luo, et al. (1999). "Enhanced apoptotic response to photodynamic therapy after bcl-2 transfection." Cancer Res **59**(14): 3429-3432.

Kim, Y. E., J. Chen, et al. (2010). "Monitoring apoptosis and neuronal degeneration by real-time detection of phosphatidylserine externalization using a polarity-sensitive indicator of viability and apoptosis." Nat Protoc **5**(8): 1396-1405.

King, T. J. and J. S. Bertram (2005). "Connexins as targets for cancer chemoprevention and chemotherapy." Biochim Biophys Acta **1719**(1-2): 146-160.

Knowles, R. G. and S. Moncada (1994). "Nitric oxide synthases in mammals." Biochem J **298 (Pt 2)**: 249-258.

Kondratskyi, A., M. Yassine, et al. (2013). "Calcium-permeable ion channels in control of autophagy and cancer." Front Physiol **4**: 272.

Korbelik, M., C. S. Parkins, et al. (2000). "Nitric oxide production by tumour tissue: impact on the response to photodynamic therapy." Br J Cancer **82**(11): 1835-1843.

Korbelik, M., J. Sun, et al. (2001). "Interaction between photodynamic therapy and BCG immunotherapy responsible for the reduced recurrence of treated mouse tumors." Photochem Photobiol **73**(4): 403-409.

Kroemer, G. and L. Zitvogel (2012). "Abscopal but desirable The contribution of immune responses to the efficacy of radiotherapy." Oncoimmunology **1**(4).

Lahdenranta, J., J. Hagendoorn, et al. (2009). "Endothelial nitric oxide synthase mediates lymphangiogenesis and lymphatic metastasis." Cancer Res **69**(7): 2801-2808.

Lancaster, J. R., Jr. (1997). "A tutorial on the diffusibility and reactivity of free nitric oxide." Nitric Oxide **1**(1): 18-30.

Leanza, L., L. Biasutto, et al. (2013). "Intracellular ion channels and cancer." Front Physiol **4**: 227.

Lechner, M., P. Lirk, et al. (2005). "Inducible nitric oxide synthase (iNOS) in tumor biology: the two sides of the same coin." Semin Cancer Biol **15**(4): 277-289.

Lee, J. M., F. M. Davis, et al. (2011). "Ion channels and transporters in cancer. 4. Remodeling of Ca(2+) signaling in tumorigenesis: role of Ca(2+) transport." Am J Physiol Cell Physiol **301**(5): C969-976.

Leon, L., J. F. Jeannin, et al. (2008). "Post-translational modifications induced by nitric oxide (NO): implication in cancer cells apoptosis." Nitric Oxide **19**(2): 77-83.

Lim, M. H., D. Xu, et al. (2006). "Visualization of nitric oxide in living cells by a copper-based fluorescent probe." Nat Chem Biol **2**(7): 375-380.

Lin, S., K. A. Fagan, et al. (2000). "Sustained endothelial nitric-oxide synthase activation requires capacitative Ca2+ entry." J Biol Chem **275**(24): 17979-17985.

Loewenstein, W. R. and Y. Kanno (1967). "Intercellular communication and tissue growth. I. Cancerous growth." J Cell Biol **33**(2): 225-234.

Lukanidin, E. and J. P. Sleeman (2012). "Building the niche: the role of the S100 proteins in metastatic growth." Semin Cancer Biol **22**(3): 216-225.

Macphail, S. E., C. A. Gibney, et al. (2003). "Nitric oxide regulation of human peripheral blood mononuclear cells: critical time dependence and selectivity for cytokine versus chemokine expression." J Immunol **171**(9): 4809-4815.

Mantovani, A., P. Allavena, et al. (2008). "Cancer-related inflammation." Nature **454**(7203): 436-444.

Mantovani, A., S. Sozzani, et al. (2002). "Macrophage polarization: tumor-associated macrophages as a paradigm for polarized M2 mononuclear phagocytes." Trends Immunol **23**(11): 549-555.

Massi, D., M. C. De Nisi, et al. (2009). "Inducible nitric oxide synthase expression in melanoma: implications in lymphangiogenesis." Mod Pathol **22**(1): 21-30.

Matsuda, H. and T. Iyanagi (1999). "Calmodulin activates intramolecular electron transfer between the two flavins of neuronal nitric oxide synthase flavin domain." Biochim Biophys Acta **1473**(2-3): 345-355.

McMasters, R. A., R. L. Saylors, et al. (1998). "Lack of bystander killing in herpes simplex virus thymidine kinase-transduced colon cell lines due to deficient connexin43 gap junction formation." Hum Gene Ther **9**(15): 2253-2261.

McMurry, J. L., C. A. Chrestensen, et al. (2011). "Rate, affinity and calcium dependence of nitric oxide synthase isoform binding to the primary physiological regulator calmodulin." FEBS J **278**(24): 4943-4954.

Mehta, P. (1984). "Potential role of platelets in the pathogenesis of tumor metastasis." Blood **63**(1): 55-63.

Mesnil, M., C. Piccoli, et al. (1996). "Bystander killing of cancer cells by herpes simplex virus thymidine kinase gene is mediated by connexins." Proc Natl Acad Sci U S A **93**(5): 1831-1835.

Mesnil, M. and H. Yamasaki (2000). "Bystander effect in herpes simplex virus-thymidine kinase/ganciclovir cancer gene therapy: role of gap-junctional intercellular communication." Cancer Res **60**(15): 3989-3999.

Miller, E. W., J. Y. Lin, et al. (2012). "Optically monitoring voltage in neurons by photo-induced electron transfer through molecular wires." Proc Natl Acad Sci U S A **109**(6): 2114-2119.

Mocellin, S., V. Bronte, et al. (2007). "Nitric oxide, a double edged sword in cancer biology: searching for therapeutic opportunities." Med Res Rev **27**(3): 317-352.

Molon, B., S. Ugel, et al. (2011). "Chemokine nitration prevents intratumoral infiltration of antigen-specific T cells." J Exp Med **208**(10): 1949-1962.

Monteith, G. R., F. M. Davis, et al. (2012). "Calcium channels and pumps in cancer: changes and consequences." J Biol Chem **287**(38): 31666-31673.

Mroz, P., F. Vatansever, et al. (2013). "Photodynamic Therapy of Murine Mastocytoma Induces Specific Immune Responses against the Cancer/Testis Antigen P1A." Cancer Research **73**(21): 6462-6470.

Muntane, J., A. J. De la Rosa, et al. (2013). "Nitric oxide and cell death in liver cancer cells." Mitochondrion **13**(3): 257-262.

Munzel, T., A. Daiber, et al. (2005). "Vascular consequences of endothelial nitric oxide synthase uncoupling for the activity and expression of the soluble guanylyl cyclase and the cGMP-dependent protein kinase." Arterioscler Thromb Vasc Biol **25**(8): 1551-1557.

Nagaraj, S., K. Gupta, et al. (2007). "Altered recognition of antigen is a mechanism of CD8+ T cell tolerance in cancer." Nat Med **13**(7): 828-835.

Noble, M. A., A. W. Munro, et al. (1999). "Potentiometric analysis of the flavin cofactors of neuronal nitric oxide synthase." Biochemistry **38**(50): 16413-16418.

Norbury, C. J. and B. Zhivotovsky (2004). "DNA damage-induced apoptosis." Oncogene **23**(16): 2797-2808.

Nosho, K., Y. Baba, et al. (2010). "Tumour-infiltrating T-cell subsets, molecular changes in colorectal cancer, and prognosis: cohort study and literature review." J Pathol **222**(4): 350-366.

Ogino, S., K. Nosho, et al. (2009). "Lymphocytic reaction to colorectal cancer is associated with longer survival, independent of lymph node count, microsatellite instability, and CpG island methylator phenotype." Clin Cancer Res **15**(20): 6412-6420.

Ozawa, H., T. Matsunaga, et al. (2007). "Decreased expression of connexin-30 and aberrant expression of connexin-26 in human head and neck cancer." Anticancer Res **27**(4B): 2189-2195.

Pacher, P., J. S. Beckman, et al. (2007). "Nitric oxide and peroxynitrite in health and disease." Physiol Rev **87**(1): 315-424.

Parkash, J. and K. Asotra (2010). "Calcium wave signaling in cancer cells." Life Sci **87**(19-22): 587-595.

Pinton, P., C. Giorgi, et al. (2008). "Calcium and apoptosis: ER-mitochondria Ca2+ transfer in the control of apoptosis." Oncogene **27**(50): 6407-6418.

Pittet, M. J. and R. Weissleder (2011). "Intravital imaging." Cell **147**(5): 983-991.

Plaetzer, K., T. Kiesslich, et al. (2002). "Characterization of the cell death modes and the associated changes in cellular energy supply in response to AlPcS4-PDT." Photochem Photobiol Sci **1**(3): 172-177.

Plaetzer, K., B. Krammer, et al. (2009). "Photophysics and photochemistry of photodynamic therapy: fundamental aspects." Lasers Med Sci **24**(2): 259-268.

Polanska, U. M. and A. Orimo (2013). "Carcinoma-associated fibroblasts: non-neoplastic tumour-promoting mesenchymal cells." J Cell Physiol **228**(8): 1651-1657.

Porta, C., E. Riboldi, et al. (2011). "Mechanisms linking pathogens-associated inflammation and cancer." Cancer Lett **305**(2): 250-262.

Portilho, F. A., C. E. Cavalcanti, et al. (2013). "Antitumor activity of photodynamic therapy performed with nanospheres containing zinc-phthalocyanine." J Nanobiotechnology **11**(1): 41.

Postow, M. A., M. K. Callahan, et al. (2012). "Abscopal Effect in a Patient with Melanoma REPLY." New England Journal of Medicine **366**(21): 2035-2036.

Prise, K. M. and J. M. O'Sullivan (2009). "Radiation-induced bystander signalling in cancer therapy." Nat Rev Cancer **9**(5): 351-360.

Radi, R., J. S. Beckman, et al. (1991). "Peroxynitrite-induced membrane lipid peroxidation: the cytotoxic potential of superoxide and nitric oxide." Arch Biochem Biophys **288**(2): 481-487.

Radi, R., J. S. Beckman, et al. (1991). "Peroxynitrite oxidation of sulfhydryls. The cytotoxic potential of superoxide and nitric oxide." J Biol Chem **266**(7): 4244-4250.

Ramakrishnan, R., C. Huang, et al. (2012). "Autophagy induced by conventional chemotherapy mediates tumor cell sensitivity to immunotherapy." Cancer Res **72**(21): 5483-5493.

Rammes, A., J. Roth, et al. (1997). "Myeloid-related protein (MRP) 8 and MRP14, calcium-binding proteins of the S100 family, are secreted by activated monocytes via a novel, tubulin-dependent pathway." J Biol Chem **272**(14): 9496-9502.

Rapozzi, V., E. Della Pietra, et al. (2013). "Nitric oxide-mediated activity in anti-cancer photodynamic therapy." Nitric Oxide **30**: 26-35.

Raza, A., M. J. Franklin, et al. (2010). "Pericytes and vessel maturation during tumor angiogenesis and metastasis." Am J Hematol **85**(8): 593-598.

Reeves, K. J., M. W. Reed, et al. (2009). "Is nitric oxide important in photodynamic therapy?" J Photochem Photobiol B **95**(3): 141-147.

Reveneau, S., L. Arnould, et al. (1999). "Nitric oxide synthase in human breast cancer is associated with tumor grade, proliferation rate, and expression of progesterone receptors." Lab Invest **79**(10): 1215-1225.

Rizzuto, R., D. De Stefani, et al. (2012). "Mitochondria as sensors and regulators of calcium signalling." Nature Reviews Molecular Cell Biology **13**(9): 566-578.

Rizzuto, R., P. Pinton, et al. (2003). "Calcium and apoptosis: facts and hypotheses." Oncogene **22**(53): 8619-8627.

Rizzuto, R. and T. Pozzan (2006). "Microdomains of intracellular Ca2+: molecular determinants and functional consequences." Physiol Rev **86**(1): 369-408.

Robb-Gaspers, L. D. and A. P. Thomas (1995). "Coordination of Ca2+ signaling by intercellular propagation of Ca2+ waves in the intact liver." J Biol Chem **270**(14): 8102-8107.

Roberts, R. L. and P. C. Lin (2004). "Structural and functional optical imaging of angiogenesis in animal models." Methods Enzymol **386**: 105-122.

Roderick, H. L. and S. J. Cook (2008). "Ca2+ signalling checkpoints in cancer: remodelling Ca2+ for cancer cell proliferation and survival." Nat Rev Cancer **8**(5): 361-375.

Ryckman, C., K. Vandal, et al. (2003). "Proinflammatory activities of S100: proteins S100A8, S100A9, and S100A8/A9 induce neutrophil chemotaxis and adhesion." J Immunol **170**(6): 3233-3242.

Ryter, S. W. and C. J. Gomer (1993). "Nuclear factor kappa B binding activity in mouse L1210 cells following photofrin II-mediated photosensitization." Photochem Photobiol **58**(5): 753-756.

Saji, H., W. Song, et al. (2006). "Systemic antitumor effect of intratumoral injection of dendritic cells in combination with local photodynamic therapy." Clin Cancer Res **12**(8): 2568-2574.

Salama, I., P. S. Malone, et al. (2008). "A review of the S100 proteins in cancer." Eur J Surg Oncol **34**(4): 357-364.

Sanson, M., V. Marcaud, et al. (2002). "Connexin 43-mediated bystander effect in two rat glioma cell models." Cancer Gene Ther **9**(2): 149-155.

Santamaria-Kisiel, L., A. C. Rintala-Dempsey, et al. (2006). "Calcium-dependent and -independent interactions of the S100 protein family." Biochem J **396**(2): 201-214.

Schmidt, H. H., H. Hofmann, et al. (1996). "No .NO from NO synthase." Proc Natl Acad Sci U S A **93**(25): 14492-14497.

Shao, C., M. Folkard, et al. (2008). "Role of TGF-beta1 and nitric oxide in the bystander response of irradiated glioma cells." Oncogene **27**(4): 434-440.

Shao, C., K. M. Prise, et al. (2008). "Signaling factors for irradiated glioma cells induced bystander responses in fibroblasts." Mutat Res **638**(1-2): 139-145.

Shishido, S. N., A. Delahaye, et al. (2014). "The anticancer effect of PQ1 in the MMTV-PyVT mouse model." Int J Cancer **134**(6): 1474-1483.

Siddhanta, U., C. Wu, et al. (1996). "Heme iron reduction and catalysis by a nitric oxide synthase heterodimer containing one reductase and two oxygenase domains." J Biol Chem **271**(13): 7309-7312.

Simard, J. C., A. Cesaro, et al. (2013). "S100A8 and S100A9 induce cytokine expression and regulate the NLRP3 inflammasome via ROS-dependent activation of NF-kappaB(1.)." PLoS One **8**(8): e72138.

Simard, J. C., D. Girard, et al. (2010). "Induction of neutrophil degranulation by S100A9 via a MAPK-dependent mechanism." J Leukoc Biol **87**(5): 905-914.

Sinha, P., C. Okoro, et al. (2008). "Proinflammatory S100 proteins regulate the accumulation of myeloid-derived suppressor cells." J Immunol **181**(7): 4666-4675.

Sirnes, S., J. Bruun, et al. (2012). "Connexin43 acts as a colorectal cancer tumor suppressor and predicts disease outcome." Int J Cancer **131**(3): 570-581.

Snyder, C. M., E. H. Shroff, et al. (2009). "Nitric Oxide Induces Cell Death by Regulating Anti-Apoptotic BCL-2 Family Members." PLoS One **4**(9).

Song, S., F. F. Zhou, et al. (2013). "PDT-induced HSP70 externalization up-regulates NO production via TLR2 signal pathway in macrophages." Febs Letters **587**(2): 128-135.

Stuehr, D. J., N. S. Kwon, et al. (1991). "N omega-hydroxy-L-arginine is an intermediate in the biosynthesis of nitric oxide from L-arginine." J Biol Chem **266**(10): 6259-6263.

Teleki, I., T. Krenacs, et al. (2013). "The potential prognostic value of connexin 26 and 46 expression in neoadjuvant-treated breast cancer." BMC Cancer **13**: 50.

Thomsen, L. L., D. W. Miles, et al. (1995). "Nitric oxide synthase activity in human breast cancer." Br J Cancer **72**(1): 41-44.

Todryk, S., A. A. Melcher, et al. (1999). "Heat shock protein 70 induced during tumor cell killing induces Th1 cytokines and targets immature dendritic cell precursors to enhance antigen uptake." J Immunol **163**(3): 1398-1408.

Torok, N. J., H. Higuchi, et al. (2002). "Nitric oxide inhibits apoptosis downstream of cytochrome C release by nitrosylating caspase 9." Cancer Res **62**(6): 1648-1653.

Vacchelli, E., I. Vitale, et al. (2013). "Trial Watch: Anticancer radioimmunotherapy." Oncoimmunology **2**(9): e25595.

Verrico, A. K., A. K. Haylett, et al. (2001). "In vivo expression of the collagen-related heat shock protein HSP47, following hyperthermia or photodynamic therapy." Lasers Med Sci **16**(3): 192-198.

Vinken, M., T. Vanhaecke, et al. (2006). "Connexins and their channels in cell growth and cell death." Cell Signal **18**(5): 592-600.

Wang, J., Y. Dai, et al. (2013). "All-trans retinoic acid restores gap junctional intercellular communication between oral cancer cells with upregulation of Cx32 and Cx43 expressions in vitro." Med Oral Patol Oral Cir Bucal **18**(4): e569-577.

Wang, Y., W. S. Shin, et al. (1996). "Contribution of sustained Ca2+ elevation for nitric oxide production in endothelial cells and subsequent modulation of Ca2+ transient in vascular smooth muscle cells in coculture." J Biol Chem **271**(10): 5647-5655.

Weigert, A. and B. Brune (2008). "Nitric oxide, apoptosis and macrophage polarization during tumor progression." Nitric Oxide **19**(2): 95-102.

Wu, J., R. N. Taylor, et al. (2013). "Retinoic acid regulates gap junction intercellular communication in human endometrial stromal cells through modulation of the phosphorylation status of connexin 43." J Cell Physiol **228**(4): 903-910.

Yang, Y., S. K. Qin, et al. (2014). "Connexin-dependent gap junction enhancement is involved in the synergistic effect of sorafenib and all-trans retinoic acid on HCC growth inhibition." Oncol Rep **31**(2): 540-550.

Yokota, T., H. Ikeda, et al. (2000). "Enhanced cell death in NR-S1 tumor by photodynamic therapy: possible involvement of Fas and Fas ligand system." Lasers Surg Med **26**(5): 449-460.

Yu, C. F., J. H. Hong, et al. (2013). "The Roles of Macrophages and Nitric Oxide in Interleukin-3-Enhanced HSV-Sr39tk-Mediated Prodrug Therapy." PLoS One **8**(2).

Zhang, W., X. J. He, et al. (2011). "Inducible nitric oxide synthase expression correlates with angiogenesis, lymphangiogenesis, and poor prognosis in gastric cancer patients." Hum Pathol **42**(9): 1275-1282.

Zitvogel, L., O. Kepp, et al. (2012). "Inflammasomes in carcinogenesis and anticancer immune responses." Nat Immunol **13**(4): 343-351.

Publications

Sonda N, Simonato F, Peranzoni E, Calì B, Bortoluzzi S, Bisognin A, Wang E, Marincola FM, Naldini L, Gentner B, Trautwein C, Sackett SD, Zanovello P, Molon B, Bronte V (2013). **miR-142-3p prevents macrophage differentiation during cancer-induced myelopoiesis.** Immunity 38:1236-49.

Rodriguez L, Simeonato E, Scimemi P, Anselmi F, Calì B, Crispino G, Ciubotaru CD, Bortolozzi M, Ramirez FG, Majumder P, Arslan E, De Camilli P, Pozzan T, Mammano F (2012). **Reduced phosphatidylinositol 4,5-bisphosphate synthesis impairs inner ear Ca2+ signaling and high-frequency hearing acquisition**. Proc. Natl. Acad. Sci. U.S.A. 109:14013-8.

Immunity
Article

miR-142-3p Prevents Macrophage Differentiation during Cancer-Induced Myelopoiesis

Nada Sonda,[1,2] Francesca Simonato,[1] Elisa Peranzoni,[2] Bianca Calì,[1] Stefania Bortoluzzi,[4] Andrea Bisognin,[4] Ena Wang,[5] Francesco M. Marincola,[5,6] Luigi Naldini,[7,8] Bernhard Gentner,[7,8] Christian Trautwein,[9] Sara Dutton Sackett,[9] Paola Zanovello,[1,2] Barbara Molon,[2,3] and Vincenzo Bronte[10,*]

[1]Department of Surgery, Oncology and Gastroenterology, Oncology and Immunology Section, University of Padua, 35128 Padua, Italy
[2]Istituto Oncologico Veneto, Istituti di Ricovero e Cura a Carattere Scientifico (IRCCS), 35128 Padua, Italy
[3]Venetian Institute of Molecular Medicine, 35129 Padua, Italy
[4]Department of Biology, University of Padua, 35121 Padua, Italy
[5]Department of Transfusion Medicine, Infectious Disease and Immunogenetics Section, Clinical Center, and Center for Human Immunology, National Institutes of Health, Bethesda, MD 20892, USA
[6]Chief Research Officer, Sidra Medical and Research Center, Doha, Qatar
[7]San Raffaele Telethon Institute for Gene Therapy and Division of Regenerative Medicine, Gene Therapy and Stem Cells, San Raffaele Scientific Institute, 20132 Milan, Italy
[8]Vita-Salute San Raffaele University Medical School, 20132 Milan, Italy
[9]Department of Medicine III, RWTH University Hospital, 52074 Aachen, Germany
[10]Verona University Hospital and Department of Pathology, Immunology Section, University of Verona, 37134 Verona, Italy
*Correspondence: vincenzo.bronte@univr.it
http://dx.doi.org/10.1016/j.immuni.2013.06.004

SUMMARY

Tumor progression is accompanied by an altered myelopoiesis causing the accumulation of immunosuppressive cells. Here, we showed that miR-142-3p downregulation promoted macrophage differentiation and determined the acquisition of their immunosuppressive function in tumor. Tumor-released cytokines signaling through gp130, the common subunit of the interleukin-6 cytokine receptor family, induced the LAP* isoform of C/EBPβ transcription factor, promoting macrophage generation. miR-142-3p downregulated gp130 by canonical binding to its messenger RNA (mRNA) 3' UTR and repressed C/EBPβ LAP* by noncanonical binding to its 5' mRNA coding sequence. Enforced miR expression impaired macrophage differentiation both in vitro and in vivo. Mice constitutively expressing miR-142-3p in the bone marrow showed a marked increase in survival following immunotherapy with tumor-specific T lymphocytes. By modulating a specific miR in bone marrow precursors, we thus demonstrated the feasibility of altering tumor-induced macrophage differentiation as a potent tool to improve the efficacy of cancer immunotherapy.

INTRODUCTION

Under pathological conditions, such as infections or cancer development, a hematopoiesis subversion occurs, which leads to the expansion of myeloid cells retaining an immature phenotype and sharing a propensity to inhibit T lymphocyte activation (Gabrilovich et al., 2012). Mouse myeloid cells systemically expanded in tumor-bearing hosts express the markers CD11b and Gr-1 (Ly-6C and Ly-6G) and have been defined collectively as myeloid-derived suppressor cells (MDSCs). $CD11b^+Gr\text{-}1^+$ cells do not possess a suppressive phenotype, which is instead acquired in cancer hosts when they accumulate in the spleen and within the tumor mass of tumor-bearing mice (Gallina et al., 2006; Sica and Bronte, 2007). In addition to their immunoregulatory activity, $CD11b^+Gr\text{-}1^+$ cells have been found to promote tumor angiogenesis, cell invasion, and metastasis (Gil-Bernabé et al., 2012).

It is increasingly clear that $CD11b^+Gr\text{-}1^+$ cells comprise different subsets. Granulocytic MDSCs, with high Gr-1 expression, are less immunosuppressive than monocytic- and macrophagic-like MDSCs, which possess an intermediate and low or negative Gr-1 expression, respectively (Dolcetti et al., 2010).

Experimental models of autochthonous pancreatic ductal adenocarcinoma (PDAC) formation in mouse have detailed progressive waves of myelomonocytic cell recruitment after initiation of the transforming program driven by the active oncogenes *Kras*, with $CD11b^+Gr\text{-}1^+$ cells being among the first to be recruited within the developing cancer lesions (Clark et al., 2007). Moreover, recent data suggest that *Kras* oncogene-dependent accrual of myelomonocytic cells is mandatory for pancreatic intraepithelial neoplasia (PanIN) initiation and progression. This process involves at least two cytokines, GM-CSF and interleukin-6 (IL-6), which were shown to be sufficient to originate immunosuppressive $CD11b^+Gr\text{-}1^+$ cells from bone marrow (BM) precursors (Marigo et al., 2010).

In addition, *Kras* oncogene-driven inflammation at the PanIN stage critically relied on GM-CSF for both progression to PDAC and $CD11b^+Gr\text{-}1^+$ cell recruitment within the pancreatic stroma. Moreover, this circuit was essential to alter $CD8^+$ cytotoxic T cell immunity, and only the blockade of either GM-CSF

production or CD11b$^+$Gr-1$^+$ cell activity restored antitumor immunity (Bayne et al., 2012; Pylayeva-Gupta et al., 2012).

Interestingly, recruited CD11b$^+$Gr-1$^+$ cells contribute with transformed epithelial cells to the local production of the cytokines IL-6 and IL-11 that activate the signal transducer and activator of transcription factor 3 (STAT3). STAT3, in turn, induces antiapoptotic and proproliferative genes, fueling tumor initiation, promotion, and progression (Fukuda et al., 2011; Lesina et al., 2011).

Recent studies have also unveiled a role for some transcription factors (TFs) in regulating the myelomonocytic differentiation and recruitment to either tumor site or secondary lymphoid organs (Sonda et al., 2011). In particular, the STAT family members STAT1 (Kusmartsev and Gabrilovich, 2005), STAT3 (Corzo et al., 2009), and STAT6 (Munera et al., 2010) have been reported as positive regulators of MDSC expansion and activation. In addition, CCAAT/enhancer-binding protein β (C/EBPβ) regulates MDSC functional properties and subset distribution in different organs (Marigo et al., 2010). Of note, STAT3 can directly influence C/EBPβ activity (Zhang et al., 2010), adding another level of complexity to the scenario of tumor-enhanced myelopoiesis.

In addition to TFs, an aberrant microRNA (miR) expression can also be associated with tumor-induced myelopoiesis (Liu et al., 2011, 2012 ; Zhang et al., 2011). MiRs are small noncoding RNAs regulating gene expression primarily through seed-matched sites located within the 3′ untranslated regions (UTR) of the target mRNA (Bartel, 2009). However, miRs can also recognize sites in the 5'UTR or in the coding sequence of the cognate mRNA, even if these bindings seem to be less effective than those in the canonical 3' UTRs (Fang and Rajewsky, 2011; Tay et al., 2008).

Many biological processes, such as embryonic development, cell differentiation, and division are influenced by the dynamically modulated expression of specific miRs (Hatfield et al., 2005; Miska, 2005). Hematopoiesis represents a finely tuned, multistep process where miRs can exert a fundamental regulator role (Baltimore et al., 2008; Chen et al., 2004; Chen and Lodish, 2005). For example, miR-17-5p, miR-20a, miR-106a, miR-150, miR-10a, and miR-146a have been reported to regulate the physiological differentiation of monocytes, B and T lymphocytes, helper T cells, and dendritic cells (DCs), respectively (Fontana et al., 2007; Takahashi et al., 2012 ; Turner et al., 2011 ; Zhou et al., 2007).

Despite the increasing amount of data on the subject, the molecular mechanisms explaining how neoplastic cells regulate the expression and the activity of specific TFs and/or miRs in myeloid compartment are still poorly defined. Furthermore, reciprocal interaction between miRs and TFs and specific pathways controlling either granulocytic or monocytic differentiation have not been fully elucidated. Here, we determined the "miR signature" in tumor-infiltrating myeloid cells (TIMs). Among differentially expressed miRs, we identified miR-142-3p as critical for preventing macrophage differentiation during tumor-induced myelopoiesis, by both canonical and non canonical modulation of the gp130 and C/EBPβ signalling. Moreover, we demonstrated the potential therapeutic application for miR-142-3p oligonucleotide as adjuvant tool for adoptive T cell therapy of cancer.

RESULTS

miR-142-3p Is Downregulated in Tumor-Associated CD11b$^+$ Cells

To identify differentially expressed miRs (DEMs) in TIMs, total RNA was isolated from either tumor-infiltrating or normal CD11b$^+$ cells purified from the spleen of healthy mice and was hybridized on to miR arrays (see Figure S1A available online). Clustering analysis of samples, based on all considered miR expression profiles, showed that myeloid cells isolated from tumor-bearing mice had a distinctive miR signature compared to control healthy spleens (Figure 1A). Among the miR repertoire, 79 were found to be differentially modulated in tumor-infiltrating versus normal cells (Figure S1B). In particular, the array analysis showed miR-142-3p and miR-150 were strongly downregulated in tumor-infiltrating CD11b$^+$ cells. This finding was further confirmed by qRT-PCR analysis (Figure S1C).

In order to identify the putative targets of the 79 DEMs, we performed a combined analysis of miR and gene expression profiles of the same samples. As supported by expression data, 238 negative correlations, mainly involving downregulated miRs, were selected (Figure S1D). Many of the predicted target genes are known regulatory factors of myeloid cell differentiation and/or proliferation (Figures S1E and S1F). For example, *Nras* alteration was linked to an aberrant GM-CSF signaling, causing a chronic myelomonocytic leukemia-like phenotype (Wang et al., 2010). *Ptgs2* was associated with myeloid cell recruitment and/or activity during tumor development (Eruslanov et al., 2010), whereas *E2f3* was identified as a TF involved in monocyte differentiation (Schmeier et al., 2009). In addition, both *Dapk1* and *Ccne1* expression could be regulated by C/EBPβ (Gade et al., 2008; Gutsch et al., 2011), which modulates tumor-induced myelopoiesis (Marigo et al., 2010). We thus moved to investigate the role of miR-142-3p and miR-150 in TIM differentiation and activity during altered myelopoiesis.

miR-142-3p Directs Myeloid Cell-Commitment

In order to assess the role of miR-142-3p and miR-150 in myeloid cell commitment, we first generated MDSCs in vitro from bone marrow cultures, as previously described (Marigo et al., 2010). Specific miR content was measured every day by qRT-PCR analysis. These two miRs followed very different kinetics (Figure 1B): miR-142-3p showed a prominent downregulation in the early phases of cell commitment, whereas miR-150 had a linear, but delayed, decrease over time. This time-dependent miR modulation was differently associated with BM-MDSC generation. The enforced expression of miR-142-3p in BM cultures determined a significant decrease of total cell numbers (data not shown), exerting different effects on various cell subsets. In fact, the expression of miR-142-3p, but not miR-150, in BM cells mostly impaired CD11b$^+$Gr-1$^{lo\text{-}neg}$ cell subset generation (Figure 1C). The morphological analysis showed that miR-142-3p overexpressing BM-cultures were mainly driven towards granulocytic differentiation (Figure 1D).

Cytofluorimetric characterization and qRT-PCR analysis confirmed that the CD11b$^+$Gr-1$^{lo\text{-}neg}$ subset was mainly composed of mature macrophages with enhanced expression of markers (Figure S1G), and genes (Figure S1H), distinct from M2-oriented, tumor-associated macrophages (Gabrilovich

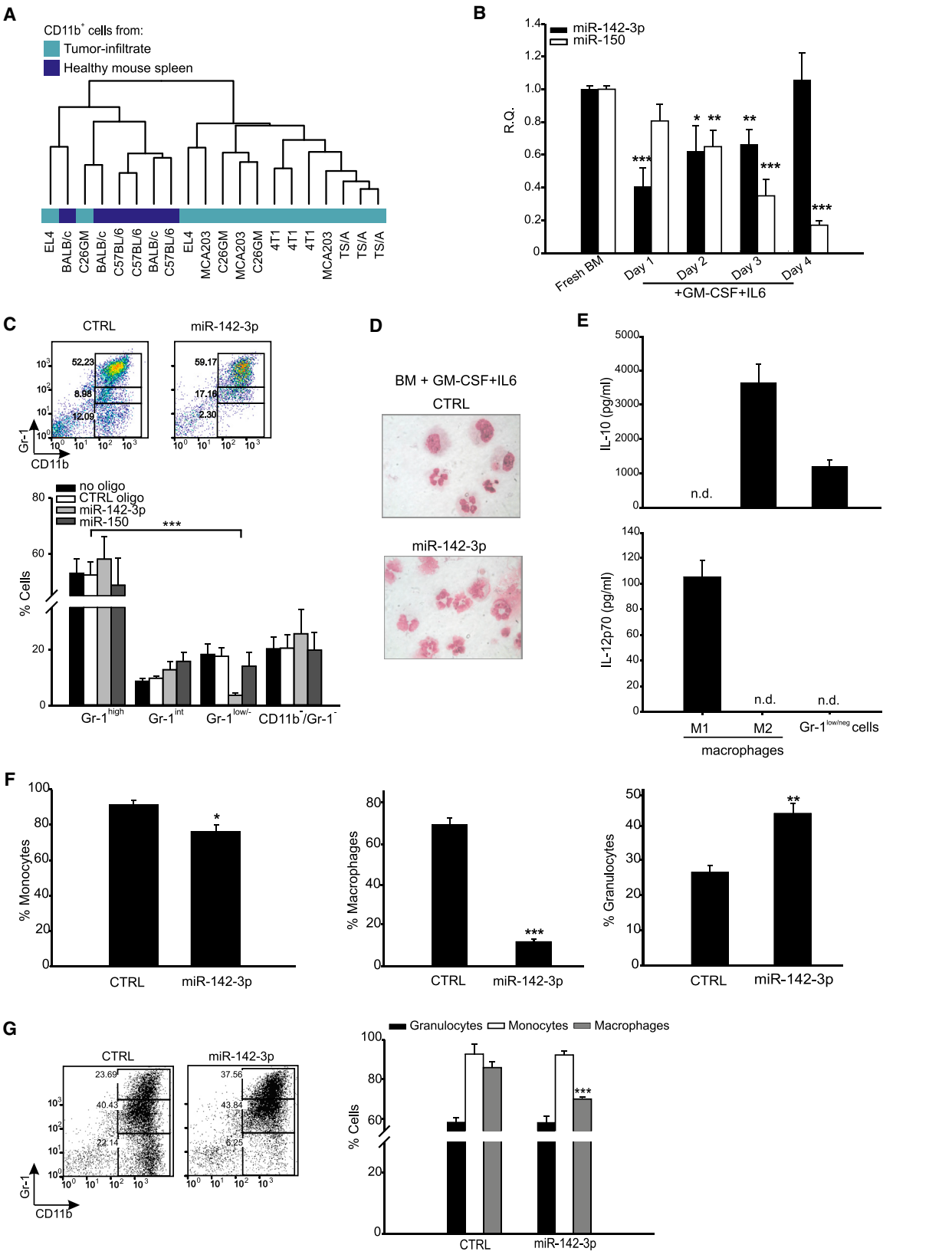

(legend on next page)

et al., 2012; Lawrence and Natoli, 2011; Mantovani et al., 2002). In addition, purified CD11b^{+}Gr-1$^{lo\text{-}neg}$ cells secreted IL-10 but not IL-12, analogously to M2-polarized macrophages (Figure 1E). Gene-expression analysis of miR-142-3p overexpressing BM cultures showed that miR upregulation mostly affected genes related to M2 polarization (Figure S1I). Collectively, these data indicated that CD11b^{+}Gr-1$^{lo\text{-}neg}$ cells possessed a prevalent M2-profile, even if the expression of M1-macrophage markers, such as MARCO and *Nos2* (Murray and Wynn, 2011), was also detected (Figure S1G and S1H).

To characterize further miR role in myeloid cell-commitment, we additionally stimulated BM-MDSCs expressing either control (CTRL) or miR-142-3p oligos with M-CSF. miR-142-3p overexpressing cells showed a clear reduction in macrophage percentage and a significant increase in the granulocytes, whereas the monocytic subset was only partially affected (Figure 1F; Figure S1L). Collectively, these data suggest that miR-142-3p content in BM cells regulates the transition to macrophages. Of note, miR-142-3p-expressing BM-cells exposed to tumor-cell conditioned medium (TCCM) showed a comparable impairment in macrophage differentiation (Figure 1G).

miR-142-3p Downregulation Is Required for the Generation and Activity of Immunosuppressive Cells

Among in vitro generated BM-MDSCs, the CD11b^{+}Gr-1$^{lo\text{-}neg}$ subset is endowed with the highest immune-suppressive activity (Dolcetti et al., 2010; Marigo et al., 2010). We thus wondered whether miR-142-3p expression could control the suppressive behavior of BM-MDSC cultures. We measured cell division in antigen-stimulated, CFDA-SE-labeled T lymphocytes cultured with BM-MDSCs previously transfected with either CTRL or miR oligos. The enhanced expression of miR-142-3p, but not miR-150, reduced the immunosuppressive activity of BM-MDSCs, restoring CD8^{+} T cell proliferation (Figure 2A). A similar decrease in the immunosuppressive activity was observed in miR-142-3p-expressing MDSCs generated by the exposure to TCCM (Figure S2).

We therefore asked whether forced miR downregulation in myeloid progenitors could support macrophage generation even in the presence of granulocytic differentiating stimuli. We isolated BM-CD11b^{-} cells, which are capable of generating all the Gr-1 subsets after cytokine treatment (Figure 2B). We infected these cells with a lentiviral construct (miR-142-3pT) able to "sponge" endogenous miR-142-3p (the infection efficiency was of 38% ± 5%). After infection, CD11b^{-} cells were treated with G-CSF to drive granulocytic differentiation. miR-142-3p downregulation determined a significant decrease in the percentage of granulocytes with a concomitant increase in the macrophage number. The differentiation of monocytes was not affected (Figure 2C).

When cultured with antigen-activated CD8^{+} T cells, G-CSF-treated CD11b^{-} cells showed a poor immunosuppressive activity (Figure 2D). Of note, the enforced miR-142-3p downregulation augmented the ability of G-CSF-treated CD11b^{-} to block T lymphocyte proliferation (Figure 2D). Thus, miR-142-3p downregulation in myeloid precursors represents a pivotal event for the maturation of immunosuppressive macrophages.

IL6st Is a Direct Target of miR-142-3p, and It Is Involved in Macrophage Commitment

In order to define the molecular mechanisms by which miR-142-3p controls macrophage differentiation, we computationally identified regulated genes, focusing on those involved in monocyte-macrophage commitment. To evaluate whether miR directly binds to these predicted targets, we set up a luciferase reporter assay screening by using plasmids in which the firefly luciferase open reading frame (ORF) was fused to the 3' UTR of these genes. miR-142-3p overexpression caused a reduction in luciferase activity when transfected with the *Il6st*, *Egr2*, *Id1*, and *Pla2g6* coding plasmids, indicating these genes as direct miR targets (Figure 3A). Mutations in the predicted seed sequence allowed us to validate miR-142-3p interaction with the two genes showing the strongest impairment of luciferase activity, i.e., *Il6st* and *Egr2.* In seed-mutated mRNAs, miR-142-3p addition did not change luciferase activity (Figure 3B).

Between these two targets, we focused on *Il6st* gene, the transmembrane chain common to all the receptors for IL-6 cytokine family members, because the activation of IL-6 pathway is known to regulate physiological and pathological myeloid cell differentiation. To verify gp130 role on tumor-altered myelopoiesis, we injected MCA203 cells either in wild-type (WT) or in mice bearing a conditional *Il6st* gene deletion in hematopoietic cells (*Il6st*$^{-/-}$). After 4 weeks, BM cells were harvested and cultured in the presence of TCCM to evaluate myeloid cell differentiation. BM cells from *Il6st*$^{-/-}$ mice showed a clear reduction in the percentage of the macrophages, associated to an expansion of both the granulocytic and monocytic compartment (Figure 3C).

Intriguingly, miR overexpression induced a strong reduction in the phosphorylated STAT3 protein level (Figure 3D), indicating that miR-142-3p also influenced STAT3 activation, an event downstream of the IL6st signaling.

Figure 1. miR-142-3p Is Downregulated in Tumor-Recruited CD11b^{+} Cells and Regulates Myeloid Cell Differentiation

(A) The dendrogram shows samples classification resulting from unsupervised analysis of all miR expression data obtained from CD11b^{+} total RNA isolated from either the spleen of healthy mice (navy) or from the mass of the indicated tumors (blue). Data from three arrays hybridized with pools of at least three mice per each group are shown.

(B) BM cells were cultured with GM-CSF+IL-6 to generate BM-MDSCs. Total RNA was isolated from either fresh or cultured BM-cells (days 1–4) and qRT-PCR for miR-142-3p and miR-150 content was performed. Data, reported as relative quantity (R.Q.), are normalized to miR level in fresh BM cells.

(C and D) BM cells from healthy mice were transfected with either CTRL (scramble) or miR oligo before GM-CSF+IL-6 treatment. After 96 hours, cultures were analyzed by flow cytometry and cytochemical stain to evaluate myeloid differentiation. Representative FACS panels and the relative quantification of subsets expressing CD11b and Gr-1 markers (C) are reported, and May-Grünwald-Giemsa staining of cytospins is shown (D).

(E) CD11b^{+}/Gr-1$^{lo/neg}$ cells were sorted from GM-CSF+IL-6 treated-BM cells and plated for additional 40 hours. IL-10 and IL-12p70 release was measured by ELISA. For comparison, cytokine levels secreted by either M1- or M2-polarized, BM-derived macrophages are shown.

(F) Percentages of monocytes, macrophages, and granulocytes in BM cultures further stimulated with M-CSF.

(G) BM cells were transfected with either CTRL or miR oligo and cultured in the presence of TCCM. After 96 hours, cultures were analyzed by FACS.

In all panels, data are expressed as mean ± SE of three independent experiments. $^{**}p < 0.01$; $^{***}p < 0.001$. See also Figure S1.

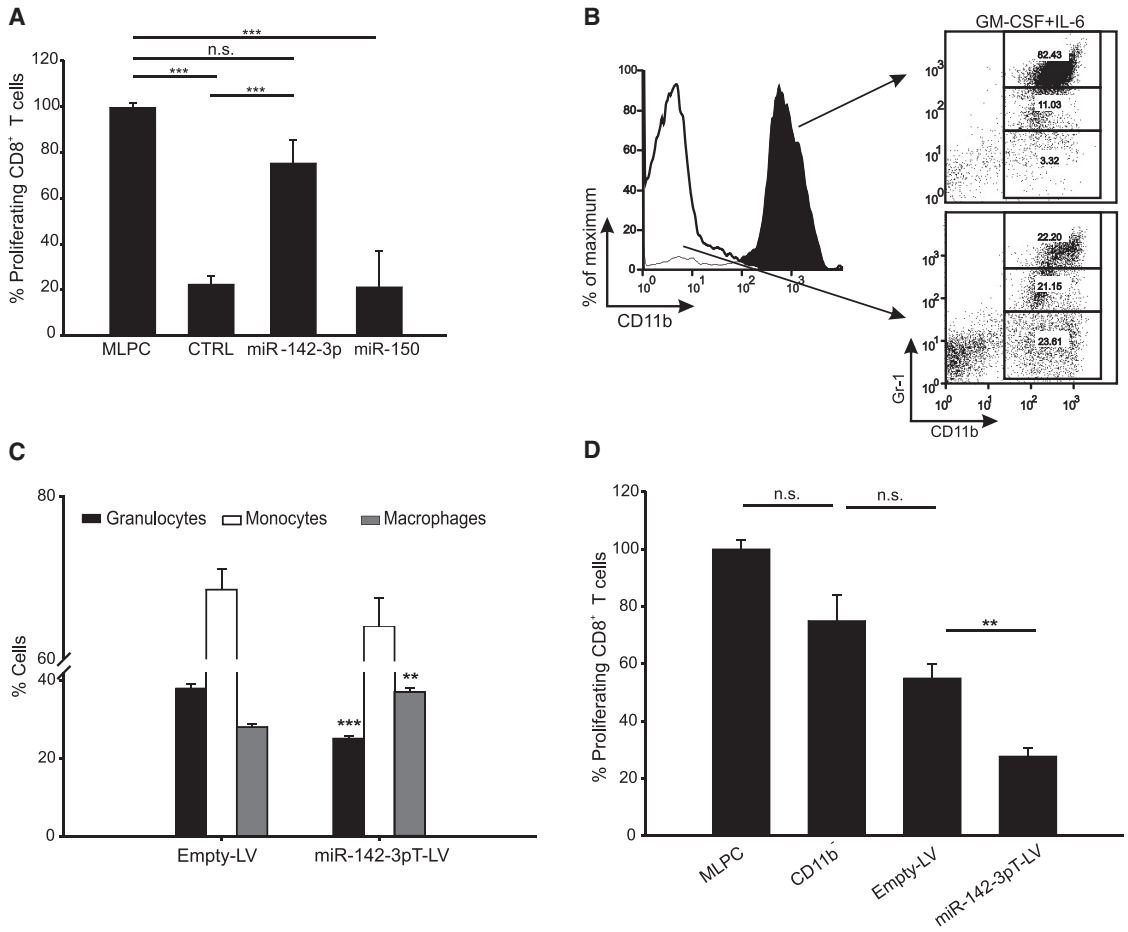

Figure 2. miR-142-3p Regulates Immune-Suppressive Activity of TIMs

(A) CFDA-SE-labeled $CD8^+$ T cells from *pmel-1* mice were stimulated with the specific antigen in the presence of BM-MDSCs expressing either CTRL or miR oligos. $CD8^+$ T cell proliferation was evaluated as CFDA-SE dilution relative to lymphocyte cultures stimulated in the absence of BM-MDSCs (MLPC).

(B) BM $CD11b^+$ and $CD11b^-$ cells of healthy mice were treated for 4 days with GM-CSF+IL6 before evaluating CD11b/Gr-1 distribution.

(C) BM-$CD11b^-$ cells were infected with either CTRL or miR-142-3p capturing (miR-142-3pT) lentiviruses and then cultured in the presence of G-CSF. Percentages of granulocytes, monocytes, and macrophages are reported.

(D) $CD8^+$ T lymphocytes were antigen-stimulated and cultured for 3 days in the presence of $CD11b^-$ BM cells generated as in (B) and (C). Histograms represent the quantification of $CD8^+$ T cell-proliferation evaluated as CFDA-SE dilution relative to control MLPC.

In all panels, data are expressed as mean ± SE from three independent experiments. *$p < 0.05$;**$p < 0.01$; ***$p < 0.001$. See also Figure S2.

LAP* C/EBPβ Expression Is Controlled by miR-142-3p

A reported link exists between *Stat3* and *Cebpb* (Zhang et al., 2010), which regulates the differentiation of immunosuppressive TIMs (Marigo et al., 2010). We therefore tested whether *Cebpb* could be controlled by miR-142-3p. *Cebpb* mRNA encodes three isoforms, with different molecular weight and transcription activity: two activating proteins, LAP* and LAP, and an inhibitory isoform, LIP. We evaluated C/EBPβ isoform amounts in miR overexpressing NIH-3T3 cells, and we observed a significant downregulation exclusively in LAP* (Figure 4A).

During cell differentiation, the activating/inhibitory isoform ratio dynamically changes to guarantee a specific gene-transcription pattern (Smink et al., 2009). We detected a significant variation in isoform ratio, mainly due to downregulation of the LAP*, in miR-142-3p overexpressing BM-MDSCs (Figure 4B). Intriguingly, BM cells driven to granulocytic differentiation treatment showed a strong decrease in LAP* content, whereas macrophage differentiation caused LAP* upregulation (Figure 4C).

To determine whether C/EBPβ isoform ratio was altered by miR-142-3p through STAT3 activity modulation, we treated BM cells with GM-CSF and IL-6 in the presence of JSI-124, a specific STAT-3 phosphorylation inhibitor. As previously reported (Nefedova et al., 2005), the addition of the inhibitor promoted a strong DC maturation and a reduction in the macrophage number (Figure S3). JSI-124-treated BM cells showed a strong LAP* decrease (Figure 4D), an overall response similar to miR-142-3p enforced expression (Figure 4B), suggesting a direct link between STAT3 activation and C/EBPβ isoform-ratio modulation.

We additionally ablated gp130 expression in NIH-3T3 cells by small hairpin RNA (shRNA) (Figure 4E). In the absence of gp130, we found a significant decrease of both LAP* and LIP expression (Figure 4F), suggesting that, in addition to gp130 modulation,

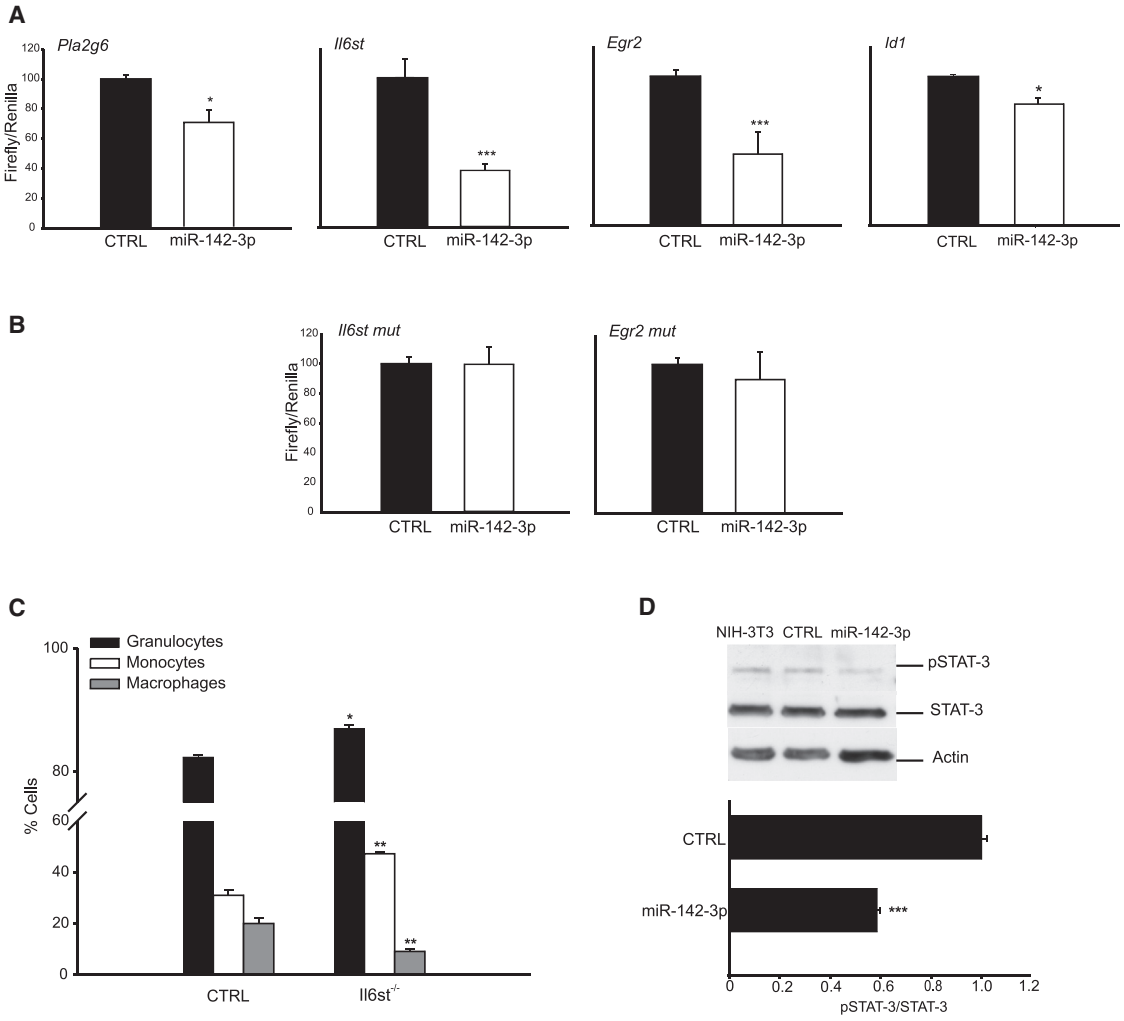

Figure 3. A Direct Target of miR-142-3p, IL6st, Is Involved in Macrophage Commitment

(A and B) HEK293T cells were cotransfected with a plasmid carrying the luciferase ORF fused to WT 3'UTR of the indicated genes and with either CTRL or miR-142-3p oligos (A). Experiments were additionally performed with a plasmid mutated in the seed sequence of 3'UTR (B). The firefly activity was normalized to the *Renilla* activity and the normalized value of CTRL-transfected cells was set as 100.

(C) WT (CTRL) or *Il6st*$^{-/-}$ mice were injected with MCA203 cells. After 4 weeks, BM cells were harvested and further cultured with TCCM. Cultures were analyzed by flow cytometry. Percentages of granulocytes, monocytes, and macrophages are reported. Data from n= 6 mice per group (from two independent experiments).

(D) Immunoblot analysis (WB) of STAT3 phosphorylation in miR-142-3p-over-expressing NIH-3T3 cells and the related signal quantification (ratio between phosphorylated STAT3 (pSTAT3)/nonphosphorylated STAT3). Protein levels were normalized to α-actin signal. The normalized STAT3 ratio in CTRL-transfected cells was set as 1.

In all panels, data are expressed as mean ± SE from three (or five for luciferase assays) independent experiments. *p <0.05;**p < 0.01; ***p < 0.001.

miR-142-3p could control C/EBPβ expression by other mechanisms.

miR-142-3p Directly Regulates the C/EBPβ Isoform Ratio and Is Negatively Regulated by LAP*

We detected a significant LAP* downregulation even in HEK293T cells coexpressing miR-142-3p and *Cebpb* coding sequence domain (CDS) (Figure 5A). By using RNAHybrid 2.2 algorithm, a putative miR-142-3p binding site was identified in the *Cebpb* CDS (Figure 5B). Of note, this binding site spans the second start codon, where a loop structure can be created, regulating the reciprocal isoform expression (Baldwin et al., 2004). We speculated that miR binding, by either modifying or interfering with the loop generation, could control C/EBPβ isoform translation (Figure 5B).

To validate the hypothesis of a direct miR binding, we transfected HEK293T cells with a plasmid carrying the *Cebpb* CDS in frame with the luciferase ORF. The addition of miR-142-3p significantly reduced the luciferase activity (Figure S4A). Coherently, miR overexpression did not impact the luciferase activity in cells expressing a mutated CDS (Figure S4A). Results were validated by protein blot analysis (compare Figures 5A and 5C). These data unveiled a direct miR-142-3p-*Cebpb* interaction.

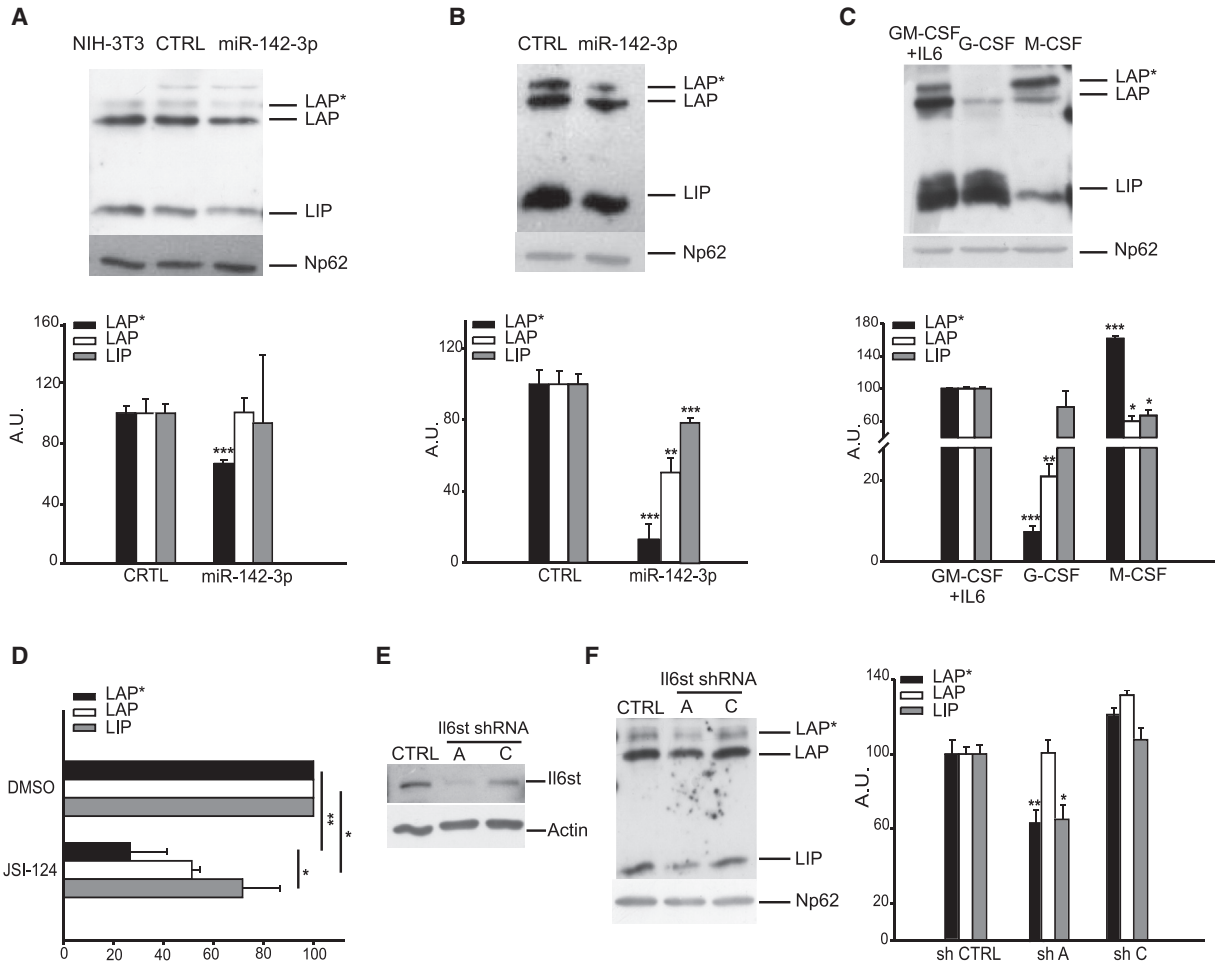

Figure 4. LAP* C/EBPβ Expression Is Controlled by miR-142-3p

(A and B) WB of C/EBPβ isoform expression in the nuclear fraction (NF) of NIH-3T3 cells (A) or BM-MDSCs (B) expressing either CTRL or miR-142-3p oligo and the related signal quantification were reported. Protein levels were normalized to nucleoporin-62 (Np62) signal. The normalized C/EBPβ value in CTRL-transfected cells was set as 100. A.U., arbitrary units.

(C) WB of C/EBPβ isoform expression in the NF of BM-cells cultured for 96 hours in the presence of different cytokines (GM-CSF/IL-6, G-CSF or M-CSF) and the related signal quantification were reported.

(D) BM cells were treated for 4 days with GM-CSF+IL-6 and 0.5 μM JSI-124 or DMSO vehicle were added 24 hours before culture harvesting. C/EBPβ expression was analyzed by WB.

(E) *Il6st* was ablated in NIH-3T3 cells by transfecting different shRNAs expressing puromycin resistance. After 4 weeks of antibiotic selection, IL-6 expression was analyzed in whole-cell extract by WB. Silencing efficiency: sh A = 85% sh C = 10%.

(F) WB for C/EBPβ isoform expression in the NF of *Il6st*-silenced NIH-3T3 cells and the relative signal quantification were reported.

In all panels, data are expressed as mean ± SE of three independent experiments. *p < 0.05 **p < 0.01 ***p < 0.001. See also Figure S3.

A TF-miR feedback loop is frequently reported, thus we asked whether C/EBPβ could in turn regulate miR-142-3p expression. A plasmid coding a region of 1,250 bp upstream of the pri-miR-142-3p sequence (named Walk 1) fused to the luciferase ORF was generated. This region contains the miR promoter and nine computationally identified C/EBPβ binding sites. In addition, two shorter constructs (Walk 2 and Walk 3; Figure S4B) were considered. Moreover, to further dissect the role of each isoform in miR regulation, *Cebpb* sequence was modified to generate a LAP*-coding construct (Figures S4C and S4D). No miR-142-3p promoter activation was observed when cells were cotransfected with miR promoter plasmids and LAP* coding construct (Figure 5D). On the other hand, a clear increment in luciferase activity was detected by transfecting cells with a LIP-coding plasmid. The reduction in miR promoter activity linearly correlated with the binding site number (Figure 5D).

To evaluate the impact of C/EBPβ isoform ratio on miR promoter activity, we cotransfected HEK293T with different concentrations of LAP*- and LIP-coding plasmids. We found that an increased ratio caused a linear promoter activity reduction (Figure 5E), whereas a higher promoter activity was observed when the ratio decreased (Figure 5F).

In summary, we hypothesize that during tumor-induced myelopoiesis a mini-circuit is activated by tumor-released IL-6 family cytokines. Their binding to the IL-6 subunit determines both a STAT3-mediated and a direct C/EBPβ isoform ratio

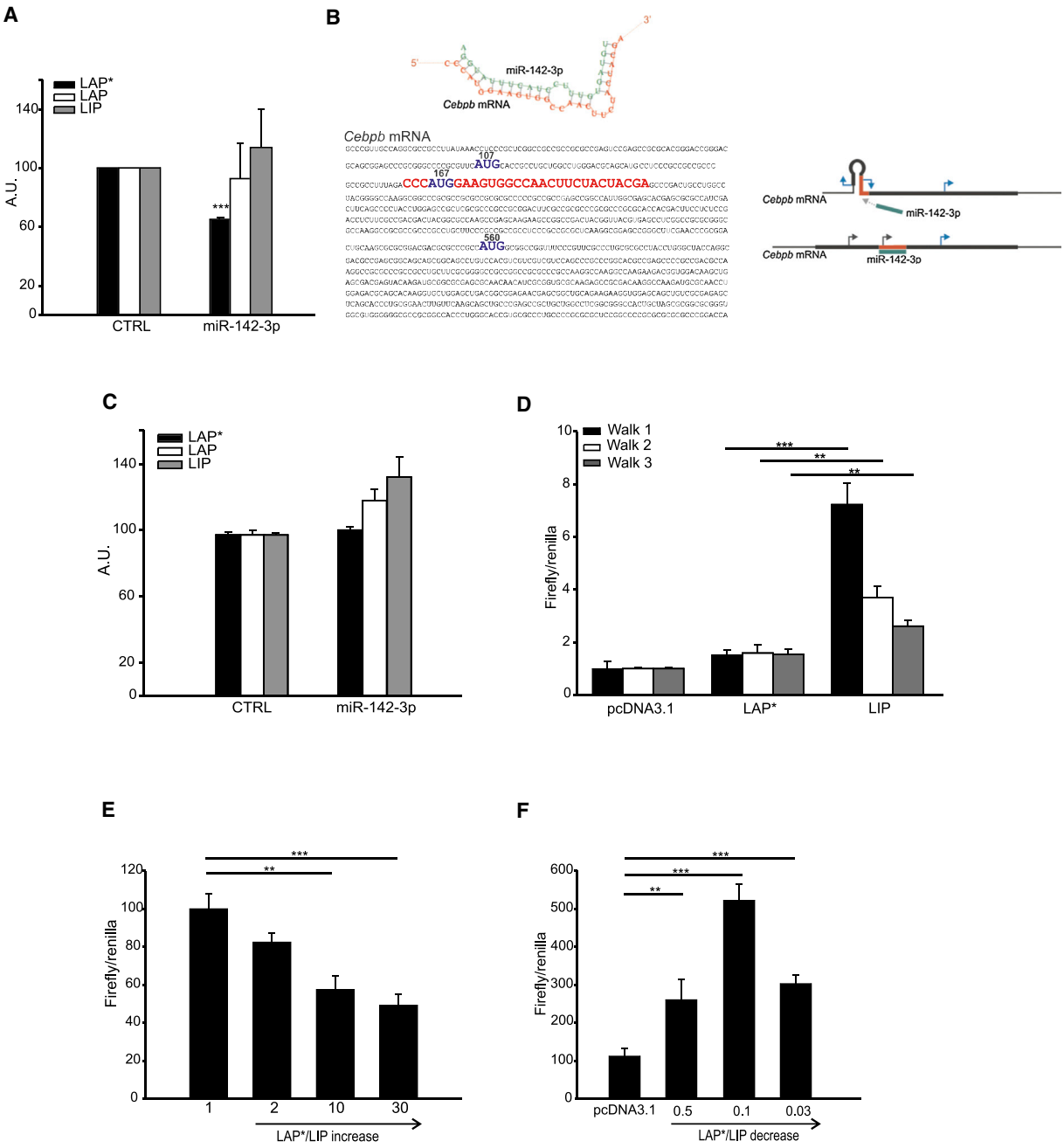

Figure 5. miR-142-3p Directly Regulates the C/EBPβ Isoform Ratio and Is Negatively Regulated by LAP*

(A) Signal quantification of C/EBPβ isoform expression by WB in the NF of HEK293T cells transfected with mouse C/EBPβ CDS and either CTRL or miR-142-3p oligo.

(B) Computationally predicted miR-142-3p binding site in the C/EBPβ CDS (left) and the hypothesized impact of miR binding on AUG recognition (right). Blue/grey arrow = active/not active start codons, respectively.

(C) Signal quantification of C/EBPβ expression by WB in HEK293T cells transfected with a plasmid coding a mutated C/EBPβ CDS and with either CTRL or miR-142-3p oligos.

(D) Luciferase assay in HEK293T cells transfected with constructs expressing three putative miR-142-3p promoter sequences (Walk 1, 2, and 3), and plasmids expressing either the LIP or the LAP* isoforms. Luciferase activity was normalized to the *Renilla* luciferase activity and the normalized value of pcDNA3.1-trasfected cells was set as 1.

(E and F) HEK293T cells were transfected with the Walk 1 plasmid and constructs expressing either the LIP and the LAP* isoforms in different ratios. Luciferase activity was normalized to the *Renilla* luciferase activity and the normalized value of LAP*/LIP-transfected cells (LAP*/LIP ratio = 1) (E) or pcDNA3.1-trasfected cells (F) was set as 100.

In all panels, data are expressed as mean ± SE of four independent experiments. *p < 0.05; **p < 0.01; ***p < 0.001. See also Figure S4.

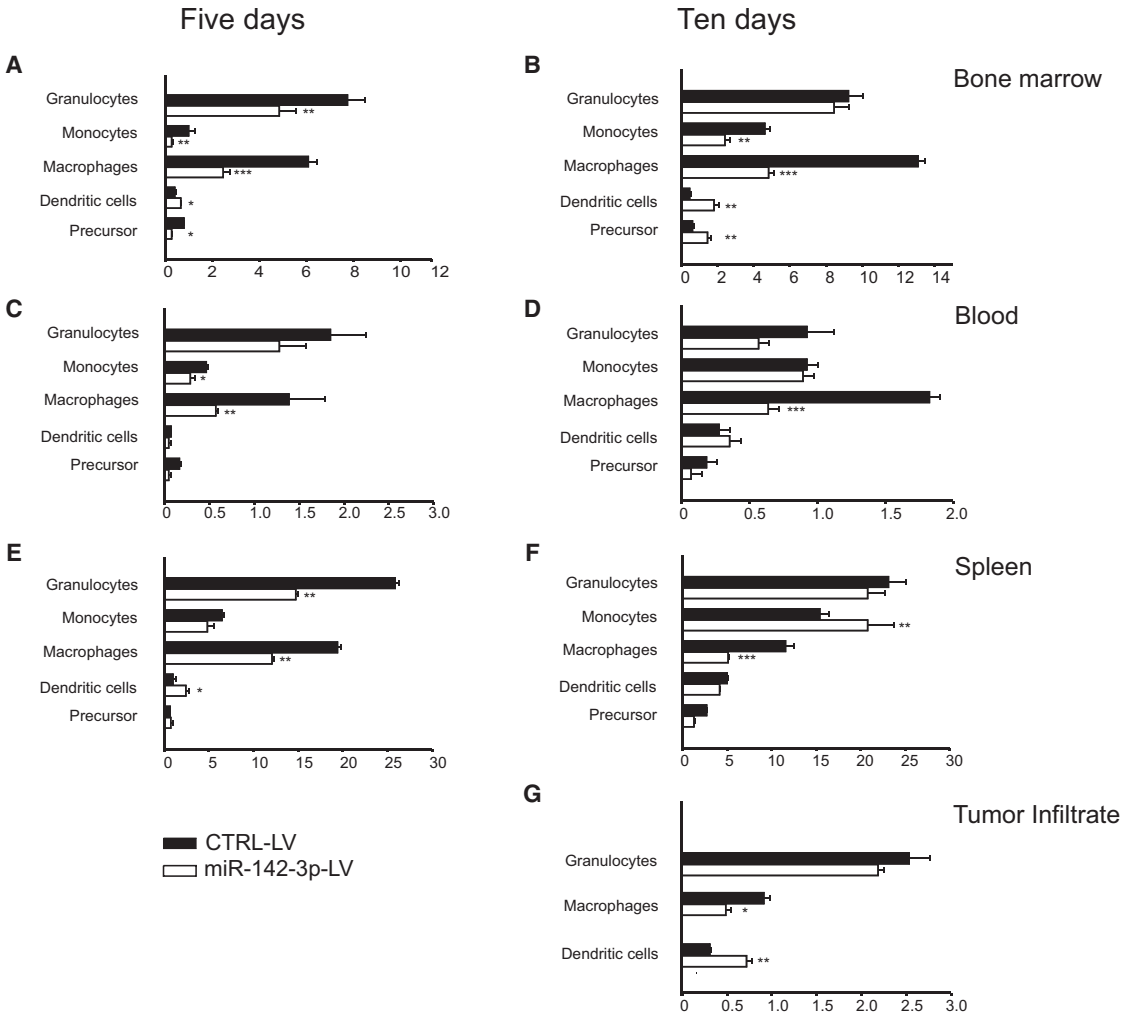

Figure 6. miR-142-3p Overexpression Alters Tumor Microenvironment

(A–G) Myeloid infiltrate analysis in the BM, blood, spleen, and tumor mass of miR-overexpressing chimeras. FACS analyses were performed on Ly5.2$^+$/mOrange$^+$ cells at day 5 or 10 (except for tumor infiltrate, analyzed only at day 10) following MCA203 injection. Absolute numbers (×10^6) of granulocytes, monocytes, macrophages, DCs (CD11c$^+$/I-A/I-E$^+$), and hematopoietic precursors (Sca-1$^+$/c-kit$^+$) are reported.

Data are reported as mean ± SE from n = 6 mice per group, two cumulated experiments. *p < 0.05; **p < 0.01; ***p < 0.001. See also Figure S5.

variation. In particular, this ratio increases as a result of the induction of the LAP* protein, driving macrophage differentiation. In this scenario, miR-142-3p modulation plays a key role: miR downregulation, due to the LAP* increase, induces IL6st upregulation, thus sustaining its downstream pathway. Moreover, miR-142-3p downregulation determines, in a feedback loop, LAP* expression increment, further promoting myeloid cell differentiation towards immunosuppressive macrophages.

miR-142-3p Overexpression Alters Tumor Microenvironment

We then address whether miR-142-3p overexpression in vivo could alter tumor microenvironment. We transplanted Ly5.2$^+$ CD11b$^-$ BM cells infected with a miR-142-3p-coding lentiviral construct in γ-irradiated, Ly5.1$^+$ recipient mice. Infected cells, identified by the mOrange2 reporter protein, had a constant miR content, as determined in qRT-PCR (about 1.97 ± 0.26 compared to control cells). Three weeks after transplantation, mice were injected with MCA203 tumor cells, and we evaluated myeloid cell distribution in tumor mass and lymphoid organs at two different time points (Figure S5A).

At day 5, miR overexpressing mice showed a strong reduction in macrophage-monocyte subsets, a modest decrease in granulocytes, but a remarkable drop in the percentage of immature precursors. Moreover, an increase in BM-DCs was evidenced (Figure 6A). A similar drive in myeloid maturation was already reported in *Cebpb*$^{-/-}$ mice (Marigo et al., 2010), further highlighting the link between this TF and miR-142-3p.

An analogous scenario was still evident at day 10 in BM, with the exception of an increase in the precursor numbers (Figure 6B). Whereas minor differences were found among circulating and splenic cells at day 5 (Figures 6C–6E), a clear increase in the monocyte percentage and a concomitant significant reduction of the macrophage number was evidenced in

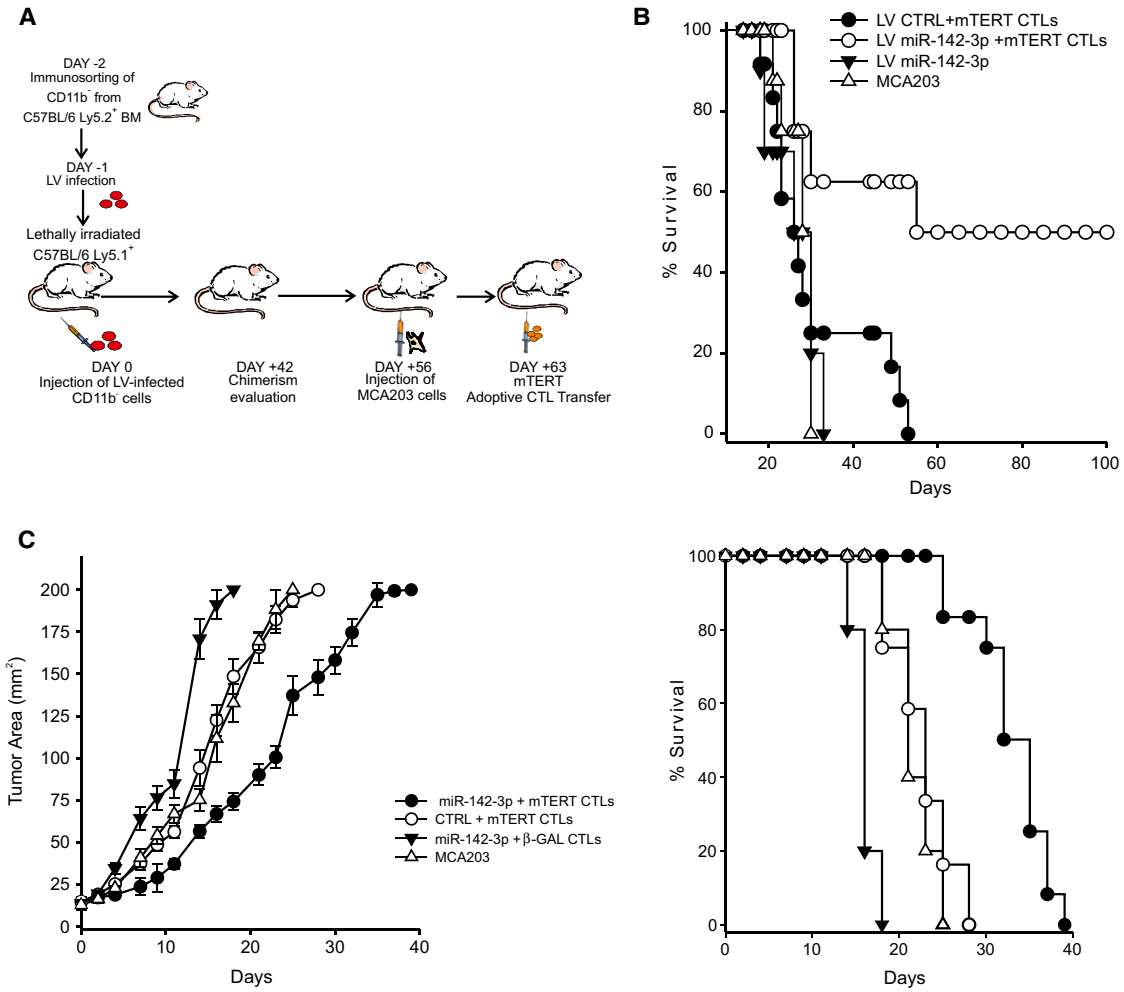

Figure 7. Enforced miR-142-3p Expression Favors Antitumor Immune Response leading to Tumor Growth Control

(A) Schedule for ACT protocol in CTRL or miR-142-3p-expressing chimeras.

(B) Survival analysis of tumor-bearing chimeras. Mantel-Haenszel statistics: LV-CTRL+mTERT CTLs versus LV-miR-142-3p+mTERT CTLs, p = 0.007; LV-miR-142-3p+mTERT CTLs versus LV-miR-142-3p, p = 0.017; LV-miR-142-3p+mTERT CTLs versus MCA203, p = 0.042. All other comparisons were not significant. n = 12 LV-CTRL+mTERT CTLs; n = 10 LV-miR-142-3p; n = 8 LV-miR-142-3p+mTERT CTLs and MCA203, two cumulated experiments.

(C) ACT was performed in MCA203 tumor-bearing mice previously transplanted with BM cells expressing either CTRL or miR-142-3p oligo. Tumor growth and survival analysis are reported. Mice were euthanized when the tumor area reached 200 mm^2. Mantel-Haenszel statistics: LV-miR-142-3p+mTERT CTLs versus MCA203, p = 0.00007; LV-CTRL+mTERT CTLs versus MCA203, p = 0.667; LV-miR-142-3p+mTERT CTLs versus LV-CTRL+mTERT CTLs, p = 0.00001. Data are reported as mean ± SE from n = 10/12 mice per group.

See also Figure S6.

the blood and the spleen of miR overexpressing mice at day 10 (Figures 6D–6F), recapitulating the in vitro block in monocyte-macrophage transition.

Tumor dimension allowed us to analyze tumor infiltrate only at the latest time point. We detected a similar decrease in the percentage of macrophages and an associated expansion of DC numbers (Figure 6G), suggesting that in vivo miR overexpression was able to change the ratio of macrophage: DC to favor the DC expansion.

Enforced miR-142-3p Expression Favors Antitumor Immune Response leading to Tumor Growth Control

The macrophage subversion and coincident DC expansion might create a more favorable microenvironment for antitumor T lymphocyte recruitment and activity. Thus, the preconditioning of BM cell differentiation by miR-142-3p expression could be an innovative strategy to improve the efficacy of cancer immunotherapy. To address this possibility, we generated stable miR-142-3p expressing chimeras and subjected them to adoptive cell therapy (ACT) with mouse telomerase (mTERT) antigen-specific T lymphocytes (CTLs) (Figure 7A). Six weeks after BM transplantation, a similar chimerism and BM reconstitution between the control and miR-overexpressing mice were found (Figures S6A and S6B).

After tumor injection, mice survival was monitored. CTRL-lentivirus chimeras receiving ACT and miR overexpressing-lentivirus chimeras without ACT died within 55 days after tumor injection, with a time course indistinguishable from nonchimeric,

tumor-bearing mice (Figure 7B). In contrast, miR overexpressing mice receiving ACT showed a prolonged survival, with 50% of them surviving till the end of the observation period (Figure 7B).

We next addressed the potential therapeutic application of miR-142-3p overexpression. MCA203 tumor-bearing, Ly5.1$^+$ mice were treated with a low dose of 5-fluoracil to induce a partial myelodepletion and then injected with syngenic Ly5.2$^+$ BM cells previously transfected with either CTRL or miR-142-3p oligo (Figure S6C). Two weeks after transplantation, a similar percentage of Ly5.2$^+$ cells in all mice groups was found (Table S6D). After adoptive transfer of either mTERT or β-GAL specific (as T lymphocytes recognizing an irrelevant antigen) CTLs, mice survival was monitored. We found that the miR-142-3p expression in conjunction with tumor-specific CTLs administration was able to delay tumor growth and significantly increase mice survival (Figure 7C).

DISCUSSION

Starting from the early steps of cancerogenesis, tumor cells modify surrounding environment to evade host immune response (Bayne et al., 2012; Pylayeva-Gupta et al., 2012). Moreover, the recruitment to tumor mass and secondary lymphoid organs of myeloid cells with immunosuppressive activity is a prominent feature of tumor progression (Gabrilovich et al., 2012; Ostrand-Rosenberg et al., 2012; Sica and Bronte, 2007). Immature DCs, macrophages, and MDSCs are expanded and recruited by tumor- and host-released factors (Gabrilovich et al., 2012; Sica and Mantovani, 2012; Viola et al., 2012). Among various factors, GM-CSF, IL-6, and M-CSF have been clearly associated with the induction of immunosuppressive programs in TIMs (Bayne et al., 2012; Bronte et al., 1999; Hume and MacDonald, 2012; Marigo et al., 2010; Pylayeva-Gupta et al., 2012), but the molecular mechanisms underlying the altered myelopoiesis in cancer remain to be fully elucidated.

During late stages of tumor progression, TAMs acquire a prevalent M2-like phenotype characterized by low IL-12 and high IL-10 expression. In contrast to M1-type macrophages, TAMs have poor antitumoral activity but they rather promote tissue remodeling and angiogenesis, favoring metastatic dissemination (Sica and Bronte, 2007; Sica and Mantovani, 2012). However, this dualistic vision is challenged by findings indicating that different functional states can be present among TAMs of the same tumor microenvironment (Movahedi et al., 2010; Torroella-Kouri et al., 2009). In numerous solid cancers, high presence of tumor-recruited macrophages is tightly correlated to poor prognosis (Qian and Pollard, 2010).

Macrophages are extremely plastic cells, and both epigenetic changes and noncoding RNAs can contribute to their polarization. For example, miR-155 can target human IL-13Rα1 subunit, thus decreasing a set of M2 genes in human macrophages (Martinez-Nunez et al., 2011). We report here that miR-142-3p controls the generation of M2-type, immunoregulatory macrophages during cancer-promoted myelopoiesis, both in vitro and in vivo, by conventional binding to 3' UTR and unconventional binding to CDS of target genes in the IL-6 cytokine-family signaling cascade. Recent studies addressing miR role as regulator of myeloid cell differentiation and accumulation have mainly considered the granulocytic subset of MDSCs (Liu et al., 2011, 2012; Zhang et al., 2011). In particular, miR-17-5p and miR-20a reduced the expression of STAT3 and modulated the suppressive activity of granulocytic CD11b$^+$ Ly6G$^+$ cells (Zhang et al., 2011). In another report, high levels of miR-494 were reported to control the nonimmunological activity of MDSCs. (Liu et al., 2012).

To identify miR regulating the function and the generation of tumor-recruited myeloid cells, we characterized their full "miRNome," following purification of CD11b$^+$ cells from five different transplantable tumors, in two genetic mouse backgrounds. The choice of evaluating a broad myeloid population sharing the CD11b marker was determined by the rationale that tumors often induce a global alteration in myeloid differentiation, resulting in extensive changes in myeloid cell subset distribution and multiple blocks in differentiation towards the myeloid mature stages (Gabrilovich et al., 2012). Isolating and comparing specific cell subsets might thus not allow to pinpoint miRs responsible for the altered myeloid differentiation program and, indeed, our data highlight the enrichments in pathways related to myeloid differentiation.

Block of macrophage differentiation due to miR-142-3p-enforced expression impaired tumor growth in vivo, but only when coupled with the adoptive transfer of tumor-specific CTLs. These results suggest that miR-142-3p mainly impacts on the regulation of the immunological activity of TAMs. Moreover, in many tissues, the decreased macrophage number was associated to increased granulocyte and DC differentiation. Because DCs and monocytes derive from the same hematopoietic precursor cells, we hypothesize that miR-142-3p upregulation is also necessary to drive myeloid differentiation towards a full DC maturation, by reducing macrophage generation. In this regard, it is known that the interplay between IL-6 and M-CSF can drive macrophage differentiation and/or polarization preventing DC maturation from monocytes. In particular, IL-6 upregulates the expression of a functional MCSF-receptor (M-CSFR) on monocytes, allowing these cells to utilize the M-CSF produced in autocrine fashion (Chomarat et al., 2000). Analogously, IL-6 family cytokines, such as LIF and IL-6, can control TAM generation and M2-polarization through the M-CSFR pathway. In the tumor microenvironment, where increased LIF and IL-6 levels are found, monocytes consume M-CSF through an augmented M-CSFR-dependent internalization, and this event is linked to the skewing towards M2-type macrophages (Duluc et al., 2007). Our data indicate that miR-142-3p modulates macrophage differentiation through the alteration of IL-6 expression and signaling. Moreover, we demonstrated a double impact of miR-142-3p on the IL-6 signaling pathway. In fact, miR-142-3p directly regulated gp130, but, more interestingly, it also modulated the downstream signaling element, C/EBPβ. In this case, we showed that miR overexpression determined a prominent reduction of the full-length isoform LAP* by binding to a noncanonical site located in the CDS.

miR-142-3p activity in the regulation of myeloid differentiation has been recently addressed (Chen et al., 2008; Wang et al., 2010). The study of Wang and collaborators reported that miR-142-3p (and miR-29a) level increased during induced maturation of both monocytes and granulocytes. Additionally, miR enforced expression is able to overcome the differentiation block, which is a specific feature of the AML samples. Thus, the

role of miR downregulation in maintaining cells in an undifferentiated phase was advocated. However, this study did not address whether a block in the monocyte-macrophage transition was consequent to miR-142-3p-enforced expression in $CD34^+$ cells. In our model, miR-142-3p overexpression did not induce myeloid differentiation but, on the contrary, impaired macrophage differentiation. This apparent discrepancy is likely due to the different models analyzed and to the stimuli used.

In addition, we unveiled a reciprocal C/EBPβ-miR-142-3p interaction and defined a feedback loop, which explains how this miR is downregulated in TIMs. Intriguingly, this mini-circuit is regulated by an unanticipated activity of LAP* and LIP isoforms. Contrary to the expectations, in fact, we found that LAP* acted as an inhibitory regulator of miR activity. However, increasing evidence shows that the "dogma," which defines LAP* as an activating and LIP as an inhibitory TF, should be revised. In fact, LIP can also positively regulate the transcription of some genes, whereas LAP* can act as an inhibitor of gene transcription (Luedde et al., 2004).

Thinking about possible therapeutic translation of our findings, we also validated miR-142-3p expression modulation as adjuvant in ACT against cancer. Transfer of tumor-antigen-specific T lymphocytes is a promising anticancer strategy, but it is mandatory to create an optimal environment to allow T lymphocyte recruitment to tumor mass and unleash their full effector functions. This was previously achieved by the conditional genetic ablation of *Cebpb* gene (Marigo et al., 2010), a strategy that is difficult to transfer to the clinic given the pleiotropic activity of this TF. We demonstrated here that the use of an oligo to enforce miR-142-3p expression could be a feasible option to modify tumor environment and favor antitumor immunity. We are currently exploring the possibility to target miR-142-3p to myeloid cells by the use of nanoparticles and dendrimers.

EXPERIMENTAL PROCEDURES

General Note

All mice were maintained under SPF conditions in the animal facility of the Istituto Oncologico Veneto, and experiments were performed according to state guidelines and approved by the local ethics committee. C57BL/6 and BALB/c mice were purchased from Harlan (Milan, Italy). Transgenic mice and tumor cell lines were described in the Supplemental Information. Mouse recombinant GM-CSF, G-CSF, IL-6, and M-CSF were purchased from Peprotech. D^b-restricted $hgp100_{25–33}$ were synthesized by JPT (Berlin, Germany).

Cell Isolation

$CD11b^+$ and $CD11b^-$ cells were isolated by using magnetic microbeads conjugated with monoclonal rat anti-mouse-human CD11b antibody. Separations were performed by Miltenyi Biotec kits and MidiMacs LS or LD columns, respectively (Miltenyi Biotec, Germany).

Flow Cytometry

Antibodies, described in Supplemental Information, and matched isotypes were purchased from eBiosciences. Fluorescence acquisition was performed with FACSCalibur™ (Becton and Dickinson) and analyzed with FlowJo software (Treestar).

Bone Marrow Cultures

BM cells were obtained as previously described (Marigo et al., 2010). To obtain BM-MDSCs, we plated 1.2×10^6 cells into 6-well plates in medium supplemented with either cytokines or 25% v/v TCCM and maintained at 37°C in a 5% CO_2-humidified atmosphere for 4 days. TCCM was obtained by culturing subconfluent tumor cells in medium with 3% serum for 48 hr. Supernatants were then collected, aliquoted, and kept at −80°C until use.

BM Transfection

Fresh BM cells were transfected with either 100 nM of miR-142-3p mimic or scramble CTRL oligo (IDT), by using the transfection agent GeneSilencer (Genlantis) according to manufacturer's instructions. After 5 hours, cytokines or TCCM were added.

In Vitro CFDA-SE Labeling and Proliferation Assay

Mixed-leukocyte peptide cultures (MLPC) were set up as described in Supplemental Information.

qRT-PCR

Total RNA was extracted from cells by using Trizol reagent (Life Technologies). Taqman probes were used for the detection of miRs (Applied Biosystems), as described by the manufacturer, by using small nuclear RNA sno292 as endogenous control. For mRNA-level analysis, cDNA was generated by using reverse transcriptase SuperScript II and poly dT primers (Invitrogen). Real-time PCR was performed by using SYBR Green Master Mix (Invitrogen) and the ABI 7900HT fast real-time PCR System (Applied Biosystems). Primers are described in the Supplemental Information. S18 was used as endogenous control. Relative quantification of miRNA and mRNA expression was performed by using the ΔΔCT method.

Enzyme-Linked Immunosorbent Assay

ELISA for murine IL-12p70 and IL-10 was performed with R&D kits, following manufacturer's instructions.

Immunoblot Analysis

Nuclear cell extracts were obtained from 3×10^6 cells by using the Pierce NE-PER nuclear reagents (Pierce Biotechnology) in presence of protease inhibitors (Calbiochem). The following antibodies were used: C/EBPβ (1:1,000, Santa Cruz), gp130 (1:1,000, eBiosciences), p-STAT-3 Tyr705 (1:1,000, Cell Signaling), STAT3 (1:1,000, Santa Cruz), Nucleoporin p62 (1:1,000, BD), and α-Actin (1:5,000, Sigma). Secondary HRP-conjugated Abs were obtained from GE Healthcare Life Sciences. Immunoblots were analyzed by ECL (Pierce Biotecnology). Signal quantification was performed by using ImageJ Software.

Transduction of Hematopoietic Progenitor-Enriched $CD11b^-$ Cells and Transplantation Procedure

We transduced 3×10^6 BM-$CD11b^-$ cells with mock, miR-142-3p expressing or miR-142-3p sponge lentiviral vector stocks, produced as described in Supplemental Information, at a multiplicity of infection (MOI) of 75 for 18 hour. For in vitro experiments, $CD11b^-$-transduced cells were cultured in G-CSF-containing medium for 4 days. Transduction of $CD11b^-$ and stable chimera generation were obtained as previously described (Montini et al., 2006).

Adoptive T Cell Transfer Protocol

Eight weeks after transplantation, chimera mice were injected s.c. with MCA203 fibrosarcoma cells and ACT was performed as previously described (Ugel et al., 2010).

Luciferase Reporter Assay

HEK293T cells were cultured to 80% confluence in 24-well plates and transfected as described in Supplemental Information.

Statistics

All results are expressed as mean ± SE. Student's t test was used to determine p values. Kaplan-Meier survival analysis was performed for the comparison of survival curves. Statistical significance was defined as $p < 0.05$. In figures, asterisks were used as follows: * $p \leq 0.05$; ** $p \leq 0.01$; *** $p \leq 0.001$.

ACCESSION NUMBERS

The microarray data for miRs and gene expression analyses are available in the Gene Expression Omnibus (GEO) database (http://www.ncbi.nlm.nih.gov/gds) under the accession numbers GSE39807 and GSE39803.

SUPPLEMENTAL INFORMATION

Supplemental Information includes six figures and Supplemental Experimental Procedures and can be found with this article online at http://dx.doi.org/10.1016/j.immuni.2013.06.004.

ACKNOWLEDGEMENTS

We thank Maurizio Buggio, Serena Zilio, and Stefano Ugel for help with the in vivo experiments and Andrea Predonzani for the generation of plasmids. This work was supported by grants from the Italian Ministry of Education, University and Research (FIRB project RBAP11T3WB_003 and MIUR project 2009NREAT2_003), Italian Association for Cancer Research (AIRC, Grants IG10400, 12182, AGIMM 100005, and 6599), and AIRC-Cariparo, Regional Grant 2008. The work of C.T. was supported by the BMBF 01KU1214B (OBIHEP 360365).

Received: August 31, 2012
Accepted: March 25, 2013
Published: June 27, 2013

REFERENCES

Baldwin, B.R., Timchenko, N.A., and Zahnow, C.A. (2004). Epidermal growth factor receptor stimulation activates the RNA binding protein CUG-BP1 and increases expression of C/EBPbeta-LIP in mammary epithelial cells. Mol. Cell. Biol. *24*, 3682–3691.

Baltimore, D., Boldin, M.P., O'Connell, R.M., Rao, D.S., and Taganov, K.D. (2008). MicroRNAs: new regulators of immune cell development and function. Nat. Immunol. *9*, 839–845.

Bartel, D.P. (2009). MicroRNAs: target recognition and regulatory functions. Cell *136*, 215–233.

Bayne, L.J., Beatty, G.L., Jhala, N., Clark, C.E., Rhim, A.D., Stanger, B.Z., and Vonderheide, R.H. (2012). Tumor-derived granulocyte-macrophage colony-stimulating factor regulates myeloid inflammation and T cell immunity in pancreatic cancer. Cancer Cell *21*, 822–835.

Bronte, V., Chappell, D.B., Apolloni, E., Cabrelle, A., Wang, M., Hwu, P., and Restifo, N.P. (1999). Unopposed production of granulocyte-macrophage colony-stimulating factor by tumors inhibits CD8+ T cell responses by dysregulating antigen-presenting cell maturation. J. Immunol. *162*, 5728–5737.

Chen, C.Z., and Lodish, H.F. (2005). MicroRNAs as regulators of mammalian hematopoiesis. Semin. Immunol. *17*, 155–165.

Chen, C.Z., Li, L., Lodish, H.F., and Bartel, D.P. (2004). MicroRNAs modulate hematopoietic lineage differentiation. Science (New York, N.Y *303*, 83-86.

Chen, A., Luo, M., Yuan, G., Yu, J., Deng, T., Zhang, L., Zhou, Y., Mitchelson, K., and Cheng, J. (2008). Complementary analysis of microRNA and mRNA expression during phorbol 12-myristate 13-acetate (TPA)-induced differentiation of HL-60 cells. Biotechnol. Lett. *30*, 2045–2052.

Chomarat, P., Banchereau, J., Davoust, J., and Palucka, A.K. (2000). IL-6 switches the differentiation of monocytes from dendritic cells to macrophages. Nat. Immunol. *1*, 510–514.

Clark, C.E., Hingorani, S.R., Mick, R., Combs, C., Tuveson, D.A., and Vonderheide, R.H. (2007). Dynamics of the immune reaction to pancreatic cancer from inception to invasion. Cancer Res. *67*, 9518–9527.

Corzo, C.A., Cotter, M.J., Cheng, P., Cheng, F., Kusmartsev, S., Sotomayor, E., Padhya, T., McCaffrey, T.V., McCaffrey, J.C., and Gabrilovich, D.I. (2009). Mechanism regulating reactive oxygen species in tumor-induced myeloid-derived suppressor cells. J. Immunol. *182*, 5693–5701.

Dolcetti, L., Peranzoni, E., Ugel, S., Marigo, I., Fernandez Gomez, A., Mesa, C., Geilich, M., Winkels, G., Traggiai, E., Casati, A., et al. (2010). Hierarchy of immunosuppressive strength among myeloid-derived suppressor cell subsets is determined by GM-CSF. Eur. J. Immunol. *40*, 22–35.

Duluc, D., Delneste, Y., Tan, F., Moles, M.P., Grimaud, L., Lenoir, J., Preisser, L., Anegon, I., Catala, L., Ifrah, N., et al. (2007). Tumor-associated leukemia inhibitory factor and IL-6 skew monocyte differentiation into tumor-associated macrophage-like cells. Blood *110*, 4319–4330.

Eruslanov, E., Daurkin, I., Ortiz, J., Vieweg, J., and Kusmartsev, S. (2010). Pivotal Advance: Tumor-mediated induction of myeloid-derived suppressor cells and M2-polarized macrophages by altering intracellular PGE_2 catabolism in myeloid cells. J. Leukoc. Biol. *88*, 839–848.

Fang, Z., and Rajewsky, N. (2011). The impact of miRNA target sites in coding sequences and in 3'UTRs. PLoS ONE *6*, e18067.

Fontana, L., Pelosi, E., Greco, P., Racanicchi, S., Testa, U., Liuzzi, F., Croce, C.M., Brunetti, E., Grignani, F., and Peschle, C. (2007). MicroRNAs 17-5p-20a-106a control monocytopoiesis through AML1 targeting and M-CSF receptor upregulation. Nat. Cell Biol. *9*, 775–787.

Fukuda, A., Wang, S.C., Morris, J.P., 4th, Folias, A.E., Liou, A., Kim, G.E., Akira, S., Boucher, K.M., Firpo, M.A., Mulvihill, S.J., and Hebrok, M. (2011). Stat3 and MMP7 contribute to pancreatic ductal adenocarcinoma initiation and progression. Cancer Cell *19*, 441–455.

Gabrilovich, D.I., Ostrand-Rosenberg, S., and Bronte, V. (2012). Coordinated regulation of myeloid cells by tumours. Nature reviews *12*, 253–268.

Gade, P., Roy, S.K., Li, H., Nallar, S.C., and Kalvakolanu, D.V. (2008). Critical role for transcription factor C/EBP-beta in regulating the expression of death-associated protein kinase 1. Mol. Cell. Biol. *28*, 2528–2548.

Gallina, G., Dolcetti, L., Serafini, P., De Santo, C., Marigo, I., Colombo, M.P., Basso, G., Brombacher, F., Borrello, I., Zanovello, P., et al. (2006). Tumors induce a subset of inflammatory monocytes with immunosuppressive activity on CD8+ T cells. J. Clin. Invest. *116*, 2777–2790.

Gil-Bernabé, A.M., Ferjancic, S., Tlalka, M., Zhao, L., Allen, P.D., Im, J.H., Watson, K., Hill, S.A., Amirkhosravi, A., Francis, J.L., et al. (2012). Recruitment of monocytes/macrophages by tissue factor-mediated coagulation is essential for metastatic cell survival and premetastatic niche establishment in mice. Blood *119*, 3164–3175.

Gutsch, R., Kandemir, J.D., Pietsch, D., Cappello, C., Meyer, J., Simanowski, K., Huber, R., and Brand, K. (2011). CCAAT/enhancer-binding protein beta inhibits proliferation in monocytic cells by affecting the retinoblastoma protein/E2F/cyclin E pathway but is not directly required for macrophage morphology. J. Biol. Chem. *286*, 22716–22729.

Hatfield, S.D., Shcherbata, H.R., Fischer, K.A., Nakahara, K., Carthew, R.W., and Ruohola-Baker, H. (2005). Stem cell division is regulated by the microRNA pathway. Nature *435*, 974–978.

Hume, D.A., and MacDonald, K.P. (2012). Therapeutic applications of macrophage colony-stimulating factor-1 (CSF-1) and antagonists of CSF-1 receptor (CSF-1R) signaling. Blood *119*, 1810–1820.

Kusmartsev, S., and Gabrilovich, D.I. (2005). STAT1 signaling regulates tumor-associated macrophage-mediated T cell deletion. J. Immunol. *174*, 4880–4891.

Lawrence, T., and Natoli, G. (2011). Transcriptional regulation of macrophage polarization: enabling diversity with identity. Nature reviews *11*, 750–761.

Lesina, M., Kurkowski, M.U., Ludes, K., Rose-John, S., Treiber, M., Klöppel, G., Yoshimura, A., Reindl, W., Sipos, B., Akira, S., et al. (2011). Stat3/Socs3 activation by IL-6 transsignaling promotes progression of pancreatic intraepithelial neoplasia and development of pancreatic cancer. Cancer Cell *19*, 456–469.

Liu, Q., Zhang, M., Jiang, X., Zhang, Z., Dai, L., Min, S., Wu, X., He, Q., Liu, J., Zhang, Y., et al. (2011). miR-223 suppresses differentiation of tumor-induced $CD11b^+$ $Gr1^+$ myeloid-derived suppressor cells from bone marrow cells. Int. J. Cancer *129*, 2662–2673.

Liu, Y., Lai, L., Chen, Q., Song, Y., Xu, S., Ma, F., Wang, X., Wang, J., Yu, H., Cao, X., and Wang, Q. (2012). MicroRNA-494 is required for the accumulation

and functions of tumor-expanded myeloid-derived suppressor cells via targeting of PTEN. J. Immunol. *188*, 5500–5510.

Luedde, T., Duderstadt, M., Streetz, K.L., Tacke, F., Kubicka, S., Manns, M.P., and Trautwein, C. (2004). C/EBP beta isoforms LIP and LAP modulate progression of the cell cycle in the regenerating mouse liver. Hepatology *40*, 356–365.

Mantovani, A., Sozzani, S., Locati, M., Allavena, P., and Sica, A. (2002). Macrophage polarization: tumor-associated macrophages as a paradigm for polarized M2 mononuclear phagocytes. Trends Immunol. *23*, 549–555.

Marigo, I., Bosio, E., Solito, S., Mesa, C., Fernandez, A., Dolcetti, L., Ugel, S., Sonda, N., Bicciato, S., Falisi, E., et al. (2010). Tumor-induced tolerance and immune suppression depend on the C/EBPbeta transcription factor. Immunity *32*, 790–802.

Martinez-Nunez, R.T., Louafi, F., and Sanchez-Elsner, T. (2011). The interleukin 13 (IL-13) pathway in human macrophages is modulated by microRNA-155 via direct targeting of interleukin 13 receptor alpha1 (IL13Ralpha1). J. Biol. Chem. *286*, 1786–1794.

Miska, E.A. (2005). How microRNAs control cell division, differentiation and death. Curr. Opin. Genet. Dev. *15*, 563–568.

Montini, E., Cesana, D., Schmidt, M., Sanvito, F., Ponzoni, M., Bartholomae, C., Sergi Sergi, L., Benedicenti, F., Ambrosi, A., Di Serio, C., et al. (2006). Hematopoietic stem cell gene transfer in a tumor-prone mouse model uncovers low genotoxicity of lentiviral vector integration. Nat. Biotechnol. *24*, 687–696.

Movahedi, K., Laoui, D., Gysemans, C., Baeten, M., Stangé, G., Van den Bossche, J., Mack, M., Pipeleers, D., In't Veld, P., De Baetselier, P., and Van Ginderachter, J.A. (2010). Different tumor microenvironments contain functionally distinct subsets of macrophages derived from Ly6C(high) monocytes. Cancer Res. *70*, 5728–5739.

Munera, V., Popovic, P.J., Bryk, J., Pribis, J., Caba, D., Matta, B.M., Zenati, M., and Ochoa, J.B. (2010). Stat 6-dependent induction of myeloid derived suppressor cells after physical injury regulates nitric oxide response to endotoxin. Ann. Surg. *251*, 120–126.

Murray, P.J., and Wynn, T.A. (2011). Protective and pathogenic functions of macrophage subsets. Nature reviews *11*, 723–737.

Nefedova, Y., Nagaraj, S., Rosenbauer, A., Muro-Cacho, C., Sebti, S.M., and Gabrilovich, D.I. (2005). Regulation of dendritic cell differentiation and antitumor immune response in cancer by pharmacologic-selective inhibition of the janus-activated kinase 2/signal transducers and activators of transcription 3 pathway. Cancer Res. *65*, 9525–9535.

Ostrand-Rosenberg, S., Sinha, P., Beury, D.W., and Clements, V.K. (2012). Cross-talk between myeloid-derived suppressor cells (MDSC), macrophages, and dendritic cells enhances tumor-induced immune suppression. Semin. Cancer Biol. *22*, 275–281.

Pylayeva-Gupta, Y., Lee, K.E., Hajdu, C.H., Miller, G., and Bar-Sagi, D. (2012). Oncogenic Kras-induced GM-CSF production promotes the development of pancreatic neoplasia. Cancer Cell *21*, 836–847.

Qian, B.Z., and Pollard, J.W. (2010). Macrophage diversity enhances tumor progression and metastasis. Cell *141*, 39–51.

Schmeier, S., MacPherson, C.R., Essack, M., Kaur, M., Schaefer, U., Suzuki, H., Hayashizaki, Y., and Bajic, V.B. (2009). Deciphering the transcriptional circuitry of microRNA genes expressed during human monocytic differentiation. BMC Genomics *10*, 595.

Sica, A., and Bronte, V. (2007). Altered macrophage differentiation and immune dysfunction in tumor development. J. Clin. Invest. *117*, 1155–1166.

Sica, A., and Mantovani, A. (2012). Macrophage plasticity and polarization: in vivo veritas. J. Clin. Invest. *122*, 787–795.

Smink, J.J., Bégay, V., Schoenmaker, T., Sterneck, E., de Vries, T.J., and Leutz, A. (2009). Transcription factor C/EBPbeta isoform ratio regulates osteoclastogenesis through MafB. EMBO J. *28*, 1769–1781.

Sonda, N., Chioda, M., Zilio, S., Simonato, F., and Bronte, V. (2011). Transcription factors in myeloid-derived suppressor cell recruitment and function. Curr. Opin. Immunol. *23*, 279–285.

Takahashi, H., Kanno, T., Nakayamada, S., Hirahara, K., Sciumè, G., Muljo, S.A., Kuchen, S., Casellas, R., Wei, L., Kanno, Y., and O'Shea, J.J. (2012). TGF-β and retinoic acid induce the microRNA miR-10a, which targets Bcl-6 and constrains the plasticity of helper T cells. Nat. Immunol. *13*, 587–595.

Tay, Y., Zhang, J., Thomson, A.M., Lim, B., and Rigoutsos, I. (2008). MicroRNAs to Nanog, Oct4 and Sox2 coding regions modulate embryonic stem cell differentiation. Nature *455*, 1124–1128.

Torroella-Kouri, M., Silvera, R., Rodriguez, D., Caso, R., Shatry, A., Opiela, S., Ilkovitch, D., Schwendener, R.A., Iragavarapu-Charyulu, V., Cardentey, Y., et al. (2009). Identification of a subpopulation of macrophages in mammary tumor-bearing mice that are neither M1 nor M2 and are less differentiated. Cancer Res. *69*, 4800–4809.

Turner, M.L., Schnorfeil, F.M., and Brocker, T. (2011). MicroRNAs regulate dendritic cell differentiation and function. J. Immunol. *187*, 3911–3917.

Ugel, S., Scarselli, E., Iezzi, M., Mennuni, C., Pannellini, T., Calvaruso, F., Cipriani, B., De Palma, R., Ricci-Vitiani, L., Peranzoni, E., et al. (2010). Autoimmune B-cell lymphopenia after successful adoptive therapy with telomerase-specific T lymphocytes. Blood *115*, 1374–1384.

Viola, A., Sarukhan, A., Bronte, V., and Molon, B. (2012). Mol. Biol. Rep. *39*, 2713–2722.

Wang, J., Liu, Y., Li, Z., Du, J., Ryu, M.J., Taylor, P.R., Fleming, M.D., Young, K.H., Pitot, H., and Zhang, J. (2010). Endogenous oncogenic Nras mutation promotes aberrant GM-CSF signaling in granulocytic/monocytic precursors in a murine model of chronic myelomonocytic leukemia. Blood *116*, 5991–6002.

Zhang, H., Nguyen-Jackson, H., Panopoulos, A.D., Li, H.S., Murray, P.J., and Watowich, S.S. (2010). STAT3 controls myeloid progenitor growth during emergency granulopoiesis. Blood *116*, 2462–2471.

Zhang, M., Liu, Q., Mi, S., Liang, X., Zhang, Z., Su, X., Liu, J., Chen, Y., Wang, M., Zhang, Y., et al. (2011). Both miR-17-5p and miR-20a alleviate suppressive potential of myeloid-derived suppressor cells by modulating STAT3 expression. J. Immunol. *186*, 4716–4724.

Zhou, B., Wang, S., Mayr, C., Bartel, D.P., and Lodish, H.F. (2007). miR-150, a microRNA expressed in mature B and T cells, blocks early B cell development when expressed prematurely. Proc. Natl. Acad. Sci. USA *104*, 7080–7085.

Reduced phosphatidylinositol 4,5-bisphosphate synthesis impairs inner ear Ca^{2+} signaling and high-frequency hearing acquisition

Laura Rodriguez[a,b,1], Elena Simeonato[a,c,1], Pietro Scimemi[d,e], Fabio Anselmi[a], Bianca Calì[a], Giulia Crispino[a,b], Catalin D. Ciubotaru[a,f], Mario Bortolozzi[a,b], Fabian Galindo Ramirez[a], Paromita Majumder[a], Edoardo Arslan[d,e], Pietro De Camilli[g,h], Tullio Pozzan[a,i,j,2], and Fabio Mammano[a,b,j,2]

[a]Istituto Veneto di Medicina Molecolare, Fondazione per la Ricerca Biomedica Avanzata, 35129 Padua, Italy; [b]Dipartimento di Fisica e Astronomia "G. Galilei"; [c]Dipartimento di Medicina Molecolare, and [i]Dipartimento di Scienze Biomediche, Università di Padova, 35131 Padua, Italy; [d]Dipartimento di Neuroscienze Scienze Npsrr, Università di Padova, 35129 Padua, Italy; [e]Servizio di Audiologia, Ospedale "Ca' Foncello," 31100 Treviso, Italy; [f]Consorzio Interuniversitario Nazionale per la Scienza e Tecnologia dei Materiali, 50121 Florence, Italy; [g]Howard Hughes Medical Institute and [h]Departments of Cell Biology and Neurobiology, Program in Cellular Neuroscience, Neurodegeneration and Repair, Yale University School of Medicine, New Haven, CT 06510; and [j]Consiglio Nazionale delle Ricerche, Istituto di Neuroscienze, Sezione di Padova, 35131 Padua, Italy

Contributed by Tullio Pozzan, July 13, 2012 (sent for review October 20, 2011)

Phosphatidylinositol phosphate kinase type 1γ (PIPKIγ) is a key enzyme in the generation of phosphatidylinositol 4,5-bisphosphate [PI(4,5)P_2] and is expressed at high levels in the nervous system. Homozygous knockout mice lacking this enzyme die postnatally within 24 h, whereas PIPKIγ$^{+/-}$ siblings breed normally and have no reported phenotype. Here we show that adult PIPKIγ$^{+/-}$ mice have dramatically elevated hearing thresholds for high-frequency sounds. During the first postnatal week we observed a reduction of ATP-dependent Ca^{2+} signaling activity in cochlear nonsensory cells. Because Ca^{2+} signaling under these conditions depends on inositol-1,4,5-trisphosphate generation from phospholipase C (PLC)-dependent hydrolysis of PI(4,5)P_2, we conclude that (*i*) PIPKIγ is primarily responsible for the synthesis of the receptor-regulated PLC-sensitive PI(4,5)P_2 pool in the cell syncytia that supports auditory hair cells; (*ii*) spatially graded impairment of this signaling pathway in cochlear nonsensory cells causes a selective alteration in the acquisition of hearing in PIPKIγ$^{+/-}$ mice. This mouse model also suggests that PIPKIγ may determine the level of gap junction contribution to cochlear development.

connexins | deafness | phosphoinositides | Ca^{2+} oscillations | NF-κB

Cell stimulation with a variety of agents triggers signaling cascades that involve PI(4,5)P_2, a minor glycerophospholipid of the inner leaflet of the plasma membrane. PI(4,5)P_2 contributes to these processes by being converted into second messengers, by controlling the activity of PI(4,5)P_2-binding proteins, or by acting as the substrate of PI(3,4,5)P_3 kinase (1). Phospholipase C (PLC)-dependent hydrolysis of PI(4,5)P_2 generates the second messenger molecules diacylglycerol and IP_3; the latter binds to IP_3 receptors (IP_3R) to activate Ca^{2+} efflux from the endoplasmic reticulum, raising the cytosolic free Ca^{2+} concentration ($[Ca^{2+}]_i$) (2).

Most plasma membrane PI(4,5)P_2 is generated by phosphorylation of PI(4)P at the D-5 position of the inositol ring, a reaction catalyzed by type I PI(4)P 5-kinases (PIPKI) (1). Distinct genes encode the three PIPKI isoforms, named α, β, and γ (note that nomenclature for the murine and human isoforms of $PIPKI_\alpha$ and $PIPKI_\beta$ were previously inconsistent; in this article, the murine nomenclature is used); the three isoforms localize within different compartments and play specific roles in individual cell types, because one isoform cannot compensate for the loss of another (3, 4). Of the three isoforms, PIPKIγ is the one expressed at highest concentration in the nervous system (5) in platelets and megakaryocytes (6).

Knockout mice have been generated for all three isoforms of PIPKI. PIPKIα$^{-/-}$ mice develop normally but show increased degranulation and cytokine production by mast cells activated via the Fcε receptor (7). PIPKIβ$^{-/-}$ mice have a normal phenotype except for decreased fertility; however, platelets from these mice show diminished PI(4,5)P_2 production, PLC activation, and IP_3 production after thrombin treatment (6). PIPKIγ$^{-/-}$ mice, in which exons 2–6 of the PIPKIγ gene (*Pip5k1c*) that encode most of the catalytic region were deleted by homologous recombination, present decreased levels of PI(4,5)P_2 in the nervous system (5). Whereas PIPKIγ$^{+/-}$ mice breed normally and have no obvious phenotype, all PIPKIγ$^{-/-}$ mice are recognizable soon after birth by their impaired motility, and they die postnatally within 24 h. The inability of these mice to feed after birth strongly suggested the occurrence of major neurological defects. Indeed, cortical neurons in primary cultures of from PIPKIγ$^{-/-}$ mice revealed defects in synaptic transmission that may result, at least in part, from an impairment of synaptic vesicle traffic (5). Note that another PIPKIγ knockout mouse generated by random insertional mutagenesis exhibits embryonic lethality at midgestation (8); the reason for this discrepancy is not known.

Here we report that PIPKIγ deficiency in mice results in a sizeable and spatially graded down-regulation of IP_3R Ca^{2+} signaling along the sensory epithelium of the cochlea (inner ear) during a crucial postnatal period that precedes acquisition of hearing, which in mice occurs around postnatal day 12 (P12, where P0 indicates day of birth). This reduction of Ca^{2+} signaling correlates with the appearance of a specific deafness phenotype in adult PIPKIγ$^{+/-}$ mice, characterized by normal sensitivity to low-frequency sounds but a dramatic reduction of the sensitivity to frequencies in excess of 20 kHz. These data are discussed in terms of present models of inner ear development and sound perception.

Results

Hearing relies on a sensitive mechanoelectrical transduction process in the cochlea of the inner ear, in which the organ of Corti encompasses highly specialized sensory hair cells that are embedded in a matrix of supporting and epithelial cells, henceforth designated as *cochlear nonsensory cells*. The functional maturation of the cochlea relies not only on the differentiation of hair cells and the formation of coordinately polarized hair bundles, but also on the formation of nonsensory cell networks, which form vast functional syncytia coupling transfer of ions, signaling molecules and nutrients through gap junction channels (9). Our recent work has linked alterations of IP_3R Ca^{2+} signaling in nonsensory cells of the developing cochlea to impaired hearing acquisition in mouse

Author contributions: T.P. and F.M. designed research; L.R., E.S., P.S., F.A., B.C., G.C., F.G.R., and P.M. performed research; P.D.C. contributed new reagents/analytic tools; L.R., E.S., P.S., F.A., G.C., C.D.C., M.B., F.G.R., E.A., T.P., and F.M. analyzed data; and P.D.C., T.P., and F.M. wrote the paper.

The authors declare no conflict of interest.

Freely available online through the PNAS open access option.

[1]L.R. and E.S. contributed equally to this work.

[2]To whom correspondence may be addressed. E-mail: tullio.pozzan@unipd.it or fabio.mammano@unipd.it.

This article contains supporting information online at www.pnas.org/lookup/suppl/doi:10.1073/pnas.1211869109/-/DCSupplemental.

models of human hereditary deafness (10). On the basis of the primary role played by PIPKIγ in IP_3 signaling, although no phenotype has been described in PIPKIγ$^{+/-}$ mice, we would predict that a reduction of $PI(4,5)P_2$ levels may affect the development of hearing capability. Accordingly, it seemed of potentially great interest to investigate the hearing performances of transgenic mice with PIPKIγ deficiency.

Hearing Loss in PIPKIγ$^{+/-}$ Mice. Initially, we examined hearing in adult PIPKIγ$^{+/-}$ mice by recording auditory brainstem responses (ABRs), which are electrical signals evoked from the brainstem by the presentation of sound stimuli (Fig. 1). We assessed ABR thresholds in ($n = 6$) PIPKIγ$^{+/-}$ mice and ($n = 4$) WT siblings and found similar values for click and tone burst stimuli at 8, 14, and 20 kHz. However, thresholds where significantly elevated in PIPKIγ$^{+/-}$ mice compared with WT animals, by more than 12 and 33 dB sound pressure level (SPL), respectively, at 26 kHz ($P = 0.003$) and 32 kHz ($P = 0.0002$). These results demonstrate that PIPKIγ deficiency ensues in a unique phenotype of hearing loss at high sound frequencies, which are mapped onto the basal 50% of the length of the mouse cochlea (11) (Fig. 1*B*). Note that the structure of ABR waveforms, when identifiable, was well preserved at all frequencies (Fig. 1*A*). This behavior suggests normal general functioning of the nervous system and in particular of the neural elements contributing to the generation of synchronized discharges along the auditory nerve and brainstem pathway; and this is also consistent with the lack of an overt neurologic phenotype in these heterozygous mice. Confocal microscopy in adult PIPKIγ$^{+/-}$ mice revealed neither hair cell loss nor morphological abnormalities in spiral ganglion neurons and organ of Corti, which appeared normally innervated (*SI Appendix*, Fig. S1). In particular, the density of nerve fibers in tangential sections of the osseous spiral lamina (expressed as number of fibers per mm^2) was $(1.6 \pm 0.2) \times 10^5$ in WT and $(1.6 \pm 0.4) \times 10^5$ in PIPKIγ$^{+/-}$ mice.

PIPKIγ Deficiency Impairs Intercellular Ca^{2+} Waves and Intracellular $[Ca^{2+}]_i$ Oscillations Evoked by ATP in the Postnatal Cochlea. For these experiments, we used organotypic cultures of P0–P5 cochlear tissue (*SI Appendix*, Fig. S2) prepared according to standard protocols, because this preparation preserves the architecture and functional relationships among the cells observed in vivo (12). Cultures comprised the *lesser epithelial ridge* (LER), which is thought to give rise to the outer hair cells and lateral nonsensory cells, and the adjacent *greater epithelial ridge* (GER), which gives rise to the inner hair cells and medial nonsensory cells (13). After overnight incubation in vitro, we loaded cochlear cultures with the Ca^{2+} indicator fura-2 and performed ratiometric imaging of the cytosolic free Ca^{2+} concentration ($[Ca^{2+}]_i$) at room temperature (22–24 °C).

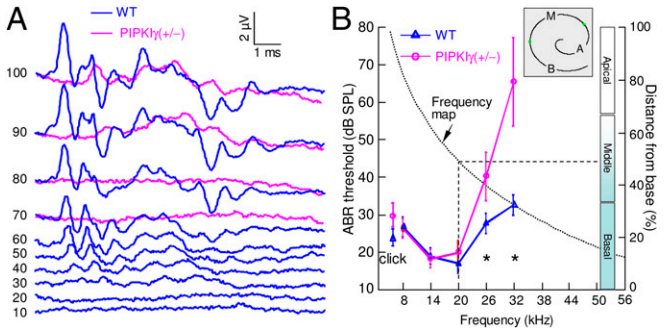

Fig. 1. Hearing loss in adult PIPKIγ$^{+/-}$ mice. (*A*) Representative ABR waveforms evoked by a 32-kHz tone burst in a WT mouse (blue) and a PIPKIγ$^{+/-}$ mouse (magenta); numbers indicate stimulus intensity in dB sound pressure level (SPL). (*B*) Average hearing thresholds (left ordinates) of wave IV ABR for clicks and tone bursts of 8, 14, 20, 26, and 32 kHz in WT mice (blue) and PIPKIγ$^{+/-}$ mice (magenta) between P27 and P50; black asterisks indicate significant differences (ANOVA); error bars, SD. The black dotted curve (right ordinates) is a portion of the mouse position vs. frequency map $d = 156.5 - 82.5 \cdot \log_{10}(f)$, where d is the normalized distance along the coiling axis of the cochlea from its base, in percent, and f is the frequency in kHz (11); dashed lines delimit the portion of the map where hearing loss in PIPKIγ$^{+/-}$ mice is noticeable; Apical (A), Middle (M), and Basal (B) refer to the three segments of the cochlear duct length shown schematically (*Inset*) (*SI Appendix*, Fig. S2).

We and others have previously demonstrated that the binding of extracellular ATP to G protein-coupled $P2Y_2$ and $P2Y_4$ receptors, expressed on the endolymphatic surface of the developing sensory epithelium, activates PLC-dependent generation of IP_3, which in turn triggers a regenerative Ca^{2+} wave that propagates for hundreds of micrometers from the site of stimulation (14–18). Using previously developed image processing algorithms (16, 17), we examined Ca^{2+} wave propagation elicited by a puff of ATP (4 μM, 50 ms) in cultures from ($n = 3$) WT, ($n = 5$) PIPKIγ$^{+/-}$, and ($n = 3$) PIPKIγ$^{-/-}$ mice (Fig. 2 *A* and *B*). Data analysis revealed a significant reduction of the propagation index in LER cells of PIPKIγ$^{+/-}$ ($P = 0.003$) and PIPKIγ$^{-/-}$ ($P = 0.001$) cultures compared with WT cultures; the reduction was more pronounced in PIPKIγ$^{-/-}$ cultures, and differences between these and PIPKIγ$^{+/-}$ cultures were statistically significant ($P = 0.011$) (Fig. 2*C*). Thus, only quantitative and not qualitative differences were observed, related to this parameter, between the heterozygous and homozygous animals. In addition, because of the postnatal lethality of PIPKIγ$^{-/-}$ mice (5), not only could we analyze only P0 tissues, but later alterations in cochlea physiology were prevented. Clearly complete loss of PIPKIγ may be particularly toxic for the whole organisms, whereas the reduction in the gene dosage in the heterozygote may be more informative of some key feature and specific of the enzymes for cochlear functions. Therefore, we concentrated exclusively on PIPKIγ$^{+/-}$ mice.

Intercellular Ca^{2+} waves are often accompanied by a trail of $[Ca^{2+}]_i$ oscillations, which can also be reliably evoked by the application of extracellular ATP at nanomolar levels (16–18). When stimulated by prolonged application of ATP (200 nM), nonsensory LER cells in cultures from P5 WT mice developed $[Ca^{2+}]_i$ oscillations that persisted for periods in excess of 10 min (Fig. 2 *D* and *E*, *Left*). By contrast, $[Ca^{2+}]_i$ oscillations in LER cells from age-matched PIPKIγ$^{+/-}$ mice ceased almost abruptly after variable time intervals that rarely exceeded 5 min (Fig. 2 *D* and *E*, *Right*). Specifically, the duration of Ca^{2+} oscillation bursts evoked by application of 200 nM ATP in the LER of PIPKIγ$^{+/-}$ cultures were 169 ± 37 s in the apical turn, 244 ± 40 s in the middle turn, and 171 ± 38 s in the basal turn ($m = 100$ cells in each of $n = 3$ cultures for each turn and each genotype).

Next, we constructed ATP dose–response functions by plotting the maximal fura-2 ratio change (ΔR_{max}) vs. [ATP] in LER cells from P5 mice (Fig. 3; each data point is the average of $m = 15$ cells in $n = 3$ cultures). In the apical turn, the dose–response of WT and PIPKIγ$^{+/-}$ cultures superimposed almost perfectly, with similar half-maximal effective concentration: $EC_{50} = 93 \pm 4$ nM in WT and $EC_{50} = 101 \pm 9$ nM in PIPKIγ$^{+/-}$ cultures. In the middle turn, the EC_{50} shifted significantly from 96 ± 5 nM of WT to 353 ± 13 nM of PIPKIγ$^{+/-}$ cultures ($P = 2 \times 10^{-4}$). In the basal turn, the shift was even more dramatic: from 72 ± 4 nM of WT to 448 ± 18 nM of PIPKIγ$^{+/-}$ cultures ($P = 5 \times 10^{-4}$). Quantitative real-time PCR (qPCR) analysis of cochlear ducts explanted from ($n = 4$) PIPKIγ$^{+/-}$ mice at P5 showed the expected reduction of PIPKIγ mRNA level compared with ($n = 4$) age-matched WT controls (Fig. 3*B*). The reduction in the basal turn was significantly more pronounced than in the middle and apical turn ($P < 0.05$), in accord with the ATP dose–response analysis (Fig. 3*A*).

The question thus arises as to whether PIPKIγ reduction also affects the amplitude of the $[Ca^{2+}]_i$ oscillations evoked by ATP in the LER (Fig. 4). Averaged waveforms had similar amplitudes in apical turn of WT and PIPKIγ$^{+/-}$ cultures; by contrast, amplitudes in middle and basal turn PIPKIγ$^{+/-}$ cultures were reduced by 24% and 22% compared with WT controls (Fig. 4, *Left*; each waveform was obtained in LER cells by averaging more than 1,500 peak-aligned $[Ca^{2+}]_i$ oscillations within 3 min from the onset of a 200-nM ATP application). Accordingly, distributions of $[Ca^{2+}]_i$ oscillation amplitudes in WT and PIPKIγ$^{+/-}$ LER cultures (Fig. 4,

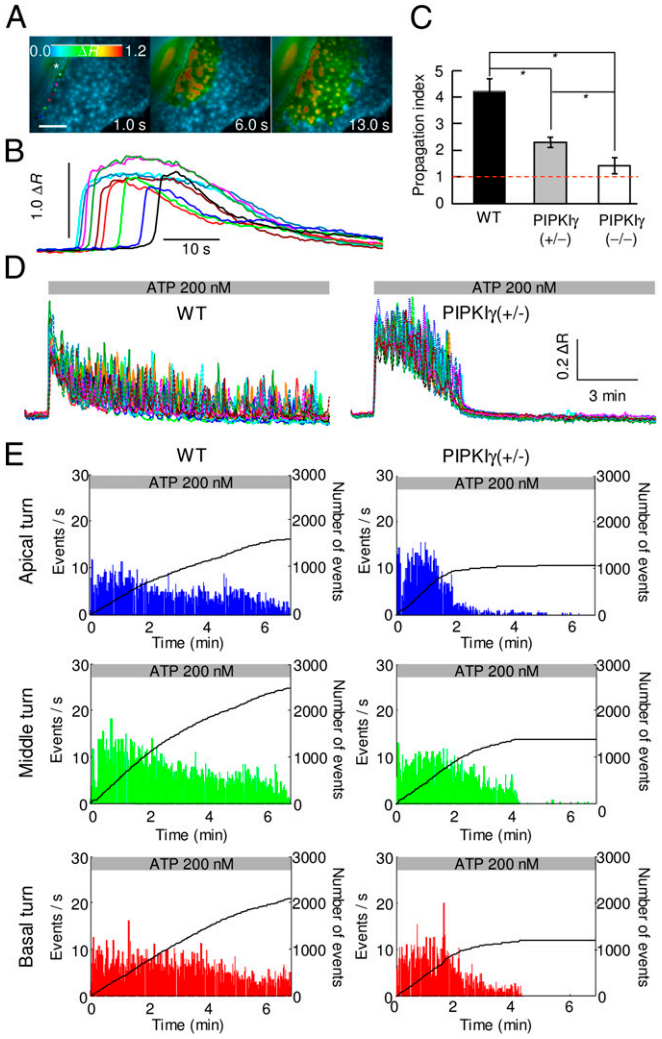

Fig. 2. ATP-evoked Ca^{2+} signaling in the LER of cochlear organotypic cultures from postnatal WT and PIPKIγ$^{+/-}$ mice. (*A*) Samples of a representative false-color image sequence showing fura-2 fluorescence ratio changes (Δ*R*), encoded as shown by the color scale bar, recorded in a WT culture after delivery of a brief puff (50 ms) of ATP (4 μM) through a glass micropipette (white asterisk); time in seconds from puff offset is shown in the lower right corner of the corresponding frame. (Scale bar, 100 μm.) (*B*) Waveforms of Ca^{2+} responses obtained by averaging signals within the nine color-matched regions of interest shown over individual cells at increasing distance from micropipette opening in *A*. (*C*) propagation index, defined as the maximal area invaded by the intercellular Ca^{2+} wave divided by the area directly stimulated by the puff (pooled data); an index of 1 indicates no propagation; black asterisks indicate significant differences (ANOVA); error bars, SD. (*D*) Sample traces of Ca^{2+} responses obtained by averaging fura-2 ratio signals within 15 randomly selected cells in representative apical turn cultures from P5 WT and PIPKIγ$^{+/-}$ mice during sustained application of extracellular ATP (200 nm, gray bars). (*E*) Frequency histograms of ATP-evoked $[Ca^{2+}]_i$ oscillations (events) in cultures from P5 WT and PIPKIγ$^{+/-}$ mice (pooled data); in each graph, the solid black line (right ordinates) is the time integral of the corresponding frequency histogram and, as such, it tracks the mean number of events in the cell population from the onset of the ATP application.

Right) overlapped in the apical turn but were shifted toward significantly lower values in middle and basal turns ($P = 2.2 \times 10^{-16}$).

PIPKIγ Deficiency Impairs Spontaneous $[Ca^{2+}]_i$ Transients in the Postnatal Cochlea. Spontaneous $[Ca^{2+}]_i$ oscillations in LER cells are rarely observed while working with cochlear organotypic cultures at room temperature, but their frequency is drastically increased upon blockade of ectoATPases (17). Conversely, spontaneous $[Ca^{2+}]_i$ transients were always observed in the GER (Fig. 5*A*). These spontaneous events have been attributed by us and other investigators to spontaneous release of ATP (19, 20) through connexin hemichannels (21). Not only have we confirmed these data in these GER preparations (sensitivity to ATP receptor antagonists and to connexin hemichannel inhibitors), but we could also show that focal UV photolysis of a caged intracellular IP_3 precursor in the GER evokes $[Ca^{2+}]_i$ transients similar to the spontaneous ones (Movie S1). In addition, and similarly to $[Ca^{2+}]_i$ oscillations induced by exogenous ATP in LER cells, (*i*) the spontaneous $[Ca^{2+}]_i$ transients showed no sign of fatigue in recordings lasting 15 min or more in the GER of ($n = 3$) WT cultures (*SI Appendix*, Fig. S3*A*, *Left*); (*ii*) the spontaneous $[Ca^{2+}]_i$ transients in the GER ceased within 5 min in ($n = 3$) WT cultures after addition of 200 nM thapsigargin (*SI Appendix*, Fig. S3*A*, *Right*) a noncompetitive inhibitor of the Ca^{2+}-ATPase (SERCA) that causes the complete and irreversible depletion of Ca^{2+} from the endoplasmic reticulum; (*iii*) the PLC inhibitor U73122 (2.5 μM) significantly ($P = 0.001$) and reversibly reduced the frequency of spontaneous $[Ca^{2+}]_i$ transients in the GER ($n = 3$; *SI Appendix*, Fig. S3*B*, *Left*); and (*iv*) the spontaneous $[Ca^{2+}]_i$ transients in the GER were also drastically reduced by the potent (although not completely specific) IP_3R antagonist 2-aminoethoxydiphenyl borate (2-APB, 100 μM; $n = 3$; *SI Appendix*, Fig. S3*B*, *Right*). Altogether, the results of these and previously published experiments (17, 21) indicate that ATP-evoked $[Ca^{2+}]_i$ oscillations in the LER and spontaneous $[Ca^{2+}]_i$ transients in the GER are generated by similar mechanisms [i.e., ATP activation of P2Y receptors (by exogenous addition of ATP in the LER or local ATP release through connexin hemichannels in the GER), followed by IP_3 generation and Ca^{2+} release from the endoplasmic reticulum].

The prediction can thus be made that PIPKIγ deficiency should also affect the pattern of spontaneous events in GER cells. We thus examined the frequency of spontaneous $[Ca^{2+}]_i$ transients in each cochlear turn by counting all events within the portion of the GER in the field view while imaging cultures obtained from P5 WT mice ($n = 4$) and age-matched PIPKIγ$^{+/-}$ siblings ($n = 4$) (Fig. 5*B*). Even considering the different areas of the GER regions along the coiling axis of the cochlea (*SI Appendix*, *SI Materials and Methods*), the 1.85-fold lower mean frequency in the basal turn with respect to the apical turn reflects a genuine reduction of spontaneous Ca^{2+} signaling activity in the different GER regions of WT cultures (Fig. 5*B*, *Left*). We then performed the same analysis in GER cells from PIPKIγ$^{+/-}$ cultures (Fig. 5*B*, *Right*). In

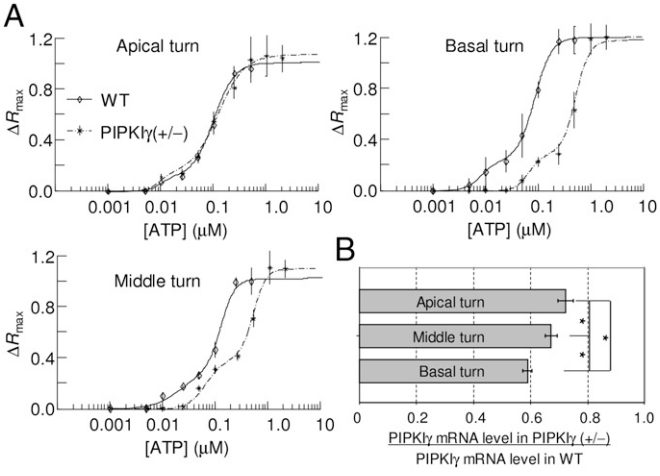

Fig. 3. ATP dose–response curves in the LER of organotypic cultures (*A*) and qPCR analysis of PIPKIγ mRNA level in the sensory epithelium (*B*) from P5 WT and PIPKIγ$^{+/-}$ cochleae (pooled data). Lines through data in *A* are least-square fits with the sum of two scaled logistic functions. Black asterisks in *B* indicate significant differences (ANOVA); error bars, SD.

CELL BIOLOGY

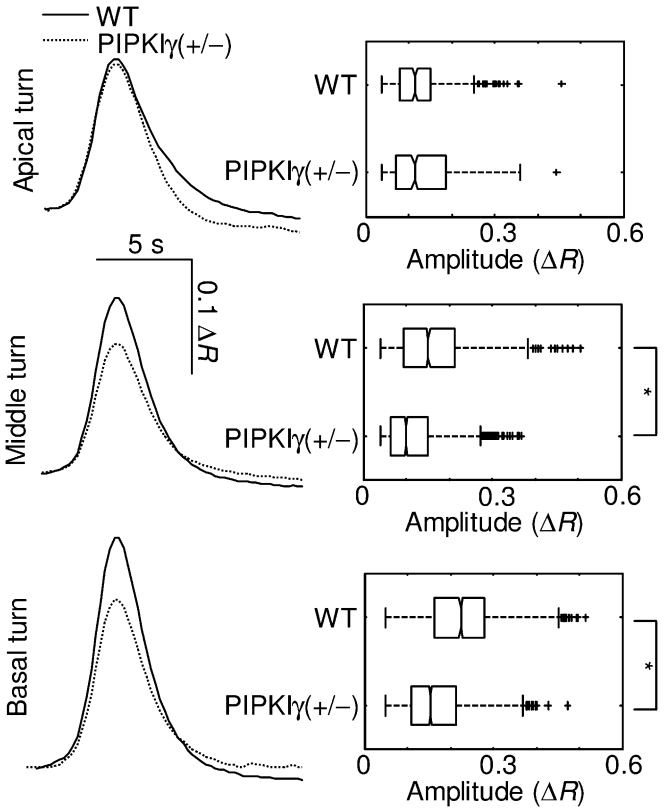

Fig. 4. Amplitudes of $[Ca^{2+}]_i$ oscillations evoked by 200 nM ATP in the LER of organotypic cochlear cultures from P5 WT and PIPKIγ$^{+/-}$ mice (pooled data). *Left*: Average waveforms; *Right*: amplitude distributions (for box plot symbolism; see, e.g., http://en.wikipedia.org/wiki/Box_plot); black asterisks indicate significant differences between data distributions (Mann–Whitney *U* test; *SI Appendix, SI Materials and Methods*).

the apical turn, we found similar mean frequencies of occurrence (39 ± 4 events per minute in WT vs. 38 ± 11 events per minute in PIPKIγ$^{+/-}$ cultures). Differences become discernible, although not statistically significant, in the middle turn (32 ± 7 events per minute in WT vs. 25 ± 8 events per minute in PIPKIγ$^{+/-}$ cultures; $P = 0.32$). They were evident (fivefold reduction) and highly significant in the basal turn (21 ± 2 events per minute in WT vs. 4 ± 1 events per minute in PIPKIγ$^{+/-}$ cultures; $P = 2 \times 10^{-4}$), in accord with the more pronounced reduction of PIPKIγ mRNA level in this turn (Fig. 3*B*).

As far as amplitudes of spontaneous $[Ca^{2+}]_i$ transients are concerned (Fig. 6), akin to what we noticed in LER cells, averaged waveforms had similar amplitudes in apical turn GER of WT and PIPKIγ$^{+/-}$ cultures; by contrast, amplitudes in middle and basal turn GER of PIPKIγ$^{+/-}$ cultures were reduced by 21% and 33% compared with WT controls (Fig. 6, *Left*; waveforms were obtained by averaging 448, 385, and 389 peak-aligned $[Ca^{2+}]_i$ transients in WT cultures, 557, 392, and 62 transients in PIPKIγ$^{+/-}$ cultures from the apical, middle, and basal turn, respectively). Accordingly, amplitude distributions of spontaneous $[Ca^{2+}]_i$ transients in the GER of PIPKIγ$^{+/-}$ cultures overlapped with WT distributions in the apical turn but were shifted toward significantly lower values ($P < 5.0 \times 10^{-5}$) both in middle and basal turns (Fig. 6, *Right*). $[Ca^{2+}]_i$ oscillations induced by exogenous ATP were not investigated in GER cells, because they superimpose to spontaneous events.

To summarize, both the amplitude and frequency of spontaneous $[Ca^{2+}]_i$ transients were drastically reduced in the basal turn and hardly affected in the apical turn of the GER. This correlates with the reduced sensitivity to ATP and the more marked reduction in the level of PIPKIγ in the basal region, suggesting that this enzyme is critical for producing the $PI(4,5)P_2$ pool responsible for IP_3 generation in cochlear nonsensory cells.

PIPKIγ Deficiency Causes Down-Regulation of Connexin Transcripts in the Postnatal Cochlea. In nonexcitable cells, such as cochlear nonsensory cells, $[Ca^{2+}]_i$ controls the dynamics of gene expression through the activation of multiple transcription factors (22, 23). A widely held hypothesis is that information is encoded mainly by the frequency of $[Ca^{2+}]_i$ oscillations (22); however, a possible role of amplitudes and duration in signal transduction has been discussed (24, 25). It has also been argued that amplitude modulation and frequency modulation differentially regulate distinct targets (26).

Our prior work with cochlear organotypic cultures had noted that $[Ca^{2+}]_i$ oscillations in nonsensory cells participate in the coordinated regulation of connexin26 (Cx26) and connexin30 (Cx30) expression through the nuclear factor-κ light chain enhancer of activated B cells (NF-κB) (27), a thoroughly investigated Ca^{2+}-dependent transcription factor (22, 23, 28). These are the only connexins expressed in the organ of Corti nonsensory cells (29), and they are essential for the cell-to-cell propagation of Ca^{2+} signals (14, 17, 18). Here we analyzed samples from ($n = 8$) P5 PIPKIγ$^{+/-}$ mice and compared mRNA levels of both connexins with the corresponding cochlear turn in ($n = 8$) age-matched WT controls. The residual level of Cx26 mRNA was 75% ± 7% in the apical turn,

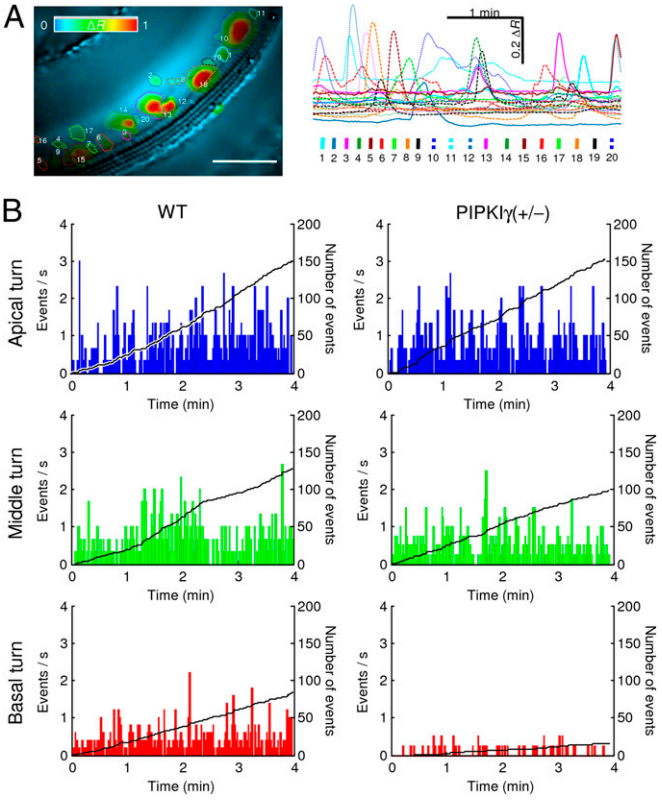

Fig. 5. Spontaneous $[Ca^{2+}]_i$ transients in the GER of WT and PIPKIγ$^{+/-}$ postnatal cochlear cultures. (*A*) *Left*: representative false-color image of fura-2 fluorescence ratio changes (Δ*R*), encoded as shown by the color scale bar, obtained as maximal projection rendering of all frames recorded in a basal turn culture from a WT P5 mouse imaged for 4 min at eight frames per second; 20 regions of interests are shown superimposed on different Ca^{2+} hot spots. (Scale bar, 100 μm.) *Right*: Fura-2 traces generated as pixel averages from the 20 color-matched regions of interests shown at *Left*. (*B*) Frequency histograms of spontaneous $[Ca^{2+}]_i$ transients (events) in cultures from P5 WT and PIPKIγ$^{+/-}$ mice (pooled data); in each graph, the solid black line (right ordinates) is the time integral of the corresponding frequency histogram and, as such, it tracks the mean number of events in the cell population from the onset of the recording.

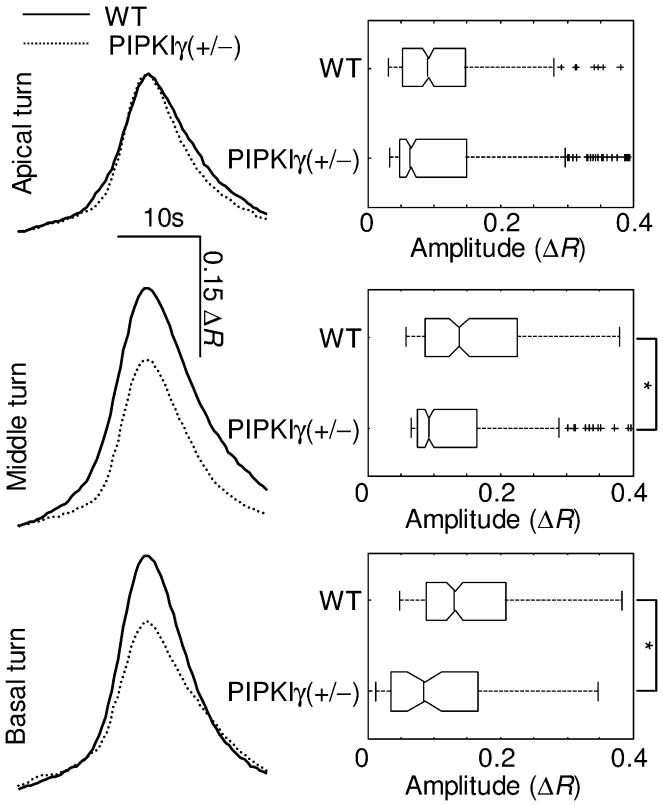

Fig. 6. Amplitudes of spontaneous $[Ca^{2+}]_i$ transients in the GER of cochlear organotypic cultures from P5 WT and PIPKIγ$^{+/-}$ mice (pooled data). *Left*: Average waveforms; *Right*: amplitude distributions; black asterisks indicate significant differences between data distributions (Mann–Whitney *U* test).

65% ± 7% in the middle, and 65% ± 6% in the basal turn. The corresponding figures for Cx30 mRNA were 70% ± 5%, 79% ± 5%, and 67% ± 4% in the apical, middle, and basal turn, respectively. Thus, impaired IP_3R Ca^{2+} signaling in cochlear nonsensory cells due to PIPKIγ deficiency causes significant downregulation of both connexin transcripts ($P < 0.005$), whereas our prior work determined that deletion of either Cx26 or Cx30 impairs IP_3R Ca^{2+} signaling in cochlear nonsensory cells (17, 27). A seemingly logical conclusion is that IP_3R Ca^{2+} signaling establishes a tight feedback loop between channel function and transcript levels of Cx26 and Cx30 in the developing cochlea.

To corroborate this conclusion, we analyzed also Cx30$^{+/-}$ and Cx30$^{-/-}$ mice. Note that normal auditory thresholds were reported for adult Cx30$^{+/-}$ mice (30), whereas both Cx30$^{-/-}$ mice (21, 30) and mice with targeted ablation of Cx26 in the inner ear (31, 32) are profoundly deaf at all tested frequencies. We also showed that whole-cochlea samples from postnatal Cx30$^{-/-}$ mice have only ~8% residual Cx26 mRNA (27). Here we found significantly reduced levels ($P < 0.001$) of Cx26 (58% ± 8%) and Cx30 (54% ± 9%) in the cochlea of ($n = 4$) P5 Cx30$^{+/-}$ mice compared with ($n = 4$) age-matched WT controls. The frequencies of occurrence of spontaneous $[Ca^{2+}]_i$ transients in GER cells of cochlear organotypic cultures from ($n = 4$) P5 Cx30$^{+/-}$ mice were indistinguishable from those of ($n = 4$) WT controls; by contrast, frequencies in ($n = 4$) Cx30$^{-/-}$ cultures were significantly reduced ($P < 0.001$) to levels resembling those of ($n = 4$) basal turn PIPKIγ$^{+/-}$ cultures (*SI Appendix*, Fig. S4). Finally, amplitudes of these spontaneous $[Ca^{2+}]_i$ transients were reduced in the middle and basal turn of Cx30$^{+/-}$ cultures ($P < 0.005$) and in all turns of Cx30$^{-/-}$ cultures ($P < 0.001$) (*SI Appendix*, Fig. S5).

To consolidate these findings we exploited the previously demonstrated capability of flufenamic acid, a connexin hemichannel blocker, to reversibly suppress both intercellular Ca^{2+} waves (17) and spontaneous $[Ca^{2+}]_i$ transients (21). In this study, we used a canalostomy approach for drug delivery to the inner ear via the posterior semicircular canal of WT mouse pups aged P4 or P5 (Movie S2). Four weeks after this single-shot injection, we tested hearing by recording ABRs and determined that auditory thresholds in ($n = 25$) mice injected with artificial endolymph (vehicle) were indistinguishable from those of ($n = 12$) noninjected controls; in contrast, thresholds in ($n = 4$) mice that had received flufenamic acid (250 μM) were significantly elevated ($P < 0.05$) by more than 15 dB SPL at all tested frequencies (*SI Appendix*, Fig. S6).

Discussion

This study reveals a unique hearing loss phenotype in adult PIPKIγ$^{+/-}$ mice at sound frequencies in excess of 20 kHz (Fig. 1) and demonstrates a key role of PIPKIγ in the inner ear and its essential function for the acquisition of hearing. It has been hypothesized that different enzymes contribute to the local control of $PI(4,5)P_2$ synthesis and confinement, thus generating distinct pools of $PI(4,5)P_2$ in the plasma membrane, each controlling specific functions (1). On the basis of studies in platelets it has been suggested that PIPKIα and PIP5KIβ contribute to the rapid synthesis of the $PI(4,5)P_2$ pool required for IP_3 and diacylglycerol generation upon agonist stimulation, whereas the $PI(4,5)P_2$ pool synthesized by PIP5KIγ does not play a major role in this process (6). At odds with this conclusion, inhibition of PIPKIγ expression in HeLa cells by RNA interference, although marginally reducing the total cellular $PI(4,5)P_2$ level, dramatically reduces IP_3 formation after histamine stimulation (33). The present data concur with the results in HeLa cells, demonstrating that Ca^{2+} signaling is selectively affected in nonsensory cells of PIPKIγ$^{+/-}$ and PIPKIγ$^{-/-}$ cochlear tissue.

Taken together, the simplest interpretation of the data presented in Figs. 2 and 3 is that reduction in gene dosage of PIPKIγ in the heterozygote causes a corresponding reduction in $PI(4,5)P_2$ levels in nonsensory cells of the developing cochlea. Consequently, PLC-mediated $PI(4,5)P_2$ hydrolysis in PIPKIγ$^{+/-}$ cultures more rapidly depletes a specific pool of $PI(4,5)P_2$ that is necessary for ATP-dependent intercellular Ca^{2+} wave propagation and maintenance of $[Ca^{2+}]_i$ oscillations in nonsensory LER cells. The apparent decrease in affinity for ATP in the medial and basal turn (Fig. 3*A*) most likely depends on the more marked reduction in PIPKIγ in these locations (Fig. 3*B*). Thus, below a critical enzyme level, $PI(4,5)P_2$ becomes the limiting factor, and optimal levels of IP_3 can only be produced when a larger number of P2 receptors are engaged by the ligand. This conclusion is also consistent with the reduced amplitudes of $[Ca^{2+}]_i$ oscillations evoked by 200 nM ATP (Fig. 4), which is a nearly saturating concentration in all cochlear turns of WT cultures, but submaximal for medial and basal turn PIPKIγ$^{+/-}$ cultures (Fig. 3*A*). Most relevant from a functional point of view, the hearing loss detected by our ABR measurements in adult PIPKIγ$^{+/-}$ mice maps precisely to this basal portion of the cochlea (Fig. 1), in a region comprising part of the middle and the whole basal turn where we detected the most pronounced Ca^{2+} signaling alterations (Figs. 3–6).

To summarize, the results presented here demonstrate that cochlear nonsensory cells of the LER and the GER share the same PLC- and IP_3R-dependent signal transduction cascade activated by ATP (*SI Appendix*, Fig. S3) and suggest that reduction in PIPKIγ gene dosage in the heterozygote causes a corresponding reduction in the critical pool of $PI(4,5)P_2$ necessary for normal Ca^{2+} signaling. We can speculate that the lack of spontaneous oscillations in LER cells in these experimental conditions (unlike those of GER) is due to (*i*) more efficient ATP hydrolysis by ectoATPases; (*ii*) reduced number and/or decreased opening probability of Cx hemichannel; or (*iii*) a combination of these mechanisms.

PIPKIγ reduction affects not only Ca^{2+} signaling directly (by reducing the precursor of IP_3) but also the expression of another key component of Ca^{2+} signaling, the channel-forming proteins Cx26 and Cx30. Indeed, we have shown previously that genetic manipulation of these connexins strongly affects Ca^{2+} signal generation and propagation (17, 21, 27). The present results single out Cx26 and Cx30 as both targets and effectors of Ca^{2+} signaling in the developing cochlea. As for the pathogenesis of

deafness, our comparative analysis of PIPKIγ$^{+/-}$ and Cx30$^{+/-}$ postnatal cultures (*SI Appendix*, Figs. S4 and S5) indicates that down-regulation of Cx26 and Cx30 mRNA level, by as much as ~50%, is insufficient per se to cause hearing loss. Instead, hearing acquisition is disrupted when Ca^{2+} signaling in cochlear nonsensory cells falls below a critical threshold. In Cx30$^{-/-}$ postnatal cultures the criticality is imparted by the uniform deletion of Cx30 and the drastic reduction of the residual Cx26 in the sensory epithelium. Indeed, in all turns of the Cx30$^{-/-}$ postnatal cochlea, IP_3R Ca^{2+} signaling in nonsensory cells is reduced to levels comparable to or lower than those of basal turn PIPKIγ$^{+/-}$ cochlea. As predicted, adult Cx30$^{-/-}$ mice are doomed to deafness at all frequencies (21, 30). In PIPKIγ$^{+/-}$ mice, the criticality is imparted by the apparent decrease in affinity for ATP only in the medial and basal turn, and the hearing defect is limited to the sound frequencies mapping in this region of the coiled sensory epithelium (Fig. 1). The importance of connexin hemichannel functionality in the critical period of hearing acquisition is further supported by the results with the connexin hemichannel inhibitor flufenamic acid (*SI Appendix*, Fig. S6), which suppresses Ca^{2+} signaling in nonsensory cells of cochlear cultures (17, 21) and causes hearing loss at all tested frequencies when delivered via canalostomy to the inner ear of mouse pups.

The severe hearing loss of Cx30$^{-/-}$ mice (30) and of mice with targeted ablation of Cx26 in the inner ear (31, 32) is associated with substantial cell death affecting hair cells and supporting cells. By contrast, we did not detect morphological abnormalities in the inner ear of adult PIPKIγ$^{+/-}$ mice, in which hair cells, spiral ganglion neurons and nerve fiber counts were indistinguishable from WT controls (*SI Appendix*, Fig. S1). Indeed, an overall normal functioning of the neural elements that contribute to the generation of synchronized discharges along the auditory nerve and brainstem pathway is required to account for the shape of PIPKIγ$^{+/-}$ ABR waveforms (Fig. 1*A*); and this is also consistent with the lack of an overt neurologic phenotype in these heterozygous mice, which behave and breed normally. Evidently, complete lack of one of these two connexins, combined with the regulation mechanisms that govern their coordinated expression (27), impacts on viability of inner ear cells more than impairment of Ca^{2+} signaling due to reduction of PIPKIγ gene dosage. Further understanding how the Ca^{2+} signaling defects reported here link to hearing loss in these different mouse models may prove crucial to unravel how hearing acquisition proceeds under normal circumstances, as well as to decipher the pathogenic processes underlying human hereditary deafness forms and, eventually, to test prospective therapies.

Materials and Methods

Statistical Analysis. Means are quoted ± SD, and *P* values are indicated by letter *P*. Unless otherwise stated, statistical comparisons of means were made by one-way ANOVA in conjunction with the Tukey range test.

Animal Handling. Animal handling was approved by the Ethics Committee of Padua University (Comitato Etico di Ateneo per la Sperimentazione Animale; Project 54/2009, Protocol 51731).

ABR Recordings. ABRs were used to assess hearing threshold of all mice strains used in this study.

Quantitative PCR. mRNA was extracted from freshly isolated P5 whole cochleae or from apical, middle, and basal turn, using the RNAeasy kit (Qiagen).

Ca^{2+} Imaging. Signals were measured as fura-2 emission ratio changes, $\Delta R = R(t) - R(0)$, where t is time, $R(t)$ is emission intensity excited at 360 nm divided by the intensity excited at 380 nm, and $R(0)$ indicates baseline ratio.

Immunohistochemistry and Confocal Imaging. Cochlear tissues were prepared according to standard protocols and analyzed using a confocal microscope (TCS SP5; Leica) equipped with an oil immersion objective (either 40× HCX PL APO 1.25 N.A.; Leica).

Further details are provided in *SI Appendix, SI Materials and Methods*.

ACKNOWLEDGMENTS. This study was supported by Ministero dell'Istruzione, dell'Università e della Ricerca-Progetti di Rilevante Interesse Nazionale Grant 2009CCZSES (to T.P. and F.M.), Telethon Grant GGP09137 (to F.M.), and National Institutes of Health Grant R37NS036251 (to P.D.C.).

1. Di Paolo G, De Camilli P (2006) Phosphoinositides in cell regulation and membrane dynamics. *Nature* 443:651–657.
2. Berridge MJ, Bootman MD, Roderick HL (2003) Calcium signalling: Dynamics, homeostasis and remodelling. *Nat Rev Mol Cell Biol* 4:517–529.
3. Doughman RL, Firestone AJ, Anderson RA (2003) Phosphatidylinositol phosphate kinases put PI4,5P(2) in its place. *J Membr Biol* 194:77–89.
4. Kwiatkowska K (2010) One lipid, multiple functions: how various pools of PI(4,5)P(2) are created in the plasma membrane. *Cell Mol Life Sci* 67:3927–3946.
5. Di Paolo G, et al. (2004) Impaired PtdIns(4,5)P2 synthesis in nerve terminals produces defects in synaptic vesicle trafficking. *Nature* 431:415–422.
6. Wang Y, et al. (2008) Loss of PIP5KIbeta demonstrates that PIP5KI isoform-specific PIP2 synthesis is required for IP3 formation. *Proc Natl Acad Sci USA* 105:14064–14069.
7. Sasaki J, et al. (2005) Regulation of anaphylactic responses by phosphatidylinositol phosphate kinase type I alpha. *J Exp Med* 201:859–870.
8. Wang Y, Lian L, Golden JA, Morrisey EE, Abrams CS (2007) PIP5KI gamma is required for cardiovascular and neuronal development. *Proc Natl Acad Sci USA* 104:11748–11753.
9. Kelly MC, Chen P (2009) Development of form and function in the mammalian cochlea. *Curr Opin Neurobiol* 19:395–401.
10. Mammano F (2011) Ca2+ homeostasis defects and hereditary hearing loss. *Biofactors* 37:182–188.
11. Müller M, von Hünerbein K, Hoidis S, Smolders JW (2005) A physiological place-frequency map of the cochlea in the CBA/J mouse. *Hear Res* 202:63–73.
12. Sobkowicz HM, Bereman B, Rose JE (1975) Organotypic development of the organ of Corti in culture. *J Neurocytol* 4:543–572.
13. Lim D, Rueda J (1992) Structural development of the cochlea. *Development of Auditory and Vestibular Systems—2*, ed Romand R (Elsevier Science, New York), 1st Ed, pp 33–58.
14. Beltramello M, Piazza V, Bukauskas FF, Pozzan T, Mammano F (2005) Impaired permeability to Ins(1,4,5)P3 in a mutant connexin underlies recessive hereditary deafness. *Nat Cell Biol* 7:63–69.
15. Mammano F, Bortolozzi M, Ortolano S, Anselmi F (2007) Ca2+ signaling in the inner ear. *Physiology (Bethesda)* 22:131–144.
16. Piazza V, Ciubotaru CD, Gale JE, Mammano F (2007) Purinergic signalling and intercellular Ca2+ wave propagation in the organ of Corti. *Cell Calcium* 41:77–86.
17. Anselmi F, et al. (2008) ATP release through connexin hemichannels and gap junction transfer of second messengers propagate Ca2+ signals across the inner ear. *Proc Natl Acad Sci USA* 105:18770–18775.
18. Majumder P, et al. (2010) ATP-mediated cell-cell signaling in the organ of Corti: The role of connexin channels. *Purinergic Signal* 6:167–187.
19. Tritsch NX, Yi E, Gale JE, Glowatzki E, Bergles DE (2007) The origin of spontaneous activity in the developing auditory system. *Nature* 450:50–55.
20. Tritsch NX, Bergles DE (2010) Developmental regulation of spontaneous activity in the Mammalian cochlea. *J Neurosci* 30:1539–1550.
21. Schütz M, et al. (2010) The human deafness-associated connexin 30 T5M mutation causes mild hearing loss and reduces biochemical coupling among cochlear nonsensory cells in knock-in mice. *Hum Mol Genet* 19:4759–4773.
22. Dolmetsch RE, Xu K, Lewis RS (1998) Calcium oscillations increase the efficiency and specificity of gene expression. *Nature* 392:933–936.
23. Mellström B, Savignac M, Gomez-Villafuertes R, Naranjo JR (2008) Ca2+-operated transcriptional networks: Molecular mechanisms and in vivo models. *Physiol Rev* 88:421–449.
24. Dolmetsch RE, Lewis RS, Goodnow CC, Healy JI (1997) Differential activation of transcription factors induced by Ca2+ response amplitude and duration. *Nature* 386:855–858.
25. Prank K, Gabbiani F, Brabant G (2000) Coding efficiency and information rates in transmembrane signaling. *Biosystems* 55:15–22.
26. Berridge MJ (1997) The AM and FM of calcium signalling. *Nature* 386:759–760.
27. Ortolano S, et al. (2008) Coordinated control of connexin 26 and connexin 30 at the regulatory and functional level in the inner ear. *Proc Natl Acad Sci USA* 105:18776–18781.
28. Li W, Llopis J, Whitney M, Zlokarnik G, Tsien RY (1998) Cell-permeant caged InsP3 ester shows that Ca2+ spike frequency can optimize gene expression. *Nature* 392:936–941.
29. Forge A, et al. (2003) Gap junctions in the inner ear: comparison of distribution patterns in different vertebrates and assessement of connexin composition in mammals. *J Comp Neurol* 467:207–231.
30. Teubner B, et al. (2003) Connexin30 (Gjb6)-deficiency causes severe hearing impairment and lack of endocochlear potential. *Hum Mol Genet* 12:13–21.
31. Cohen-Salmon M, et al. (2002) Targeted ablation of connexin26 in the inner ear epithelial gap junction network causes hearing impairment and cell death. *Curr Biol* 12:1106–1111.
32. Crispino G, et al. (2011) BAAV mediated GJB2 gene transfer restores gap junction coupling in cochlear organotypic cultures from deaf Cx26Sox10Cre mice. *PLoS ONE* 6:e23279.
33. Wang YJ, et al. (2004) Critical role of PIP5KIgamma87 in InsP3-mediated Ca(2+) signaling. *J Cell Biol* 167:1005–1010.